Improving Radar Imaging with Computational Imaging and Novel Antenna Design

by

Ruoyu Zhu

Department of Electrical and Computer Engineering
Duke University

Date:_____
Approved:

_____
Daniel L. Marks, Chair

_____
David J. Brady, Co-chair

_____
Jungsang Kim

_____
Henry O. Everitt

_____
William T. Joines

Dissertation submitted in partial fulfillment of
the requirements for the degree of Doctor
of Philosophy in the Department of
Electrical and Computer Engineering in the Graduate School
of Duke University

2017

ABSTRACT

Improving Radar Imaging with Computational Imaging and Novel Antenna Design

by

Ruoyu Zhu

Department of Electrical and Computer Engineering
Duke University

Date:_____
Approved:

_____
Daniel L. Marks, Chair

_____
David J. Brady, Co-chair

_____
Jungsang Kim

_____
Henry O. Everitt

_____
William T. Joines

An abstract of a dissertation submitted in partial
fulfillment of the requirements for the degree
of Doctor of Philosophy in the Department of
Electrical and Computer Engineering in the Graduate School of
Duke University

2017

Abstract

Traditional radar imaging systems are implemented using the focal plane technique, steering beam antennas, or synthetic aperture imaging. These conventional methods require either a large number of sensors to form a focal plane array similar to the idea of an optical camera, or a single transceiver mechanically scanning the field of view. The former results in expensive systems whereas the latter results in long acquisition time. Computational imaging methods are widely used for the ability to acquire information beyond the recorded pixels, thus are ideal options for reducing the number of radar sensors in radar imaging systems. Novel antenna designs such as the frequency diverse antennas are capable of optimizing antennas for computational imaging algorithms. This thesis tries to find a solution for improving the efficiency of radar imaging using a method that combines computational imaging and novel antenna designs. This thesis first proposes two solutions to improve the two aspects of the tradeoff respectively, i.e. the number of sensors and mechanical scanning. A method using time-of-flight imaging algorithm with a sparse array of antennas is proposed as a solution to reduce the number of sensors required to estimate a reflective surface. An adaptive algorithm based on the Bayesian compressive sensing framework is proposed as a solution to minimize mechanical scanning for synthetic aperture imaging systems. The thesis then explores the feasibility to further improve radar imaging systems by combining computational

imaging and antenna design methods as a solution. A rapid prototyping method for manufacturing custom-designed antennas is developed for implementing antenna designs quickly in a laboratory environment. This method has facilitated the design of a frequency diverse antenna based on a leaky waveguide design, which can be used under computational imaging framework to perform 3D imaging. The proposed system is capable of performing imaging and target localization using only one antenna and without mechanical scanning, thus is a promising solution to ultimately improve the efficiency for radar imaging.

Acknowledgement

I thank my advisor, Professor David J. Brady, and especially Professor Daniel L. Marks for his unquestionable support and patience. Without their guidance and insights, it would not be possible for me to finish this work.

Members of the Duke Imaging and Spectroscopy Program has helped me tremendously. Tsunghan Tsai, Patrick Llull, Alex Mrozack, Evan Chen, Andrew Holmgren, and Mehadi Hassan have offered me great help with their respective expertise. I have learned invaluable lessons from having discussion with them on a daily basis. Professor Henry Everitt and Jonathan Richard have helped me with my research and provided with data. Orges Furxhi is a great person to learn from and is always inspiring me with ideas. I have also spent so much with Tomas Zvolensky and Vinay Gowda who I are always patient with my questions. I also thank Paul Vosburgh who has helped me tremendously with the tools and 3D printers in the prototyping lab.

Finally I thank my parents and my wife for their love and unwavering faith in me. I would not have attained this achievement without their support.

Contents

List of Figures

1. Introduction

Radar (radio detection and ranging) was originally invented for detecting the range of a target by using the echo-location method [1]. Over the past decades, radar technology has been developed to perform not only ranging but also 3-D imaging. Radar can perform both active and passive imaging, regardless whether it be during the daytime or nighttime, and provide accurate depth information of the scene because of its ranging ability. Unlike imaging with visible light, radar imaging is not constrained by weather because its long wavelengths (1mm-1m) can penetrate cloud, smoke, fog, clothes, etc. The ability to penetrate these media makes radar a great tool for imaging under severe weather conditions [2], through-the-wall imaging [3], contraband detection at the airports [4-7], etc. However, as the wavelengths are much longer than visible light, the scattering microwaves detected by radar systems are sensitive to objects whose dimensions range from centimeters to meters. Although it is sufficient for many applications such as remote sensing, the resolution falls short for imaging applications when the target is small, such as concealed weapons at the airport.

High-resolution imaging technique for radar imaging has emerged from the 1950s to increase both the range and the cross-range resolution. High range resolution can be achieved by increasing the microwave bandwidth [8]. Cross-range, which translates to spatial resolution in optical imaging terminology, can be improved by increasing the size

of the physical aperture. However, under most situations, there is a limit on the size of the physical aperture. Multi-dimensional radar imaging requires an array of sensor antennas, i.e. focal plane arrays (FPA) to perform imaging [9] similar to cameras for visible wavelengths. However, achieving a large enough aperture in this fashion is accompanied by high costs especially for high-frequency applications. As frequency increases, the solid-state circuitry becomes much more expensive, thus making an array of antennas very expensive. An alternative approach by synthesizing a large aperture, i.e. synthetic aperture radar (SAR) methods, is developed to overcome the difficulties of building a large array of antennas by scanning a single aperture along a path to synthetically form a large aperture [10]. Mechanical scanning is a solution that comes at a much lower cost. However, the relative motion between the sensor and the target introduces artifacts in the final images [11]. In addition, scanning SAR methods are slow and often require a target to be stable. For example, the millimeter waves scanners being used at the U.S. airports collect holographic data of the person under inspection from every angle. The efficiency of this process can be drastically improved with the computational method and utilizing non-scanning, large effective aperture antenna, such as frequency diverse antennas [11-13].

The inefficiency is due to the requirement of a large number of sensors to cover a large aperture or otherwise the conduct of raster scanning as a tradeoff between system cost and acquisition time. The reason behind the problem is that a simple radar sensor

provides only range and reflectivity information. Novel antenna designs have made it possible to achieve multi-dimensional sensing. Another approach to improve the efficiency is to incorporate advanced sampling and processing algorithms, such as computational imaging methods, to reduce the scanning time. A combination of these two approaches, i.e., novel antenna design and computational imaging methods, and how this combination can improve the efficiency of high-resolution radar imaging will be the focus of this thesis.

Previous research has shown it is possible to apply compressed sensing [14,15] to minimize the amount of data to be acquired. Compressed sensing has been widely used in the field of imaging and sampling as it enables reconstructing with much fewer samples than what is required by the Shannon sampling theorem [16]. For compressed sensing to work for radar imaging, it is necessary to have knowledge of the structural complexity of the target so that we can indicate a compression rate for the algorithm. However, for radar imaging applications such as detecting a hidden object, it is impossible to obtain prior knowledge on the structural complexity of the target. As a result, no indication of correct compression rate can be made prior to taking the measurement. Adaptive sensing has been proposed to answer the question of how to design an adaptive sampling strategy and has stopping criteria [17]. A radar imaging system that utilizes adaptive sensing sequentially measures the scene from a distinct perspective. Each new measurement is formed by stepping the sensor to the next location. The choice of the next location is made

by the adaptive sensing algorithm to prioritize a new measurement that could contribute the most new information. By using an adaptive sensing algorithm, the total acquisition time can be reduced because non-contributing measurements are skipped. In this thesis, an adaptive method using Bayesian compressive sensing framework is discussed in detail.

The other approach to improving the efficiency of radar imaging is to jointly design custom, complex antennas with a corresponding computational imaging method [18-21]. As mentioned earlier, traditional sensors can only detect the range and reflectivity of a target by detecting and echoed pulse. Achieving 2D or 3D imaging without scanning comes at a large cost due to the expensive sensor array. Thus, there is a great need for an efficient single detector system or a sparse detector array system. The root of this problem is essentially how to reconstruct a two-dimensional signal with a one-dimensional sensor. Computational imaging combines digital processing algorithms with the physical design of imaging systems to extract information beyond the limit posed by the number of samples. By employing corresponding encoding and multiplexing techniques, researchers have realized that information and pixels are not the same things. Although the informational content cannot be increased by digital processing, it has been shown with compressive sensing algorithms that pixels can be retrieved beyond the number of measurements. This is especially necessary for signals that are multi-dimensional because computational imaging methods make it possible to reconstruct higher dimensional data

from lower dimensional integrated measurements with proper encoding or multiplexing [21].

Imaging in the radial frequency (RF) domain can benefit from computational imaging in a similar fashion, where the 2D information pertaining to the cross-range are integrated by the sensor. Frequency diverse antenna [11] becomes a popular tool among others such as reconfigurable arrays [22, 23] to multiplex the spatial domain radiation pattern so that it is possible to unfold the spatial structure of the target using the computational method briefly described above. Unlike other antennas such as phased array antennas for beam steering, the radiation pattern for a frequency diverse antenna is a function of cross-range, range, and frequency, thus the term frequency diversity [24]. Frequency diverse antennas thus make it possible to encode the sampling scheme by illuminating the scene with different radiation pattern at a different frequency. Frequency diverse antennas can be implemented using phased arrays, resonant structures such as metamaterials and resonant cavities, or folded leaky waveguides, which are all structurally more sophisticated compared to common antenna apertures such as horn antennas and open-ended waveguide. Another concern is that dielectric loss affects the amount of diversity such antennas could achieve, thus making air-filled waveguides and cavity based FDA structures much preferable. Therefore, designing and prototyping of frequency diverse antenna become the challenge as simulating these sophisticated antennas require forbidding computation power, and manufacturing complicated air-

filled antennas require high precision machining of custom made geometries. Rapid prototyping using additive manufacturing methods such as 3D printing provides a solution to easily manufacture custom antenna designs which lower the cost of materials and saves manufacturing time. Traditional machining methods start with a bulk piece of raw material and cut away unwanted parts. An experienced technician has to devise a computer-generated tool path dictating how the machine cuts the piece to achieve desired results. A 3D printer starts with an empty tray and fills the material into every voxel of the desired parts according to a 3D CAD design in a layer by layer fashion. The advantage of 3D printing is that structural complexity does not add to the complexity of manufacturing, i.e. the process of a complicated antenna is similar to the process of making a simple square block. Using 3D printing to facilitate antenna design has been explored by several groups around the world [25-30]. This thesis addresses this issue by introducing a new way of manufacturing complicated antennas using 3D printing technology and how we have used this method to prototype a frequency diversity antenna that is able to perform radar imaging.

1.1 Radar imaging basics

In this section, the basics and current methods of radar imaging are introduced and summarized as background for understanding how radar imaging can be improved using computational method jointly with a custom antenna design. The topics cover from the most basic function of a radar sensor, i.e. ranging detection, to more advanced

techniques such as 2D radar imaging and synthetic aperture radar imaging. The discussion highlights the design tradeoff between cost and acquisition time, thus the space for improvement using the method proposed in this thesis in the later chapters.

1.1.1 One-dimensional ranging and detection

The most basic form of radar imaging is detection and ranging. It is done by transmitting an electromagnetic wave and measuring the reflected field using a transceiver. Assume a short pulse signal is transmitted at time t=0 and travels at the speed of light c. It travels a certain range R upon a reflecting target and returns to the transceiver at time τ. We can thus determine the range where the target is located by using the relationship $R = c\tau/2$. A single transceiver thus is able to help us locate the target on a circle with radius R originating from the transceiver. The fact that the transmitted wave is originated at the same location as where the reflected wave is received is referred to as monostatic radar. The counterpart of monostatic radar is bi-static radar, where the emitter is at the different location than the receiver location. Similarly, the receiver measures the time of flight (ToF) of the signal to calculate the range R of the reflecting target. However, unlike monostatic radar, the conclusion is that the target lies on an ellipse where the foci are the locations of the transmitter-emitter pair. The difference between the two types of setups is illustrated in Figure 1.1. The time of flight measurement, which indicates reflectivity along the range dimension, has multiple peaks when imaging a complicated scene and thus can be seen as a one-dimensional projection of a two-dimensional scene.

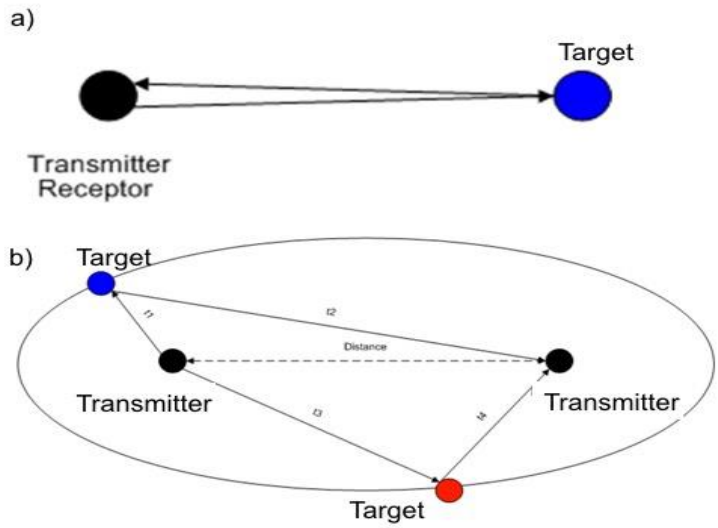

Figure 1.1 Illustration of basic radar imaging system

(a) Monostatic system and (b) bi-static system

A high range resolution can be achieved using a broadband signal. The time-domain measurement and the frequency-domain measurement are related by the Fourier transform. In principle, the range resolution of a radar with bandwidth B is given by the equation

$$\Delta r \approx \frac{c}{2B} \tag{1.1}$$

1.1.2 2D radio frequency imaging methods

Going beyond simple one-dimensional ranging, 2D imaging with radar sensors and using radio frequency wavelengths, in general, is appealing because of its ability to add range information on top of reflectivity strength and the ability to penetrate occlusions. Two-dimensional RF imaging methods can be categorized into three major categories, focal plane array (FPA) imaging, phased array imaging, and synthetic aperture

radar imaging (SAR) methods. Figure.1.2 compares the differences between these common methods.

	Focal Plane Array	Phased Array	Synthetic Aperture Imaging
Acquisition	Real-time	Electronic beam steering	Mechanical scanning
Sensor type	Antenna array	Antenna array	Single Antenna
Illumination	Active / Passive	Active	Active

Figure 1.2 Comparison between common RF imaging methods

The most direct method for imaging at millimeter wavelength is to use a focal plane array (FPA), which is analogous to optical imaging using CCD or CMOS arrays. One advantage of using FPA imaging is that all image elements are viewed simultaneously, which increases the frame rate and sensitivity limitations. An earlier effort by Yujiri et al. described in [9] presented a prototype of a W-band passive millimeter wave camera aimed to image through obscurant in the atmosphere such as fog and smoke for aviation applications. A later design by Richard and Huguenin [31] features a millimeter wave FPA imager at 94 GHz with up to 48 x 64 pixels, where each channel of the FPA is a wide band, double sideband super heterodyne receiver with nominal 94G Hz center frequency. Another important aspect regarding FPA imaging is the optics of the system. At millimeter wavelengths, normal optics would not work because the

wavelength is too long compared to visible light. Therefore, zoned lenses are used to focus the beam to the millimeter wave FPA. The system described in [31] utilizes a zoned aplanatic lens with a f/# of 1.1 and 30cm diameter. Figure 1.3 demonstrates the structure of the imager developed by Yujiri et al. The advantage of FPA imaging is the diversity in terms of an illumination source. It can be used as either active imaging or passive imaging. In addition, the ability to perform high frame rate imaging is much desired by many monitoring applications. However, the cost of FPA systems is usually high due to the complicated circuitry and the need to utilize a large number of sensors to achieve high enough pixel resolution.

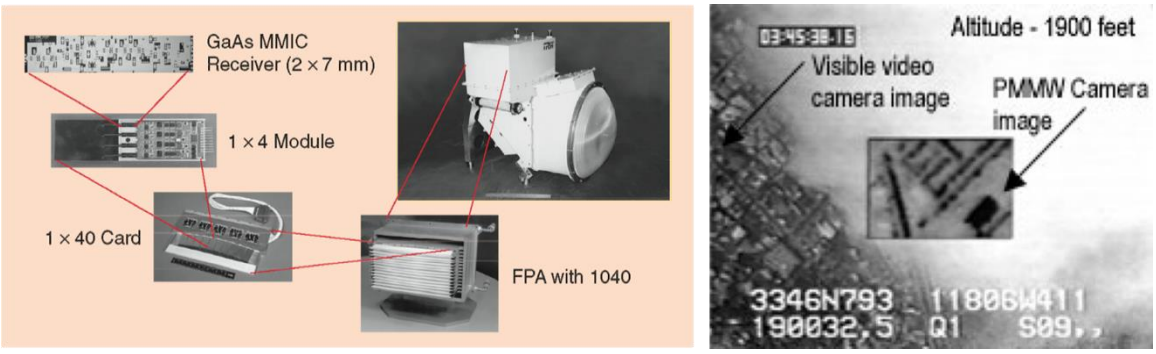

Figure 1.3 FPA imaging system and sample FPA images [9]

Another type of array imaging is provided by the phased array antenna [32, 33]. A phased array is a group of single antennas, each connected with a phase shifter. Each subsequent array element gets an increment phase delay of $\Delta\Phi$. By changing the incremental phase delay, the array can form a beam pointed in a different direction. Figure 1.4 shows the configuration of an example linear phase array. The phased array antennas

can steer the beam from one direction to another at a relatively fast speed, at a scale of microseconds, thanks to the ability to electrically control the phase delay. In addition, phased array can form high gain and high directivity beams simply by having more radiating elements, which is known as the array effect [34]. The disadvantages of this type of phased array antennas are that the coverage is limited to +/- 60 degrees from broadside, in addition to the still complicated and expensive circuitry and structure.

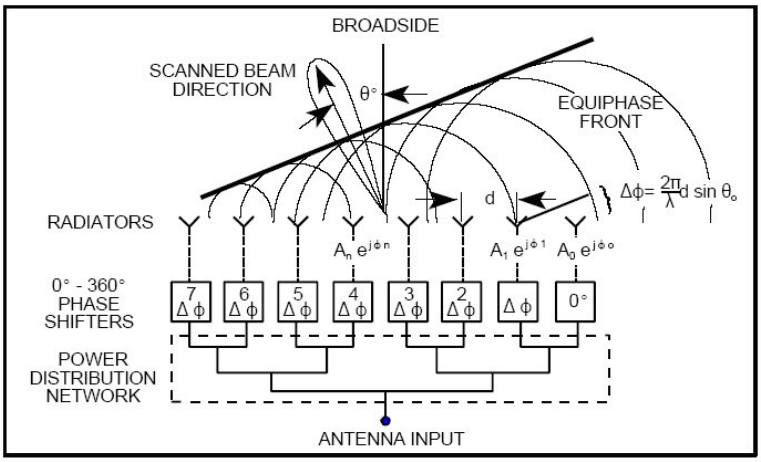

Figure 1.4 Illustration of a linear phased array antenna performing beam steering with phase shifting [35]

Another type of phased array antenna, frequency scanning array, utilizes a fixed phase difference between the radiating elements and performs beam scanning by sweeping the frequency. Frequency scanning arrays are often based on wave propagation in waveguides. An example of frequency scanning array is the slotted leaky waveguide [34]. A slotted leaky waveguide is usually an air-filled waveguide with the TE10 mode as the fundamental mode. Periodic slots are cut on the broad wall on of the waveguide so

that the induced current on the wall has to circulate around the slot and thus become a radiating dipole [34]. The constant separation between neighboring slots provides a fixed phase delay between each radiating slot. When frequency sweeps, the main beam from the antenna steers to different directions under the same principle as the phase-shifting phased arrays. Folded waveguides are sometimes used to increase the phase delay between radiating elements while maintaining a compact physical presence. In Chapter 5 of this thesis, we will discuss a novel design for a frequency diverse antenna based on this method. Figure 1.5 illustrates the slotted leaky waveguide and the folded waveguide as examples of the frequency scanning antennas.

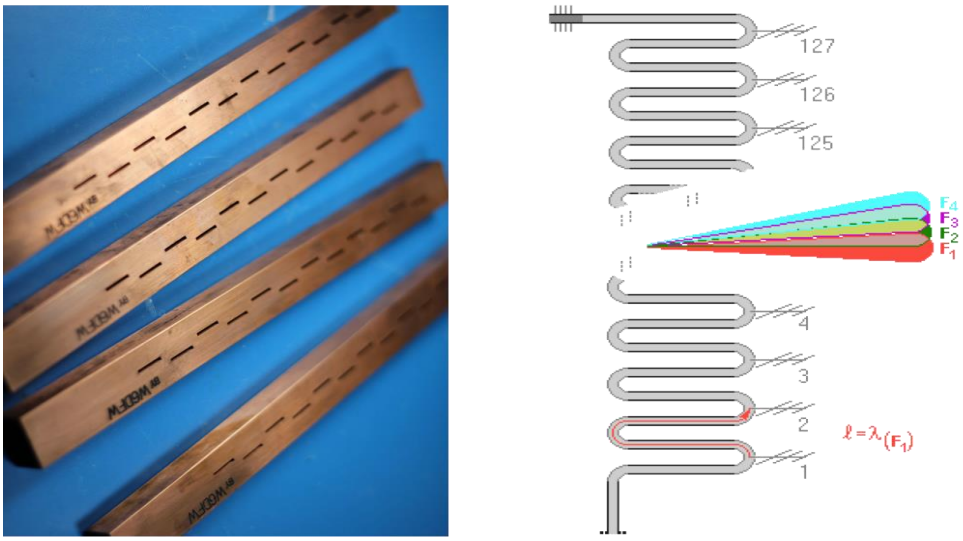

Figure 1.5 Leaky waveguide antenna as beam-steering waveguide [36]

In optical imaging, the imaging resolution is diffraction limited [37]. Fine resolution for an optical imaging system can be achieved by having a large numerical aperture, which is obtained by employing a physically large lens or introducing an immersion medium with a higher refractive index, such as oil. In radar imaging, the principle is the same, except that the wavelengths are much longer than visible light. Thus, it is impossible to have a single aperture that is physically large enough and even more impossible to immerse the space between the aperture and the target with oil. A synthetic aperture radar (SAR) is the solution to this problem that dates back to more than 60 years ago [38]. The idea is quite simple, moving the single radar aperture along while taking the reflectivity measurement serially at each spatial sampling point. Figure 1.6 (a) shows an illustration of an airborne SAR system taking measurements of the scattered waves along the path of its flight. Its principle is similar to Gabor's theory for holography. With the advantage of the ability to sample both the amplitude and the phase of the reflected field, thanks to the longer wavelengths, the SAR measurement is equivalent to sampling the wavefront of the scattering object. The effective aperture is essentially the distance that the flight has covered, rather than the size of the physical aperture of the single transceiver (except for azimuthal resolution, which is one-half of the physical aperture length [8]. Having the field measurement allows us to propagate the field to any distance or focus

the field to an image as a post process. Figure 1.6 (b) shows an example of the SAR image of Washington DC (Courtesy of Sandia Natl. Laboratory).

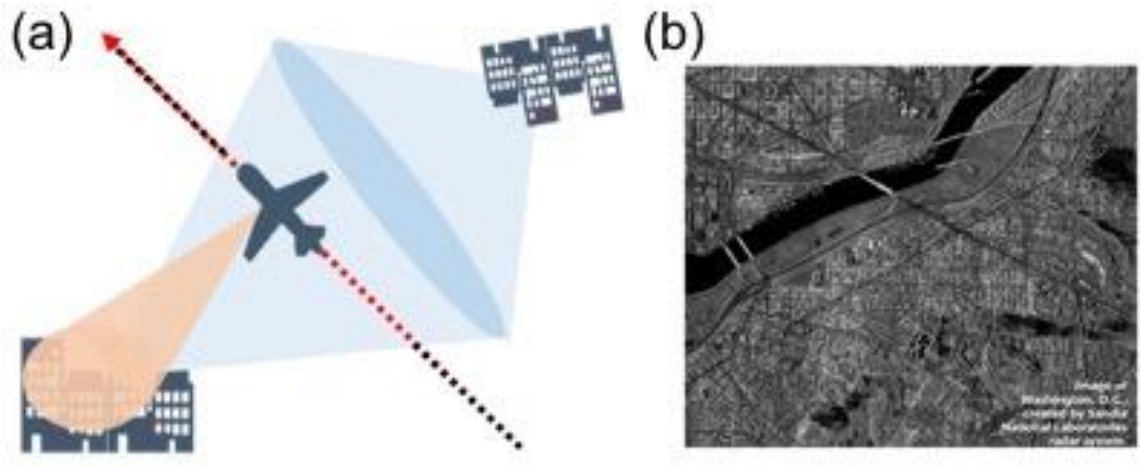

Figure 1.6 Illustration explaining basic synthetic aperture radar imaging and demonstration of a sample image

(a) diagram showing the idea of synthesizing a large aperture using SAR method (b) Sample aerial SAR image of Washington DC, created by Sandia National Laboratories radar system

The theory for SAR imaging has been greatly simplified here as there are many different types of SAR imaging modalities and processes to consider, such as spotlight SAR, stripmap SAR, and inverse synthetic aperture radar (ISAR), and complications such as the Doppler effect and so on.

1.2 Computational imaging method with novel antenna design

Computational imaging rises as a tool that combines the physical design of imaging systems and digital processing to extract information beyond the pixels that have

been measured by traditional imaging systems. Computational imaging methods have been popular in optical imaging under visible light regime because of its ability to overcome the limit posed by sampling and the ability to reconstruct signals that are multi-dimensional in nature with fewer dimensions. One good example of computational imaging is combining compressed sensing algorithms with physical designs of imaging systems that allow appropriate coding strategies to multiplex multi-dimensional signals. Under visible light where the 2-D sensor array is easily accessible, research has been done to expand the sensible dimension into spectrum domain [39], time domain [40], and polarization states [41]. These are all made possible by using coded apertures that multiplex the signals in the extra dimension and are reconstructed using carefully calibrated forward models. In the radio frequency scheme, computational imaging has been playing an increasing role because radar imaging systems are moving toward fewer sensors and faster acquisitions. This thesis introduces and discusses how computational imaging methods can be used in combination with physical aperture design to improve imaging efficiency.

1.3.1 Compressed sensing and adaptive sensing in radar imaging

Over the last decade, there have been significant advances in compressive sensing (CS) and applying CS in imaging applications [14]. The CS algorithm deals with signals that can be represented as N-dimensional real vectors so that the required measurements

to represent the signal are much fewer than N. Instead of measuring the signal directly and making N separate measurements, CS theory implies that one may only need to make a small number of related measurements due to the assumption that the original signal is sparse in some linear basis B, such as the wavelet basis. The reconstructed signal thus represents the original signal as a sparse linear combination of the orthonormal basis B. CS overcomes the Shannon sampling limit and greatly simplifies the sampling and sensing of large dimension signals.

SAR imaging can benefit the most from compressive sensing because the most significant drawback of a synthetic aperture is the large number of measurements and wide bandwidth required for high resolution. The SAR measurement data can be reconstructed using the traditional CS algorithm because the signal under reconstruction is sparse in the wavelet basis (another basis might also apply). The question then comes to how to model the SAR imaging geometry and what sampling strategies can be made based on the linear-regression-based compressive sensing, i.e. designing the projection matrix. Yigit et al. [42] have proposed three main sampling strategies based on random sampling, spatial-frequency domain sampling, frequency domain sampling, and spatial domain sampling.

One major concern about applying CS algorithm to SAR/ISAR is that the compression rate depends on the sparsity of the scene and the performance of CS reconstruction needs to be compensated by increasing the number of samples. Therefore,

determining the necessary number of random samples becomes impossible when the estimation of the complexity of the target is unavailable. One solution to the problem of unknown complexity is to develop an adaptive algorithm based spatial sampling that can estimate the next best location to probe on the fly. The algorithm should stop once the error between consecutive reconstructions begins to converge and diminish.

Mrozack et al. [17] have demonstrated a special case of adaptive SAR measurement imaging a wire as a single point scatterer. The method is based on the adaptive classification procedures first specified in [43], which relies on specifying the measurement model and existing data to specify the next step location. The searching of the next step is based on maximizing the determinant of the precision matrix of the Gaussian posterior distribution. However, the method is limited to sparse point scatterers modeled as a single point. Increasing the number of scatterers essentially enlarges the parameter space and thus requiring inversion of huge matrices. Another drawback of this method is that the model has to be indicated exactly, meaning the number of sparse scatterers has to be known before investigation. In this thesis, a new method based on compressive sensing in a Bayesian framework is proposed. The proposed method solves the adaptive sensing problem without needing prior knowledge of the target and stops after the iteration error starts to converge.

1.3.2 Computational imaging with frequency diverse antenna

SAR imaging achieves high-resolution imaging by mechanical scanning to synthesize a large aperture. Ultimately, the reason for increased resolution is diverse illumination; that is, for a single target within the scene, it is illuminated by the radar footprint at multiple locations, thus equivalent to collecting the scattered wave at a wide collection of angles. The better alternative to achieving diverse illumination by mechanical scanning is electronic scanning, which is much faster. However, electronic scanning requires large quantities of active components such as amplifiers and switches in the circuitry and thus increases the cost and complexity of the system. Active components are able to control the current flow and gain of the signal with energy from an external source, whereas passive components like resistors, capacitors, and antennas are only capable of storing or dissipating energy and do not introduce much complexity in the circuitry. The desire of simple electronic scanning systems has inspired the development of passive electromagnetic components such as metamaterial antennas [18]. The goal is to have different radiation patterns at different frequencies, thus the term frequency diverse antenna. Simple passive electromagnetic components such as dipole antennas do not change their response by much when tuning the excitation frequency. Resonators, on the other hand, have a dramatic frequency response at their resonant frequencies. The metamaterial antennas [18] are networks of resonators that switch their radiation pattern while tuning excitation frequencies, similar to mechanical scanning. However, the

frequency-diverse capability is not limited to resonant structure networks. The Echelle grating millimeter beam scanner [5] has demonstrated the ability to map a frequency sweep to a 2-D scene. The same principle has also been used widely for steering beams using leaky waveguides [44] and phased arrays [32].

Marks [11] has rigorously modeled the theory of imaging using frequency diverse antennas and has explained the reason why using frequency diverse antennas is capable of increasing the imaging resolution and efficiency. The interrogation of the object by transmitting a beam and receiving the reflection with receivers corresponds to multiplying the two aperture functions in the spatial domain. Thus, in the Fourier space, the interrogation corresponds to the convolution of the two aperture functions. Since the spatial resolution is inversely related to the spatial frequency bandwidth, a large bandwidth is preferred to achieve high resolution. It requires the interrogation beam to illuminate a large collection of angles, i.e. the q vectors, which results in a large spatial bandwidth. Figure 1.7 shows the comparison of a non-frequency-diverse system and a frequency diverse antenna system. Figure 1.7 (a)-(c) shows the spatial frequency space, the q-space, representation of an imaging scheme with discrete transmitter and receivers. In Figure 1.7 (b), q_T illustrates the q-vector representations of the transmitting wave, and q_R represents the receiver q-vectors. Figure 1.7 (c) shows the convolution of the two in the Fourier space. Figure 1.7 (d)-(f) shows the Fourier space coverage of imaging using a frequency diverse antenna. As shown in Figure 1.7 (d), using frequency diverse panel

provides a wider collection of illumination and receiving angles; thus, the Fourier space coverage is a much larger area than when using discrete antennas. The resulting convolution in the Fourier space compared to using discrete antennas is thus much larger. The ideal case is to cover the whole Fourier space, i.e. the Ewald sphere. However, that requires an infinitely large aperture and imaging from both sides, such as the 4π microscopy [45].

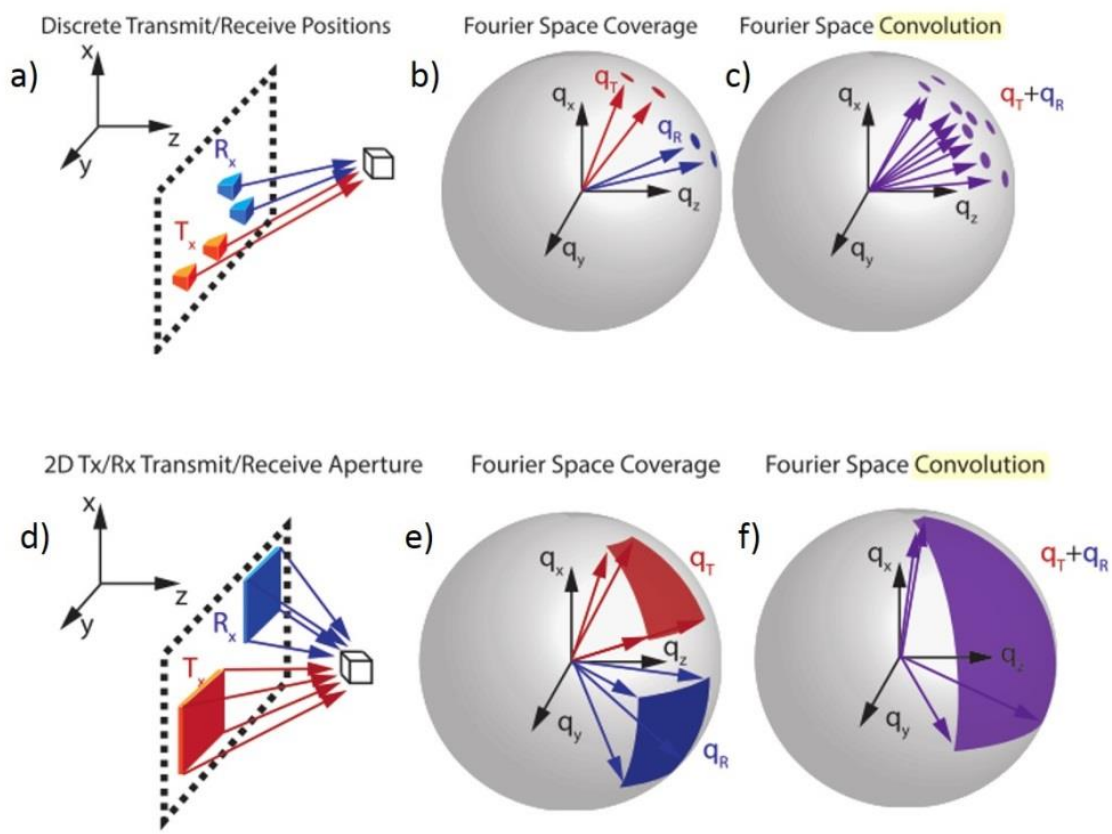

Figure 1.7 Comparison between traditional bi-static antenna pairs and frequency diverse imaging antennas [11]

1.4 Rapid prototyping passive radio frequency components

The growing interest in novel antenna design such as frequency diverse antennas [11-13, 24] has motivated research in additive manufacturing passive microwave components and devices. Traditionally, microwave waveguide assemblies are constructed by connecting various components with waveguides, which often results in a large number of joints that degrade the performance. In addition, these components are made using high-precision machining of metal materials. With the size of features on the components' scales with the wavelengths, i.e. for higher frequencies, the features become smaller and require higher manufacturing precision, which translates to manufacturing cost, complexity, and the need for high precision tools such as the computer numerical controlled (CNC) machines.

A more efficient way to manufacture such components and assemblies is using additive manufacturing methods such as three-dimensional (3D) printing. Waveguide components, such as antennas and waveguides, can be integrated into a single part without the need for additional interfaces, eliminating adapters. Current 3D printing technology has achieved layer resolution up to 15~20 μm, a fine enough resolution for simple W-band components operating at the 75-100GHz range. Furthermore, 3D printed waveguides and antennas are light-weight and low-cost compared to machined metal components. Previous efforts [26-29, 46-53] have demonstrated 3D printing radio frequency components with various methods.

In this thesis, polymer jetting (PJ) 3D printing is chosen as the primary method to rapid-prototype passive components because of its resolution, surface smoothness, production time, and cost compared to other capable methods. Figure 1.8 provides a reference to the 3D printing technology terminologies, listing 3D printing methods currently used for prototyping radio frequency passive components. An overall comparison and analysis for the chosen method are provided in this section as an introduction to understanding the challenge and requirement for the rapid prototyping of unique and novel antennas for imaging purposes.

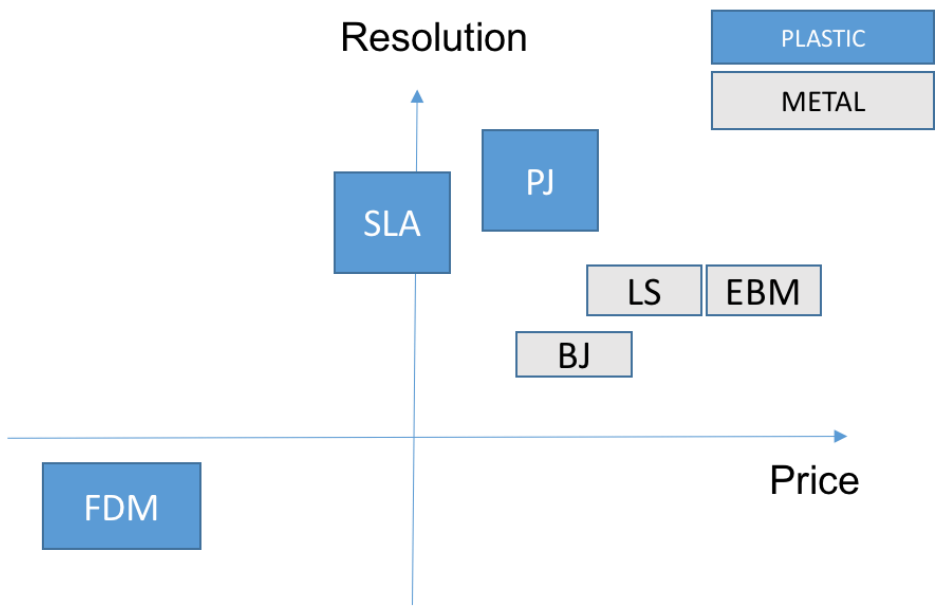

Figure 1.8 General resolution vs. price comparison of major 3-D printing methods

The first challenge to face is the conductivity of the material. For passive components, such as waveguides and antennas, to guide and radiate electromagnetic waves at the gigahertz range, the surface must be conductive. Three-dimensional metal

printing methods, such as laser sintering (LS), binder jetting (BJ), and electron beam melting (EBM), provide a direct solution to prototype any arbitrary structure in metal. It has been shown in [49,50] that successful prototypes have been made using EBM and LS 3D printing. However, the cost of such machines and materials is expensive. Another approach to overcoming the conductivity challenge is to modify plastic 3D printing technology with customized conductive material. As discussed in [25, 51], a mixture of ABS with conductive nanoparticles has been used as the printing material. The mixed material is conductive but still has low conductivity compared with pure metal. However, for radio frequency components, such as waveguides, high conductivity is required to minimize transmission loss. To satisfy the conductivity requirement for guiding radio frequency, the components only need a layer of conductive metal that is thicker than the skin depth, which is defined as $\delta=1/(\pi f \mu \sigma)$ where μ is the permeability, σ is the conductivity of the material, and f is the operating frequency. For instance, at 10GHz, the skin depth for copper is about 0.6 μm. Therefore, it is desirable to prototype using plastic printing methods such as polymer jetting (PJ), stereolithography (SL), and fused model deposition (FDM), and deposit a thin layer of pure metal on the surface. [48, 52] has demonstrated using 3D printed antenna with a dielectric substrate and conductive spray paint on the surface. The method of using conductive spray or mixed material can produce sufficient conductivity for antenna applications; however, components such as waveguides require higher conductivity.

The next challenge to consider is the resolution and surface roughness of these 3D printing technologies. Although low-cost plastic methods such as FDM are capable of prototyping the structures, as demonstrated by [25], yet the resolution is currently limited to 0.2~0.3 mm, and the surface has to undergo acetone vapor polishing procedures. This is because the FDM technology uses a wire-feeding method to feed the printing nozzle with ABS raw material in wire shape. Thus, the resolution is limited by the thickness of the ABS feed. The resolution is key to producing a prototype true to the desired shape and structure and is essential to applications with higher frequencies, such as in the millimeter wave frequency. For example, at K-band (18GHz-26.5GHz), the narrow wall for a waveguide is 4.3 mm; thus, for K-band applications discussed in this thesis, the FDM methods are not able to produce sufficient resolution. Polymer-based methods, i.e., polymer jetting and stereolithography are more attractive because the resolution is between 15μm to 20μm; the difference is in the method of deposition. Polymer-based methods utilize the polymerization process where liquid polymer solidifies under UV light. Polymer jetting technology uses a fine nozzle to deposit small droplets of the liquid polymer under UV light whereas stereolithography technology builds the prototype in a liquid polymer tank by shining a focused UV laser onto the surface of the liquid. Polymer-based methods also result in a much smooth surface, as the liquid polymer naturally tends to level the surface, especially for stereolithography where parts are pulled out from a liquid polymer tank. It has been demonstrated in [53] that stereolithography-printed

waveguides are able to operate up to the W-band frequencies. However, compared to polymer jetting methods, stereolithography printed parts require longer post processing time, i.e. hours of UV curing. In addition, when printing parts with straight-tube structures such as straight waveguide sections, stereolithography printers tend to avoid focusing its UV laser at the same location over a long time and potentially degrade the glass plate, which is unavoidable when building a straight tube. This is the reason most SL printed waveguides are not printed upright but slanted, causing the waveguide channel to suffer from printing lines.

In consideration of all the above-mentioned challenges and characteristics of each printing technology, the polymer jetting method is chosen as the primary method for the works in this thesis. In Chapter 4, the detailed method by which pure copper is deposited on the polymer surface is proposed as an addition to current methods of additive manufacturing passive radio frequency components.

1.5 Thesis outline

Radar imaging is limited by the simplicity of the sensor and the lack of computational methods to improve the efficiency. This thesis discusses the possibility of improving radar imaging efficiency using an approach of using computational imaging methods in combination with novel antenna designs. The thesis first proposes two methods improving the efficiency using only computational methods. Chapter 2 discusses an algorithm for using a sparse set of simple antenna transceivers to perform reflectivity

and surface profile reconstruction. This algorithm allows reconstruction using a small number of sensors in contrast to using a large array of transceivers or using a single transceiver scanning the whole scene. In chapter 3, an adaptive sampling algorithm based on the Bayesian compressive sensing algorithm is introduced to improve the efficiency of millimeter wave ISAR imaging. Traditionally, ISAR imaging in a lab environment is performed by mounting the target on a rotational stage while rotating a single transceiver antenna around the stage. Measurement is taken at each angle around the stage to reconstruct the object on the stage. With adaptive sensing, the process can be improved because the algorithm selectively chooses to perform measurements at angles that contribute more information, thus improving the acquisition time and reducing mechanical movements.

The thesis then discusses the impact of novel antenna design when applied to computational imaging methods, by first introducing a method of rapid prototyping custom antenna designs that facilitates novel designs. In chapter 4, a method to 3D print and metalize passive radio frequency components with polymer-based printing technology is proposed. This method makes it easy to rapid prototype any custom-made antenna in a laboratory environment, without the need of industry-level, high-precision machining facilities. Chapter 5 demonstrates how novel antennas designed for computational imaging can perform imaging beyond single dimensional range detection. The antenna designed is a novel frequency diverse antenna based on a single leaky

scanning waveguide. The image acquired with this antenna is reconstructed using the computational method after carefully calibrating the diverse radiation pattern for each frequency. This method opens up future possibilities of designing an antenna to optimize measurements according to its computational imaging forward model. The final chapter summarizes the work presented in this thesis and discusses the impact and future work on improving radar imaging using these methods.

2. Surface profile and reflectivity reconstruction using sparse array millimeter wave time-of-flight imaging

One of the most popular applications for millimeter wave imaging is concealed weapon detection for security reasons. The first millimeter wave imaging system designed to detect concealed weapons was proposed by Farhat and Guard [54], and it was composed of a stationary source and a scanning film-based receiver. The technique was then improved with digital sensors and digital reconstruction by Collins et al. [55]. The state-of-the-art method uses holographic reconstruction, which is similar to the backward wave reconstruction algorithm for acoustic holography described by Boyer [56]. However, the method in [56] employs Fresnel's approximation and thus limits the resolution for near-field imaging systems. Sheen et. al [4, 58] has extended the algorithm developed by Soumekh [59, 60] for SAR and proposed the holographic reconstruction algorithm for near-field 2D and 3D imaging reconstruction with millimeter wave. Nowadays, security scanners based on this technology are widely used in airports for security measures; however, these methods require scanning arms populated with sensors and, as a result, they are slow and expensive. In this section, a new method for millimeter wave imaging that enables surface profile reconstruction and reflectivity estimation with a time-of-flight (ToF) imaging algorithm is proposed using only a sparse array of sensors and no mechanical scanning required.

2.1 Introduction

Time-of-flight imaging is a widely used technique in optical imaging to estimate the range and location of a target. ToF measures the total round-trip time for the light signal to travel between the device and the target. From the measured travelling time and the known speed of light, the distance between the device and the reflecting target can be easily deduced; thus, ToF imaging has been the ideal solution for range detection and 3D imaging in optical wavelengths. Range detection in radio frequency is fairly easy, as compared to optical range detection, as it is the basic functionality of a simple sensor. This is because, at microwave frequencies, the electronics can operate fast enough to capture the phase of the signal, whereas the optical sensors, such as CMOS and CCDs, are only capable of capturing the intensity. Hence, imaging with radio frequency transceivers utilizing the range information can be treated as time-of-flight imaging and can thus be optimized with ToF imaging techniques.

Mechanical scanning has always been involved in ToF imaging, such as the push-broom scanning involved in the Lidar system for ocean floor profiling [61] and the scanning mirror method involved in landscape imaging applications [62]. It has been mentioned in the earlier chapter that the scanning method is rather slow and inefficient. However, since the beam is focused on a spot corresponding to a single pixel, a non-scanning method requires a large array of such sensors to cover the whole field of view.

In this chapter, the proposed millimeter-wave ToF imaging method uses a divergent beam to eliminate the need for mechanical scanning.

The divergent beam radar imaging is similar to the traditional SAR imaging method, which achieves high resolution by synthesizing a large effective aperture. SAR imaging works under the assumption that the entire volume of the target is scattered and thus requires dense measurement in both the spatial and frequency domain [42]. The goal is to reduce the number of sensors needed so as to decrease the cost of such systems, which is equivalent to the problem of reconstructing an image with few measurements. Compressed sensing [14, 15] has been the ideal framework for solving such a problem as it states that the number of samples can be much fewer than the limit required by the Shannon sampling theorem [16] if the signal is sparse in some basis.

When imaging extended objects, traditional SAR always assumes the objects take a certain amount of space in the object space, making them not sparse objects. However, the objects of interest are specular to electromagnetic waves up to the GHz range. Therefore, the targets can be seen as surface objects in the object space. Using this condition as the prior knowledge enables taking advantage of the sparsity and essentially reducing the number of measurements required to reconstruct the target surface shape and reflectivity.

2.2 Algorithm Overview

The method proposed in this chapter employs the sparse nature of the reflecting

surface object, which enables the use of only a few transceivers and eliminates mechanical scanning. The imaging system consists of a sparse array of bistatic antennas, meaning that the transmitters and receivers are not the same antenna. The bi-static arrangement is advantageous over mono-static arrangement because for a given number of transceivers, bi-static pairs are able to retrieve more sets of ToF measurement. The demonstrated system operates at K-band, 18GHz to 26.5 GHz; however, it can be easily scaled to other frequency ranges.

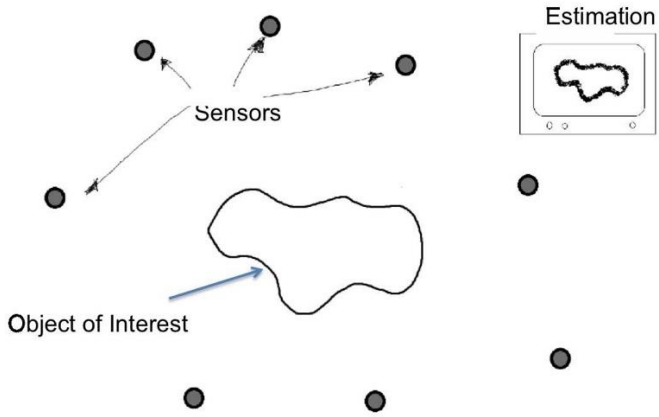

Figure 2.1 The proposed imaging system scheme of surface constrained imaging reconstruction

The ToF measurement is equivalent to the range measurement, which is made by Fourier transforming frequency domain measurement, i.e., reflected amplitude and phase at each frequency. The time-of-flight measurement is then analyzed by the algorithm described below to extract the surface reflectivity information.

Figure 2.2 shows the algorithm overview of the proposed method. The time-of-flight data contains peaks that correspond to the roundtrip distance from the transceiver

to the point that is reflecting. Therefore, each of these peaks maps to an ellipse in the two-dimensional space that contains all the possible locations that could have reflected to the receiver. However, with many sets of bi-static measurement and only a small subset of the ellipses corresponds to the true location of the reflecting points on the surface. The prior knowledge that the target is a surface reflecting object helps with selecting which part of the ellipses corresponds to the true reflecting area.

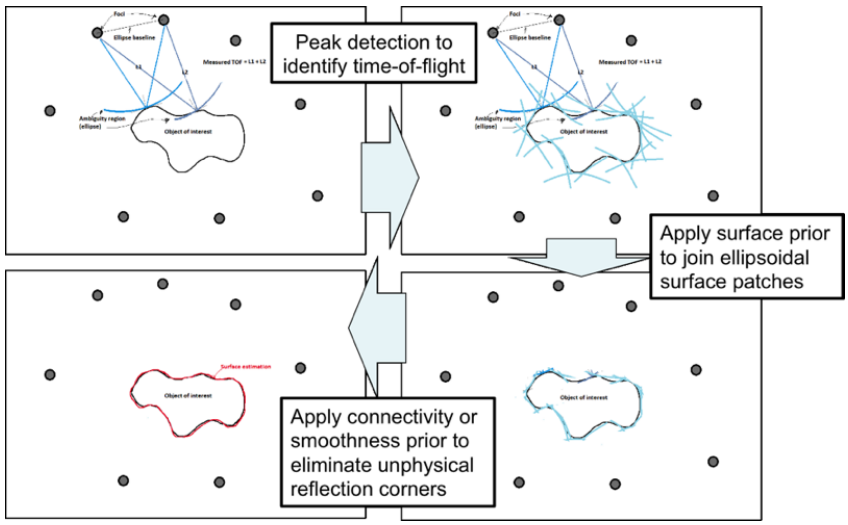

Figure 2.2 Overview for proposed ToF millimeter wave imaging algorithm

A prior estimation of the target surface is acquired by using the depth camera from Microsoft Kinect. The surface acquired by the depth camera is not necessarily the surface that reflects the millimeter wave signal transmitted by the transceiver because the depth camera sensor is operating in the IR range. However, in the case of imaging people for security purposes, it is acceptable to assume the surface seen by the depth camera is close enough to the surface that reflects the millimeter wave. With this surface priority, we are

able to narrow down to a smaller subset on each ellipse and form an estimation of the surface.

2.3 Method

To form the ToF measurement, the antenna pairs perform range detection in frequency stepping mode driven by a vector network analyzer (VNA). The network analyzer creates a signal at a certain frequency (ω1) as a voltage waveform on the output port, which excites the antenna to radiate. The scattered wave is then collected by the receiving antenna on the input port (same as the output port for monostatic radars), and the voltage is stored. The network analyzer then continues to generate the next waveform at frequency (ω2) and so on.An important aspect of the stepped-frequency systems is the intermediate bandwidth (IF bandwidth). The IF bandwidth decides how far ω_2 is separated from ω_1, i.e. how many steps to take to cover the whole bandwidth B. The benefit of having a large IF bandwidth is faster acquisition as there are fewer samples to take than in the case of a small IF bandwidth. However, with a small IF bandwidth, the signal-to-noise ratio is much higher than the acquisition time.

An important first step to reconstruct the surface from the time-of-flight measurement is to define the ellipses that contain the reflecting point. This requires knowing the location of the peaks in the time-of-flight measurement. To accurately find out the peak locations, we apply a basis pursuit denoising (BPDN) [63] algorithm to the

measured signal. The BPDN algorithm is a mathematical optimization problem with the form of

$$\min_{x} \frac{1}{2} \| y - Dx \|_2^2 + \lambda \| x \|_1 \tag{2.1}$$

where y represents the measurement vector, x is the solution vector, and D represents the forward matrix. The λ parameter controls the quality of the optimized solution in favor of either accuracy, i.e. the least square error, or sparsity of the solution. The BPDN method can also be seen as a basis pursuit method with an L1 norm regularizer to penalize complex solutions [64].

For a reflected frequency signal over a bandwidth of B, an overcomplete dictionary D with a frequency response from the sub-resolution distance is constructed. The BPDN problem is then solved to extract the peaks in the time-of-flight measurement. Each of these peak distances then makes up an ellipse around the transmitter and receiver because the sum of the path lengths from both transceivers to the reflector remains the same for all possible points. Figure 2.4 demonstrates the result of using the BPDN method to find the peak in the time-of-flight measurement.

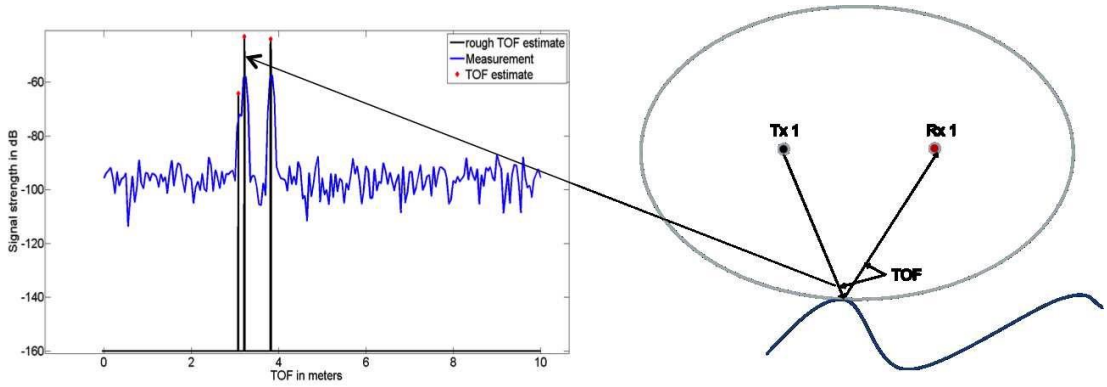

Figure 2.3 Demonstration of time-of-flight measurement simulated by method of moments, with peak detection and the corresponding ellipse

The next part of this method is to figure out which part of the ellipses actually coincide with the real surface. This returns one or several patches on each ellipse and should collectively represent the part of the surface that is reflective.

Without a prior knowledge of the surface, the best patches are found by testing each point of the ellipse that formed each bistatic pair. To test whether a point is a possible reflector for a specific bistatic pair, an imaginary half circle can be drawn tangent to the ellipse at that point and oriented to the normal of incidence. The test then simulates the time-of-flight measurement with all bistatic pairs, as if this circle is the target surface. This is done by finding the points that reflect under the bistatic pair geometrically, and then calculating the path length of that point for that bistatic pair. The error of simulated measurement with the original measurement is then computed to give weight to the point being tested. The assumption taken here is that if this point really lies on the reflecting surface, which is a continuous surface and is represented as a half circle, then the

simulated time-of-flight using this imaginary circle should have the highest correlation among simulated time-of-flight at other points. The test results are in patches on the ellipse and are estimated reflectors. Fig. 2.4 (a) and (b) show the testing schemes for two different points along an ellipse where in (a), the point being tested is on the actual surface, but the point in (b) is not. Fig. 2.4 (c) and (d) show the simulated measurements with all transceiver pairs. Fig. 2.4 (e) and (f) show the real measurement compared to the two simulated measurements. Therefore, the point being tested in Fig. 2.4 (a) has much higher weight than the one tested in Fig.2.4 (b).

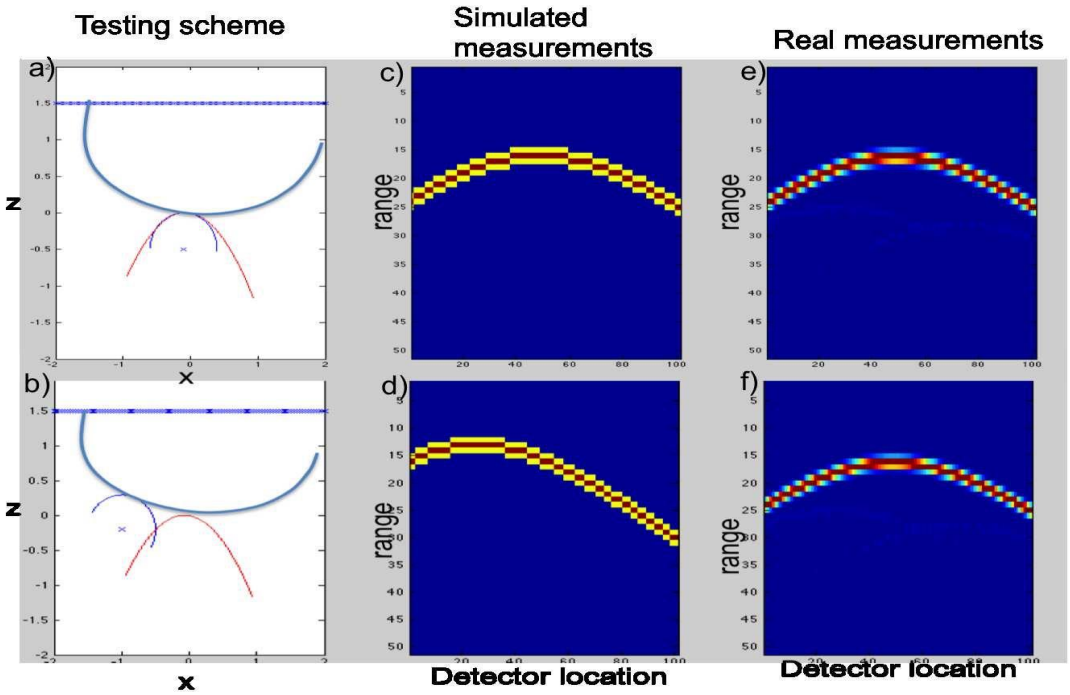

Figure 2.4 Testing scheme for surface estimation

(a)-(b) Testing scheme for a point that is one the surface vs point not on the surface. (c)-(d) Simulated measurement of the testing circles. (e)-(f) real time-of flight measurement of the surface

Here we show a simulation result of testing points on time-of-flight ellipses with the above method. The target object surface for the simulation is a 2D curve, as shown in Fig. 2.5 (a). The time-of-flight measurements from a set of 5 randomly placed bi-static transceivers are simulated numerically using the 2D method of moments (MOM) [65, 66]. The goal is to find an estimation of the 2D curve from these simulated measurements. The incident field is simulated as a tapered Gaussian beam with E-polarization at near field. The induced current on the surface structure is solved, and the reflected signals at the receiver locations are simulated. The patches of ellipses that are the closest estimation of the surface have been highlighted and shown in Fig 2.5 (a) and (b). In this experiment, the red curve is the target surface, and the time-of-flight measurement is simulated with the method of moments. The transmitter locations are labeled with blue dots, and receivers with red dots. Fig 2.5 (a) shows the results of finding patches by testing points on each of the labeled ellipses. Fig 2.5 (b) shows the final result of the reconstruction where the green curve is the truth, and the red curve is the reconstruction. It can be seen from the selected

patches of the ToF ellipses that a reliable reconstruction of this 2D curve can be acquired.

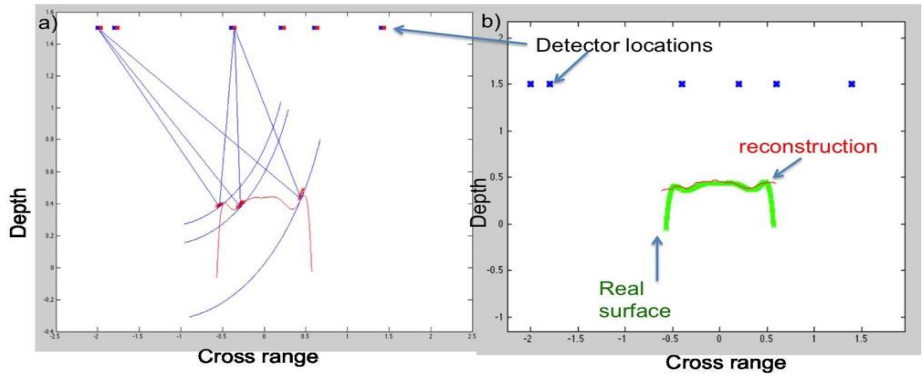

Figure 2.5 Results of elliptical patch selection algorithm

(a) Result of patch selection for three ellipses. (b) Final result after smoothing all selected patches

However, this method is computationally inefficient because the test has to be done at every point on the ellipse and for each bistatic pair. If a system utilizes N transceivers that make N! bi-static pairs, discretizing the reconstruction space into M pixels results in M×N! forward simulation and tests to be made, which is unrealistic for real-world applications, such as 3D surface reconstruction. The following improved method is much faster, but uses a surface prior to constrain the reconstruction. The goal is still searching for the patches of ellipses that can represent the surface collectively. With the surface constraints, this can be done by minimizing the distance and angle between the ellipses' points and the surface prior.

For each point p_i on the surface prior, the total time-of-flight to each bistatic pair is being calculated and a weight characterizing the difference between the path length to p_i and the pathlength to the reflecting point, i.e.,

$$d_i^m = \frac{a}{(\|TOF - (L_{TX}^i + L_{RX}^i)\| + \lambda)^\beta}. \tag{2.2}$$

where ToF is the sum of the time-of-flight distances. The terms L_{TX} and L_{RX} denote the distance from point p_i to the transmitter and receiver respectively. λ is a regularization term, and β determines which order of the difference the weighting function depends on. Similarly, we make another weighting function to enforce the point to satisfy the reflecting condition, and to constrain the curvature of the surface prior, we add another weight related to the difference of the slope:

$$a_i^m = \frac{b}{(\|\Delta\theta_i\| + \lambda)^\gamma} \tag{2.3}$$

where $\Delta\theta_i$ is the difference between the tangent angle at point p_i and the angle of the incident plane if point $p_i$were to reflect with the mth bi-static pair. Thus, when the points are close enough to match the time-of-flight measurement, the ones that do not have the same slope as the surface prior will be discarded. We can also choose to weigh the two functions differently by multiplying with coefficients **a** and **b** to favor each aspect. Therefore, the total weight put onto a point pi on the surface prior for a certain bistatic pair m is

$$w_i^m = d_i^m + a_i^m = \frac{a}{(\|TOF - (L_{TX}^i + L_{RX}^i)\| + \lambda)^\beta} + \frac{b}{(\|\Delta\theta_i\| + \lambda)^\gamma} \tag{2.4}$$

Figure 2.6 shows the scheme of selecting a patch of an ellipse to represent point p on the surface prior.

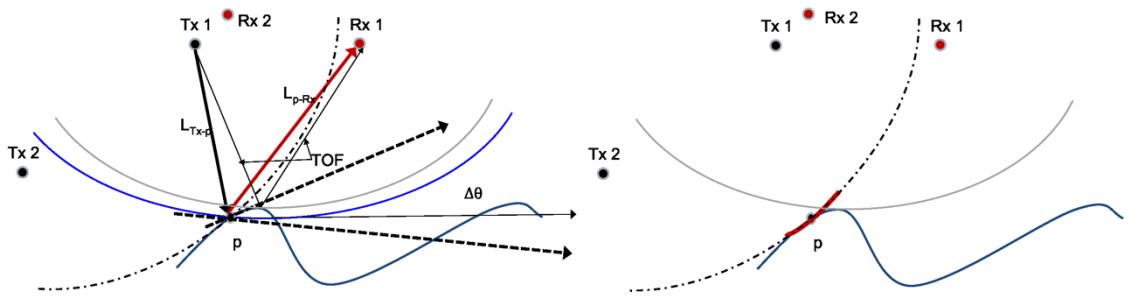

Figure 2.6 Improving the testing scheme by using a prior estimation of the surface

(a) The testing scheme for point pi with two bi-static pairs. (b) The ellipse patch with most weight has been selected for point p_i

After the estimation has been made, it can be optimized iteratively to converge closer to the exact surface. The first step of optimizing the solution is to represent the solution with splines. The best method here is the Catmull-Rom spline representation [67] where the surface passes all the control points and is C1 continuous, i.e., the first order derivatives at the control points are all continuous. This satisfies our requirements of matching the time-of-flight measurement at the control points and having a smooth surface. The control points are set as the center of the selected patches. The general idea of the optimization step is to calculate the time-of-flight with the estimated spline surface, and then minimize the difference with the measured time-of-flight by taking steps to move each control point to the optimal position. The optimization steps are necessary because although the points are on the ellipse, the first surface estimation is not the exact

surface. Therefore, when minimizing the difference of time-of-flight, the selected patch might be off, making it necessary to optimize the control points.

Assume the time-of-flight measurement is g(m,k) for each bistatic pair m and frequency k. A measurement calculated from the surface estimation is denoted as $\tilde{g}$. It can be calculated by geometric optics, i.e. looking for points that would reflect the bistatic pair and calculate the time-of-flight according to these points. We denote the forward model as

$$f(\mathbf{x} : \mathbf{\Gamma}) = \tilde{g} \tag{2.5}$$

where x denotes the vector that contains all the control points x_i, and Γ denotes the corresponding reflectivity vector containing Γ_i. $x{:}\Gamma$ is the concatenated vector of x and Γ. The merit function for the optimization is defined as the difference between the calculated measurement and the real measurement, thus

$$M(\mathbf{x} : \mathbf{\Gamma}) = |g - \tilde{g}|^2 = |g - f(\mathbf{x} : \mathbf{\Gamma})|^2 = \sum_{l=1}^{L} [g_l - f_l(\mathbf{x} : \mathbf{\Gamma})]^2 \tag{2.6}$$

where l is the number of measurement, and L=M×K is the total number measurement, i.e. for each pair and each frequency. We take the derivative of the merit function,

$$\frac{\partial M}{\partial x_i} = -2 \sum_{l=1}^{L} [g_l - f_l(\mathbf{x} : \mathbf{\Gamma})] \frac{\partial f_l(\mathbf{x} : \mathbf{\Gamma})}{\partial x_i} \tag{2.7}$$

where $\partial f_l(\boldsymbol{x}{:}\boldsymbol{\Gamma})$ is essentially the Jacobian J, whose elements can be written as

$$J_{il} = \frac{\partial f_l(\mathbf{x} : \mathbf{\Gamma})}{\partial xi} \tag{2.8}$$

The merit function is minimized by using the Levenberg-Marquardt algorithm [68, 69], where an initial estimation x is given. Note that x : Γ has been replaced with x for notation simplicity. The algorithm calculates the step that x needs to take to converge:

$$\Delta x = [J^T J + \alpha\, diag(J^T J)]^{(} - 1) J^T [g - f(x_0)] \tag{2.9}$$

where α is a regularization term. The surface is then updated with the new control points, and then iterates until the merit function converges below criteria.

2.3 Simulation and experimental results

To validate our algorithm, we experiment with the simulated surface object and time-of-flight measurements to reconstruct the surface shape and reflectivity. When used as a personnel screening technique, the interest is focused on finding the metal pieces under clothing. The target for this simulation is a sectional slice of a human torso and arm, as shown in Figure 2.7 (a), and eight transceivers are placed surrounding the phantom surface, providing 28 bistatic measurements and eight monostatic measurements. The reflectivity simulations, as shown in Figure 2.7 (b)-(d) are done with part of the surface having a different reflectivity corresponding to different situations when imaging a

person for a concealed weapon.

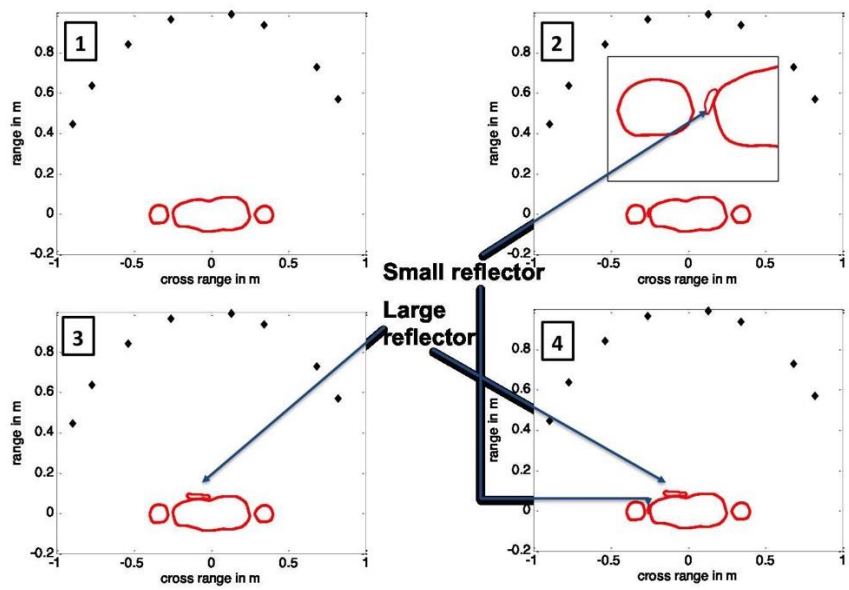

Figure 2.7 Diagram showing the simulation scheme for ToF surface imaging

(a) torso and arm - no reflector, (b) small reflector hidden under arm; inset shows the detailed location of the reflector, (c) large reflector in front of the chest, and (d) small reflector under arm and large reflector in

The result is shown in Figure 2.8 (a)-(d). Figure 2.8 (a) shows the result of the surface reconstruction with no reflector. Figure 2.8 (b) shows the reconstruction with a small reflector. The result recovers the location of the reflector, showing a bright spot between the arm and the torso. The large reflector on the torso is reconstructed and shown in (c), as the high-intensity part represents the large reflector. (d) shows the reconstruction with both reflectors. Since the large reflector piece results in a broader peak with higher

intensity, the contribution from the small reflector is not as significant as in (b).

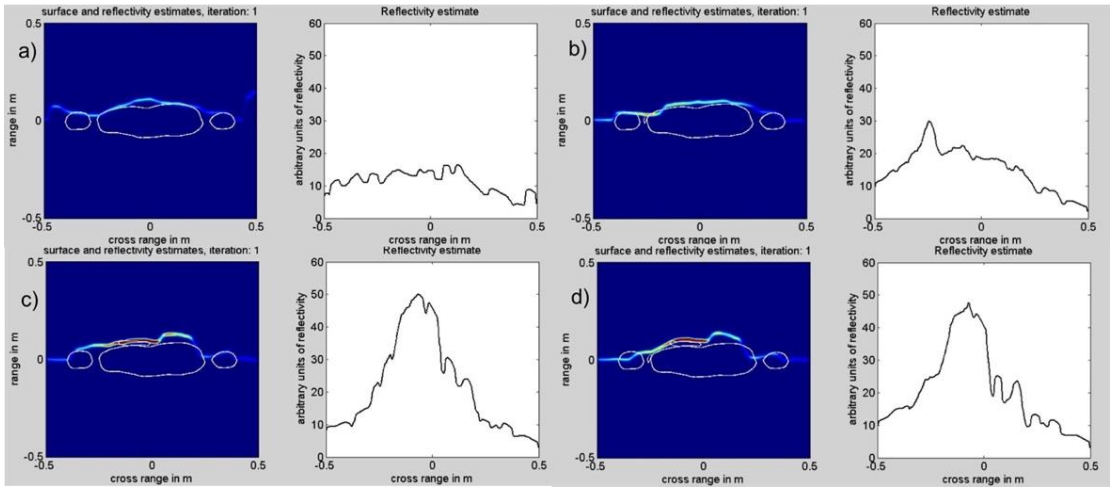

Figure 2.8 Simulation results for ToF surface imaging under different scenario

(a) reconstruction result for body and arm phantom. (b) reconstruction result for small reflector between body and arm. (c) reconstruction result for large reflector. (d) reconstruction result for both large and small reflector being present.

To verify the algorithm works in a real scenario, we set up an experiment to image a reflecting surface as shown in Fig 2.9 a-b). The chosen target is a metal bucket with a 0.5m radius that well represents a cylindrical reflecting surface. The goal is to form a reliable reconstruction of the surface profile in 2D, i.e., one-dimensional cross-range and one-dimensional range, within the field-of-view of the system. The frequency stepping system operates at the K-Band from 18GHz to 26.5 GHz, driven by a VNA. The transceivers are rectangular horn antennas with 6dB gain for the K-Band. To form bi-static transceiver pairs, we used two translational stages for each of the horns to mimic an array of transceivers. Fig 2.9 (b) shows the transmitter and receiver locations where the horns

increment in a 10-mark order Golumb ruler [70] pattern sequentially. A Golomb ruler is a set of integer points along an imaginary axis so that no pair of two points has the same distance. The purpose of the Golomb ruler arrangement is so each bi-static pair results in distinct time-of-flight measurement. The effective aperture size is 1.5m, and the target is placed 1.3m away from the horns.

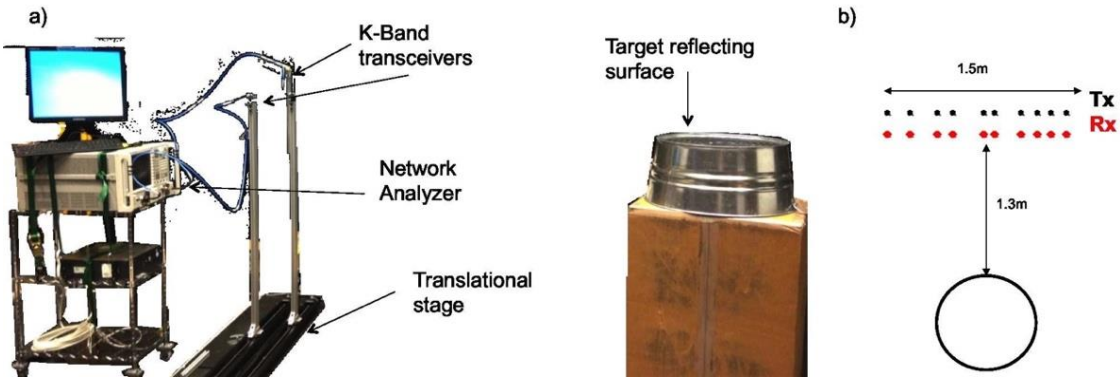

Figure 2.9 Experimental setup of the K-band ToF surface estimation system

(a) Physical setup of the experiment. (b) The locations of the transmitter (Tx) and receivers (Rx) in a Golomb ruler pattern.

The result of reconstruction is shown in Fig 2.10. Fig 2.10 a) shows the reconstruction of the bucket with an arbitrary initial surface estimation. The white curve here is the ground truth of the bucket surface shape, i.e., a circle. As shown in Fig 2.10. a-2) and a-3), the reflectivity has converged to a correct reconstruction. The reconstructed surface reflectivity is strong at the center of the aperture compared to the outer parts. This is because reflection occurs the most when the tangent is parallel or nearly parallel to the transceiver alignment. Therefore, the reflectivity profile shows a relatively much higher peak at the center than the rest of the surface. To improve this situation, a circular

transceiver arrangement circumscribing the object may give a better result. Fig 2.10 a4) shows the convergence of the solution by optimizing the merit function.

To test whether our algorithm is able to reconstruct a more complicated scheme, a piece of wood board is placed in front of the bucket so that we are able to create a surface with non-uniform reflectivity. Fig 2.10 (b) shows the reconstruction results, b1) shows the surface estimation after iterations, and b2-3) shows the reflectivity profile. It can be seen that the reflectivity profile has a clear dip at where the piece of wood was placed. It can also be seen in b3) that a dim section appears on top of the curve.

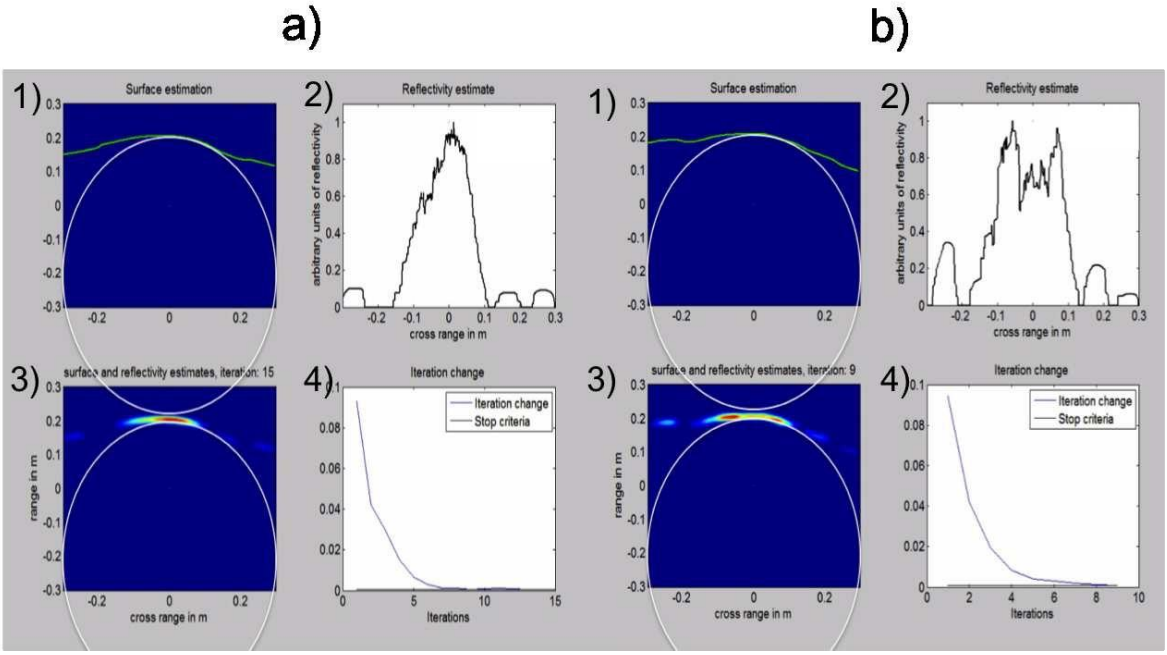

Figure 2.10 Experimental results of the K-band ToF surface estimation

a1) Surface estimation of the metal bucket (white curve is the ground truth). a2-3) Surface reflectivity estimation. a4) Iteration changes during optimization steps. b1-4) Reconstruction result for the scheme with a piece of wood in front of the bucket

2.4 Conclusion

The ultimate goal of this algorithm is to detect surface profile and reflectivity in a three-dimensional scheme, which can be applied to imaging or personnel screening. The difference between the two-dimensional and three-dimensional schemes is that the ellipses we get with time-of-flight measurements become ellipsoid in space. Computationally, working in a 3-D scenario is much more expensive than calculating two-dimensional cases. Therefore, algorithm adaptation to three-dimensional reconstruction must be made to reduce computation cost.

One method to reduce the computation cost is to selectively put points into the forward model to generate estimation $\tilde{g}$ during optimization steps. This can be done by starting to calculate only with a very sparsely down-sampled version of surface estimation. The tangents for any four points defining a square grid can imply the ranges of possible tangent angles inside the surface patch. Therefore, if a large patch is expected to have points that are able to reflect, we can go on to refine the grid points and iteratively refine the patch where the points may reflect. This prevents us from taking into account the surface patches with no reflectors, saving calculation time.

Another improvement is finding out the optimum transceiver locations. As seen in the above examples, a non-optimized transceiver arrangement results in non-uniform sensitivity across the reflecting surface, and thus, a better-arranged sensor array is desired.

3. Compressive sensing and adaptive sampling applied to millimeter wave inverse synthetic aperture imaging

3.1 Introduction

Compressive sensing (CS) algorithms [14, 15] are increasingly being adapted for image acquisition because they may increase the dimension of images, such as by adding side information to resolve spatial images spectrally and temporally as well [107]. They also significantly improve single detector imaging methods by increasing the sampling speed and efficiency over raster-scanning [95], as demonstrated in applications as diverse as optical coherence tomography (OCT) [108], single photon imaging [109, 110], infrared imaging [111], millimeter wave imaging [114], and x-ray imaging [112, 113]. CS achieves this by overcoming the Nyquist sampling limit, requiring only a few samples to reconstruct the original signal if it is sparse on some basis, such as the wavelet basis [115]. Instead of measuring a full data set, the single pixel detector may only need to acquire a few well-chosen samples to achieve a reliable reconstruction. Consequently, sampling strategies [21] have become a topic of great interest, especially CS-based adaptive sampling algorithms [17]. These are sequential sampling methods that improve the sampling efficiency by inferring which points to sample next using knowledge of prior samples.

CS algorithms have already been applied to MMW SAR and ISAR imaging [42，95, 116, 117]. It was shown in [42，95] that compression can be done on the spatial and spectral data by random sampling and reconstructions using various CS algorithms. The primary random sampling strategies include random spatial sampling, random spectral sampling, and random spatial-spectral sampling. Random spatial-spectral sampling provides the best compression rate because of the huge amount of spatial-spectral data acquired. However, if the objective is to minimize acquisition time by reducing the amount of mechanical scanning, random spatial sampling is far superior to random spectral and random spatial-spectral sampling, even though the data compression rate is lower.

When MMW imaging is being used to image through obscurants, the complexity of the scene is unknown [3, 4, 17, 118]. Consequently, random sampling strategies are problematic because the number of samples needed cannot be predetermined. Adaptive sampling provides a compelling alternative that optimizes the measurement scheme regardless of the scene complexity, thereby minimizing the amount of spatial scanning required, especially for ISAR. In a proof-of-concept demonstration of an adaptive sampling CS algorithm applied to MMW SAR imaging, Mrozack et al. accurately located point scatterers in as many steps, but the algorithm was of limited utility because of its requirement that the exact number of scatterers in the scene must be known in advance [17]. Here we introduce an ISAR method that adaptively selects each measurement

location based on the Bayesian compressive sensing (BCS) framework [119, 120] and needs no prior information on the scene complexity. The need for BCS applied to MMW ISAR was borne out of a need for a faster way to obtain high quality reconstructions of complex targets using a single heterodyne MMW transceiver. The current methodologies require mechanically scanning the target sequentially through many angles. This mechanical scanning is slow and further wastes time by measuring many angles that provide little critical information for the reconstruction. In contrast, range is determined by rapid electronic frequency sweeps, so there is no need for BCS in the range dimension. Therefore, by developing a methodology to identify which few angles can provide the most critical information needed for a reconstruction, we can avoid measuring angles that provide little additional information and speed up acquisition. We show that the adaptive algorithm converges faster than random sampling for simple targets and generates more reliable reconstructions for complex targets. In addition, the BCS framework allows the user to define stopping criteria without prior knowledge of the scene.

3.2 Modeling Inverse Synthetic Aperture Radar (ISAR) imaging

Other 2D imaging modalities directly sample in the x-y domain to render a target scene with reflectivity $\rho(x, y)$, but ISAR (and computational tomography (CT)) are sampled in the angle-range domain $f(\theta, r)$. Figure 3.1(a) illustrates how this is done for traditional MMW ISAR imaging in which either the target or the imaging system is rotated and the interrogating beam from a transceiver horn antenna is directed toward the center

of the scene at a sequence of angles θ_i and frequencies ν. As shown in Figure 3.1(b), the same transceiver antenna measures the reflected signal $F(\theta_i, \nu)$ using a vector network analyzer to record the S_{11} parameter at each angle over a range of frequencies. The transceiver antenna is then moved to the next θ_{i+1} and the measurement process is repeated until $F(\theta_i, \nu)$is acquired at all angles and frequencies. From this we can represent the scene in the desired $f(\theta, r)$ angle-range domain, where range r is measured from the center of the scene by a simple Fourier transform

$$\mathrm{f}(\theta, \mathrm{r}) = \int F(\theta, \nu) e^{j2\pi\nu r} d\nu \quad . \tag{3.1}$$

Figure 3.1(c) plots an example of $f(\theta, r)$, which bears a resemblance to the sinograms acquired in CT imaging as scattering elements in the scene rotate closer or farther from the transceiver. Since the range data represents the strength of the reflected signal in a given direction, $f(\theta, r)$ is related to $\rho(x, y)$by the Radon transform

$$f(\theta, r) = \iint \rho(x, y) \delta(x\cos\theta + y\sin\theta - r) dxdy \ . \tag{3.2}$$

The reflectivity function can be easily reconstructed by a filtered back projection (FBP) [121]

$$\rho(x, y) = \int_0^{\pi} f'(\theta, x\cos\theta + y\sin\theta) d\theta \quad , \tag{3.3}$$

where $f'(\theta, r)$ denotes the range data that has been high-pass filtered with a ramp filter to improve the result. Figure 3. 1(d) illustrates the reconstruction obtained by applying the FBP algorithm to the range data in Figure 3.1(c).

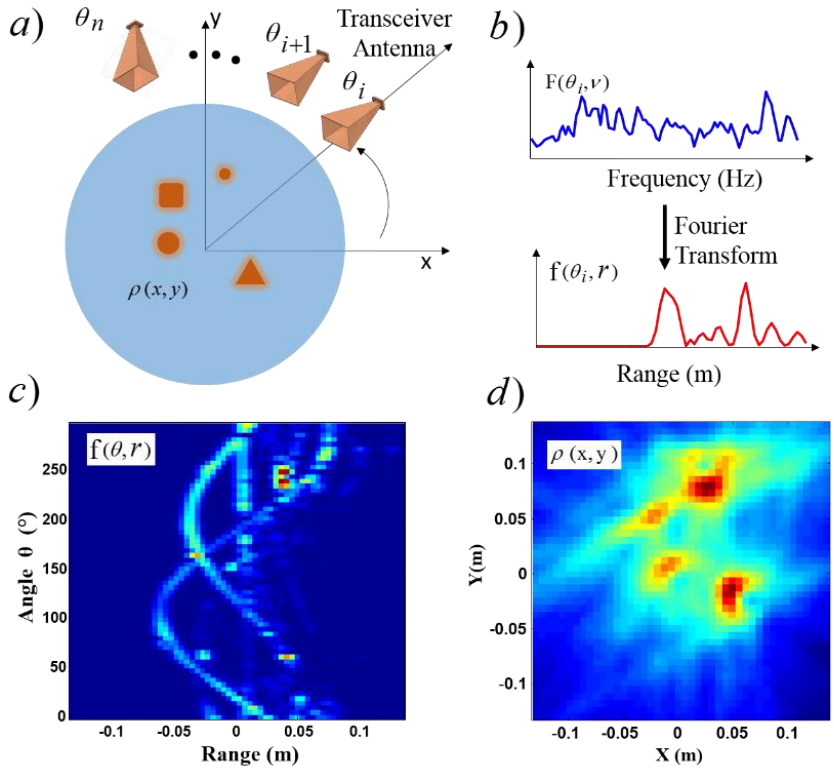

Figure 3.1 Basic setup and data acquisition of traditional ISAR imaging systems

(a) Imaging configuration for traditional ISAR imaging. (b) Example of a measurement at a single angle in the frequency domain $F(\theta_i,\nu)$ and the range data in the spatial domain obtained by Fourier transform. (c) Complete range data of all angles $f(\theta,\mathrm{r})$. (d) Reconstruction of the reflectivity function $\rho(x,y)$ by filtered back projection.

To model the measurement process, we describe the forward model as

$$g(\theta,\mathrm{r}) = \iint h(\theta-\theta',\mathrm{r}-\mathrm{r}')\,\mathrm{f}(\theta',r')d\theta' dr' \tag{3.4}$$

where $g(\theta,r)$ denotes the measurement of $f(\theta,r)$, and $h(\theta,r)$ is the transfer function that describes the sampling scheme. The model should be discretized since the samples are discretized, so

$$g_{\Delta}(\theta,r)=\sum_{n=1}^{N}\sum_{m=1}^{M}h_{\Delta}(\theta-m\Delta\theta',\mathrm{r}-n\Delta r')\mathrm{f}(\mathrm{m}\Delta\theta',n\Delta r') \tag{3.5}$$

where $\Delta\theta$ and Δr denotes the sampling interval in the angular and range domain, respectively, $M=2\pi/\Delta\theta$ is the total number of angular samples, and $N=R/\Delta r$ is the total number of range samples. From Eq. (3.5) a vectorized expression of the model becomes

$$\mathbf{g}=\mathbf{Hf}\ , \tag{3.6}$$

where g is the measurement vector of size MNx1, H is the MN x MN forward matrix, and f is the MN x1 vector as the target for reconstruction. For the ISAR scenario illustrated in Figure 3.1(a), the transceiver measures range data by means of a frequency sweep at angle θ_m, so if a single element in g is denoted $g(\theta,r)|\begin{matrix}\theta=m\Delta\theta\\ r=n\Delta r\end{matrix}$ and labeled $\boldsymbol{g_{mn}}$, the data collected at angle θ_m, become $\boldsymbol{g}=[\boldsymbol{g_{m1}};\boldsymbol{g_{m2}};\dots;\boldsymbol{g_{mn}}]$. The corresponding transfer function may be described as $\boldsymbol{h}=[\boldsymbol{h_{m1}},\boldsymbol{h_{m2}},\dots;\boldsymbol{h_{mn}}]^{\boldsymbol{T}}$, where $\mathbf{h_{mn}}=\delta(\theta-m\Delta\theta,r-n\Delta r)$ describes the sampling of a point in the angle-range domain. The objective is to minimize the time required to obtain f.

To see how this is done, we next discuss the adaptive sampling strategy under the compressive sensing framework. Instead of sampling at all M angles, f can be sampled incompletely with only K samples (K<M) and be reconstructed using the compressive sensing algorithm. We assume f needs to be sparse or sparse under wavelet representation for compressive reconstruction. Thus we chose to represent f by the Haar wavelets, resulting in the wavelet coefficients $\boldsymbol{\omega}$. We denote the Haar wavelet basis as an $MN\times MN$

matrix $\mathbf{B}$, so that $\mathbf{f} = \mathbf{B}\boldsymbol{\omega}$. The compressive measurement can thus be expressed as $\mathbf{g} = \mathbf{HB}\boldsymbol{\omega} = \boldsymbol{\Phi}\boldsymbol{\omega}$, where $\boldsymbol{\Phi} = \mathbf{HB} = [\mathbf{r}_1 ... \mathbf{r}_K]^T$ is the projection matrix relating the wavelet coefficients $\boldsymbol{\omega}$ to the compressive measurements, and a single measurement is simply $\mathbf{g}_k = \mathbf{h}_k^T \mathbf{B}\boldsymbol{\omega} = \mathbf{r}_k^T \boldsymbol{\omega}$. Note that here we use the notation $\boldsymbol{g_k}$ instead of $\boldsymbol{g_m}$ to differentiate that the former corresponds to the compressive measurement. The sparse measurement constitutes an ill-posed inversion problem, which is commonly solved via L-1 regularization, i.e.

$$\hat{\omega} = \arg\min_{\omega} \left\{ \|\mathbf{g} - \Phi\omega\|_2^2 + \lambda \|\omega\|_1 \right\} \tag{3.7}$$

where λ is the regularization coefficient that controls the sparseness of the estimation result. However, the L-1 regularization only provides a point estimate, which gives no access to adaptively choosing the optimal next measurement. Others [119, 120] have formulated the CS inversion from a Bayesian learning point of view, providing a posterior density function on the signal under reconstruction. Besides the improved accuracy of point estimation, the full posterior density function results in confidence intervals on the estimation and thus provides an objective to optimize the next measurement. Therefore the BCS framework is not only able to reconstruct the original data compressively using much fewer measurements, it also provides a way to find the next projection $\boldsymbol{r}_{K+1}$ after each measurement. This property of the BCS framework makes it a popular choice to achieve adaptive sampling in many imaging modalities. This paper focuses on how to use the full posterior density function to form the next projection $\boldsymbol{r}_{K+1}$ in the projection matrix

Φ, then how to realize the corresponding sampling scheme h_{k+1} in ISAR. The theoretical framework for the BCS algorithm is next outlined, following [119, 120], to explain how it reconstructs the original signal and formulates the optimization method for choosing the next measurement angle.

3.3 Baysian Compressive Sensing framework for adaptive ISAR

The compressive measurement can be expressed as the projection of the significant wavelet coefficients ω_s, the remaining insignificant wavelet coefficients, ω_e, and the measurement noise nm. Thus the measurement g can be expressed as

$$\begin{aligned} \mathbf{g} &= \Phi\omega + \mathbf{n}_m \\ &= \Phi\omega_s + \Phi\omega_e + \mathbf{n}_m \\ &= \Phi\omega_s + \mathbf{n} \end{aligned} \tag{3.8}$$

The elements in the generalized measurement noise n are approximated as zero-mean Gaussian distribution with variance σ^2. Thus, the likelihood for the measurement is

$$p(\mathbf{g} \mid \omega_s, \sigma^2) = (2\pi\sigma^2)^{-K/2} \exp\left(-\frac{1}{2\sigma^2} \|\mathbf{g} - \Phi\omega_s\|^2 \right) \tag{3.9}$$

For a compressive sensing problem where the signal is assumed to be sparse in the wavelet basis, a sparseness prior must be placed in the Bayesian formulation. A widely used sparseness prior is the Laplace density function [116, 119, 120]. The conventional CS conversion resulting in the solution of Eq (3.7) can be seen as the maximum a posteriori (MAP) estimation of ω [119, 120]. However, using the Laplace density function as a sparsity prior results in a Bayesian inference that cannot be calculated in closed form

because the Laplace prior is not conjugate to the Gaussian likelihood shown in Eq (3.9). Previous authors [119, 120] have provided a solution using the relevance vector machine (RVM) framework that imposes a hierarchical prior with similar properties but are conjugates to the Gaussian likelihood in Eq (3.9). A zero-mean Gaussian prior is first defined on ω,

$$p(\omega \mid \boldsymbol{\alpha}) = \prod_{i}^{N} \mathrm{N}\left(\omega_i \mid 0, \alpha_i^{-1}\right) \tag{3.10}$$

where α_i is the inverse variance indicating the precision. The second level is a Gamma prior on the hyper-parameter $\boldsymbol{\alpha}$,

$$p(\boldsymbol{\alpha} \mid \mathrm{a}, \mathrm{b}) = \prod_{i}^{N} \Gamma\left(\alpha_i \mid \mathrm{a}, \mathrm{b}\right) \tag{3.11}$$

The final prior on ω is thus derived by marginalizing over $\boldsymbol{\alpha}$,

$$p(\omega \mid a, b) = \prod_{i}^{N} \int_0^{\infty} \mathrm{N}\left(\omega_i \mid 0, \alpha_i^{-1}\right) \Gamma\left(\alpha_i \mid \mathrm{a}, \mathrm{b}\right) d\alpha_i \tag{3.12}$$

Note that the integral in Eq (3.12) results in the Student-t distribution [120]. This prior function can thus promote sparseness by choosing the right values for a and b so that it reaches maximum when $\omega_i = 0$.

For the noise in the measurement, i.e. **n** in Eq (3.8), a similar hierarchical prior is placed with α_0 as the inverse variance of the noise,

$$p(\mathbf{n} \mid a, b) = \prod_{i}^{K} \int_0^{\infty} \mathrm{N}\left(n_k \mid 0, \alpha_0^{-1}\right) \Gamma\left(\alpha_0 \mid \mathrm{c}, \mathrm{d}\right) d\alpha_i \tag{3.13}$$

The posterior covariance and mean are respectively given by [15]

$$\mathbf{\Sigma} = (\alpha_0 \Phi^T \Phi + A)^{-1}$$
$$\boldsymbol{\mu} = \alpha_0 \Sigma \Phi^T \mathbf{g} \tag{3.14}$$

where $\mathbf{A} = diag(\alpha_0, \alpha_1, ..., \alpha_N)$. The goal thus becomes searching for the precision α and α_0. The marginal likelihood for α and α_0 can be derived by marginalizing over the weights $\boldsymbol{\omega}$, following a type-II maximum likelihood (ML) procedure [120], i.e.,

$$\begin{aligned} \mathrm{L}(\boldsymbol{\alpha}, \alpha_0) &= \log p(\mathbf{g} \mid \boldsymbol{\alpha}, \alpha_0) \\ &= \log \int p(\mathbf{g} \mid \boldsymbol{\omega}, \alpha_0) p(\boldsymbol{\omega} \mid \boldsymbol{\alpha}) \, \mathrm{d}\boldsymbol{\omega} \\ &= -\frac{1}{2}[\mathrm{K} \log 2\pi + \log |\mathbf{C}|] + \mathbf{g}^T \mathbf{C}^{-1} \mathbf{g} \end{aligned} \tag{3.15}$$

where $\mathbf{C} = \sigma^2 \mathbf{I} + \mathbf{\Phi} \mathbf{A}^{-1} \mathbf{\Phi}^T$. The point estimates for α and α_0 from type II-ML maximizing the likelihood yields

$$\alpha_i^{new} = \frac{\gamma_i}{\mu_i^2}$$
$$\alpha_0^{new} = \frac{K - \Sigma_i \gamma_i}{\| \mathbf{g} - \mathbf{\Phi} \boldsymbol{\mu} \|_2^2} \tag{3.16}$$

where μ_i is the i-th posterior mean from Eq (3.8), and $\gamma_i = 1 - \alpha_i \Sigma_{\mathrm{ii}}$ [119, 120]. α and α_0 are then used to calculate $\mathbf{\Sigma}$ *and* $\boldsymbol{\mu}$ using Eq. (14) again, which constitutes an iterative process that updates these parameters until convergence occurs. The fact that α and α_0 can be updated iteratively indicates that initializing the a, b, c, d parameters for the hierarchical Gamma priors in Eq (3.12) and Eq (3.13) is not necessary in this case. Thus, setting them equal to zero is equivalent to enforcing a uniform prior on α and α_0 [119].

Since the signals being reconstructed are the wavelet coefficient of the original signals, where $\mathbf{f} = \mathbf{B}\omega$, the expectation and covariance of the posterior density function can respectively be derived as

$$\begin{aligned} E(\mathbf{f}) &= \mathbf{B}\boldsymbol{\mu} \\ Cov(\mathbf{f}) &= \mathbf{B}\boldsymbol{\Sigma}\mathbf{B}^{\mathbf{T}} \end{aligned} \tag{3.17}$$

where the diagonals of $\boldsymbol{\Sigma}$ indicate the level of accuracy (or uncertainty) on the reconstruction of elements in $\mathbf{f}$ [119].

The ability to measure uncertainty provides criteria for selecting the next best measurement to minimize the total number of samples needed to reconstruct the signal with significant fidelity. The differential entropy is one criterion that satisfies the purpose [119, 120], where

$$\begin{aligned} \mathrm{S(f)} &= -\int p(f)\log p(f)df \\ &= \frac{1}{2}\log|\mathbf{B}\boldsymbol{\Sigma}\mathbf{B}^{T}| + \mathrm{const} \\ &= \frac{1}{2}\log|\boldsymbol{\Sigma}| + \mathrm{const} \\ &= -\frac{1}{2}\log|\mathbf{A} + \alpha_0\boldsymbol{\Phi}^{\mathbf{T}}\boldsymbol{\Phi}| + \mathrm{const} \end{aligned} \tag{3.18}$$

With a new measurement, $\boldsymbol{\Phi}$ is modified by adding a new row ${r_{k+1}}^{T}$; thus, the new entropy after the next measurement derived in [119] is

$$S_{new}(\mathrm{f}) = h(\mathrm{f}) - \frac{1}{2}\log|\mathbf{A} + \alpha_0{\mathbf{r}_{K+1}}^{\mathbf{T}}\boldsymbol{\Sigma}\mathbf{r}_{K+1}| \tag{3.19}$$

The goal of making the next possible measurement becomes defining r_{K+1} so that the new entropy $S_{new}(f)$ is minimized, so the maximum of ${\boldsymbol{r}_{K+1}}^{T}\boldsymbol{\Sigma}\boldsymbol{r}_{K+1}$ should be

pursued. In addition, as pointed out in [120], maximizing $\boldsymbol{r}_{K+1}{}^{T}\boldsymbol{\Sigma}\boldsymbol{r}_{K+1}$ is equivalent to maximizing the variance of the next measurement, since

$$\begin{aligned}\mathbf{r}_{K+1}{}^{\mathbf{T}}\boldsymbol{\Sigma}\mathbf{r}_{K+1} &= \mathbf{r}_{K+1}{}^{\mathbf{T}}Cov(\omega)\mathbf{r}_{K+1} \\ &= Var(g_{K+1})\end{aligned} \quad . \tag{3.20}$$

The user may specify a stopping criterion for the algorithm to end based on the desired amount that $\boldsymbol{r}_{K+1}{}^{T}\boldsymbol{\Sigma}\boldsymbol{r}_{K+1}$ changes from iteration to iteration.

Now the question becomes how to find the r_{K+1} that maximizes the variance $\boldsymbol{r}_{K+1}{}^{T}\boldsymbol{\Sigma}\boldsymbol{r}_{K+1}$. Theoretically, the next projection vector r_{K+1} should be designed by performing an eigen-decomposition of $\boldsymbol{\Sigma}$ and letting r_{K+1} be the eigenvector of the largest eigenvalue [119]. Recall that the measurement and target are related by $\mathbf{g_k} = \mathbf{h_k}{}^{\mathbf{T}}\mathbf{f} = \mathbf{h_k}{}^{\mathbf{T}}\mathbf{B}\boldsymbol{\omega} = \mathbf{r_k}{}^{T}\boldsymbol{\omega}$, so to measure the target in its original non-wavelet basis, we use the relationship $\mathbf{h_{k+1}} = \mathbf{B}^{T}\mathbf{r_{k+1}}$ to find the $\boldsymbol{h}_{K+1}$ and design the sampling method. Here, $\boldsymbol{h}_{K+1}$ is in the form of multiplexed sampling given by

$$\mathbf{h}_{k+1} = \sum_{i}\sum_{j}\delta(\theta - i\Delta\theta, \mathrm{r} - j\Delta r) \quad . \tag{3.21}$$

An example illustrating how the projection vector $\mathbf{h_{k+1}}$ is realized under a hypothetical traditional BCS framework is presented in Figure 3.2(a). The colored points in Figure 3.2(a) indicate which points are being sampled in each measurement: orange points depict the transfer function of the k-th measurement $h_k(\theta, r)$ as an overlay on the target function $f(\theta, r)$, and the green points depict the next measurement $h_{k+1}(\theta, r)$. The

formation of the forward matrix H is thus visualized in Figure 3.2 (c) where each row corresponds to a measurement, and multiple points in each row indicate multiplexing. This type of sampling is usually realized with a coded aperture [21] to modulate which pixels to sample. However, this sampling strategy is not practical for ISAR imaging because the transceiver can only measure from one angle at a time. The sampling described in Eq (3.21) requires measuring multiple angles and ranges at the same time, requiring the kind of extensive mechanical movement that we are trying to avoid.

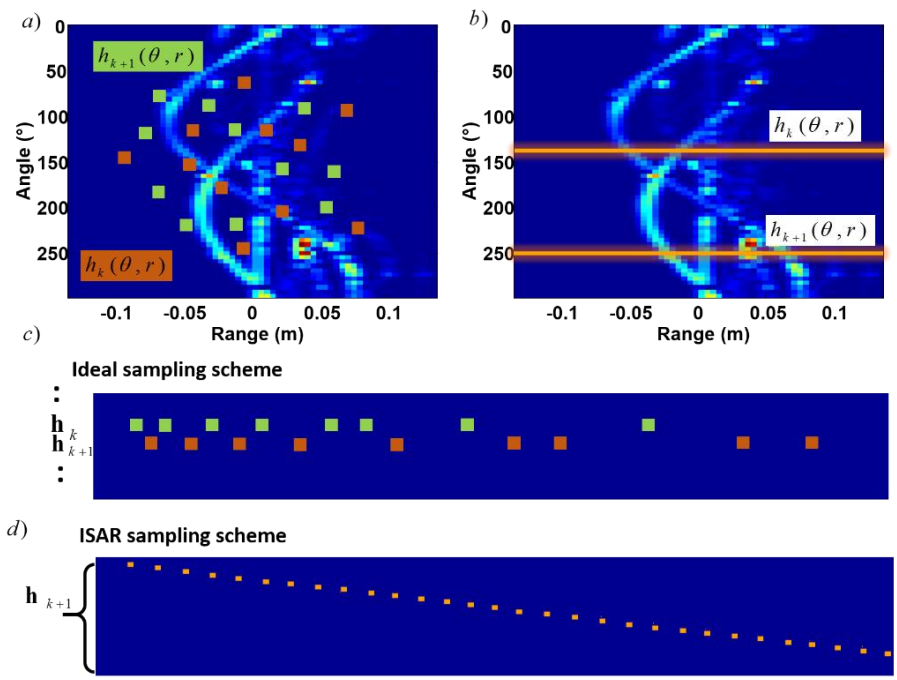

Figure 3.2 Visualization of the ISAR forward model comparing to an ideal multiplexed acquisition model

(a) Visualization of the next measurement under a hypothetical traditional BCS methodology. Colored points indicate the points sampled in step k (orange) and k+1

(green). (b) Visualization of the next measurement for ISAR imaging. (c) Vectorized form of for ideal BCS, and (d) for ISAR imaging.

As noted above, ISAR imposes a constraint when maximizing $\boldsymbol{r}_{K+1}{}^{T}\boldsymbol{\Sigma}\boldsymbol{r}_{K+1}$: all range data are taken for a fixed angle during each measurement, and this is illustrated in Figure 3.2(b). Given that our goal is to minimize the amount of mechanical movement, the sampling choice is thus limited to selecting the next angle θ_i. Due to this constraint, the actual next projection for ISAR imaging cannot be the exact eigenvector that enforces the maximum of $\mathbf{r}_{K+1}{}^{\mathbf{T}}\boldsymbol{\Sigma}\mathbf{r}_{K+1}$, and we lose the advantage of multiplexing the measurement. As a result, the transfer function should be described as

$$\mathbf{h}_{k+1}^{ISAR} = [\mathbf{h}_{k+1,1}, \mathbf{h}_{k+1,2}, ..., \mathbf{h}_{k+1,\mathrm{n}}]^T \tag{3.22}$$

$$\mathbf{h}_{k+1,\mathrm{n}} = \delta(\theta - \theta_{k+1}, \mathrm{r} - n\Delta r) \quad . \tag{3.23}$$

Figure 3. 2(b) and 3.2(d) illustrates the sampling strategy by visualizing the transfer function for the ISAR measurement and its corresponding vectorized form, the transfer matrix. The difference between the typical BCS framework and the application of BCS to ISAR is that there is no multiplexing in the latter [21], so more measurements are required. Therefore, to select the next optimal measurement in ISAR, we have to define a library of all possible $\mathbf{h}_{K+1}$ matrices under to the predefined sampling intervals and choose the one that maximizes the sum of $\mathbf{r}_{K+1}{}^{\mathbf{T}}\boldsymbol{\Sigma}\mathbf{r}_{K+1}$. For example if the user defines 360 samples along the angular domain, such that the angular sampling interval is 1° and M=360, the library consists of 360 possible $\mathbf{r}_{K+1}$ matrices from the beginning. Given the $\boldsymbol{\Sigma}$ from current

measurements, the next measurement is chosen from the remaining 359 angles. Figure. 3.2(c) and 3.2(d) emphases the difference between the theoretical BCS framework and the ISAR BCS framework that is constrained from multiplexing. Under the theoretical BCS framework with the ability to multiplex, the H matrix with K measurements is K x MN where K can be a really small number, thus maximizing compression rate. For ISAR application, the BCS framework loses multiplexing ability and only adaptively choose K angles, thus the H matrix becomes a KN x MN matrix.

3.4 Experiments and Results

Two sets of experiments were performed to test the adaptive sensing algorithm. For both experiments, the sample objects are mounted on a motorized rotational stage. The objects are illuminated by a 15 cm diameter beam folded by and collimated with a mirror. The beam is reflected by the sample object and measured by a single stationary detector. Figure. 3.3 (a) presents a schematic drawing of the experiment setup. The source radiation is generated by a transceiver module frequency swept from 75 to 110 GHz. The reflected signal is analyzed with a network analyzer. The spatial measurement is done by rotating the target on the rotational stage, then obtaining the spectral data and evaluating its Fourier transform.

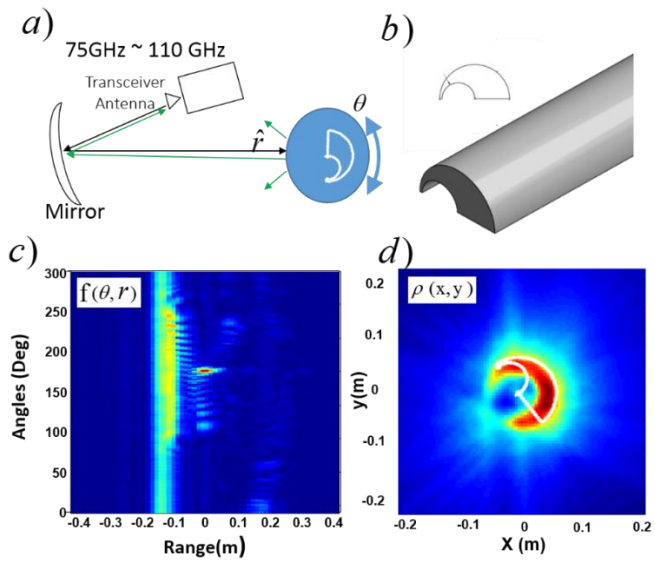

Figure 3.3 Experimental setup for adaptive ISAR with a 3D printed dielectric target

(a) A schematic drawing of the experiment. (b) Drawing of the target half-cylinder nautilus. (c) The range signal measured at 300 angles separated at 0.1 degrees per measurement. The fully-sampled reconstruction is treated as the ground truth for the simulated experiments. (d) The ISAR reconstruction via the filtered backpropagation method with all 3000 measurements.

The sample under investigation is a 3D printed nautilus-shaped dielectric cylinder, shown in Figure 3.3(b). The cylinder is 20 cm tall with outer radius 30 mm and inner radius 14 mm. Figure 3.3 (c) plots the spatial-spectral (i.e. angle-range) data measured at 3000 locations equally spaced between from 0o to 300o. The 180° orientation is depicted in Figure 3.3 (a), and the strong specular reflection from the flat surface is easily seen in Figure 3.3 (c). The range-varying structure between 90°-270° is produced by reflections from the inner cylinder cavity as it rotates closer to the source. The ISAR image can be reconstructed by performing filtered back-projection using the inverse Radon transform

on the measured spatial data. The results, shown in Figure 3.3(d), indicate a faithful reconstruction of the outer half-cylinder surface but a less accurate reconstruction of the "eclipsed" flat surface because of multiple reflection. The full sampling measurements and reconstruction shown in Figure 3.3 (c) and (d) constitute the reference to which the adaptively sampled and reconstructed images will be compared.

The adaptive sensing algorithm described here is based on a Bayesian compressive sensing framework [119，120], which requires the sparsity of the signal. However, the target under investigation may not satisfy the sparsity requirement. We perform a wavelet transform (Haar) on the measured signal in the range domain, which is relatively sparse compared to the signal in the spatial domain, shown in Figure 3.4(a). The wavelet transform provides a representation of the signal in a multi-scale basis [115]. For wavelets with lower order scales, the original signal is represented by a slowly varying basis that produces a few coefficients with large values. For higher order wavelets, the original signal is represented by a version of the original basis scaled with faster variation and smaller windows, generating a large number of coefficients with much smaller values. In Figure 3.4(a), the wavelet coefficients for the target are shown in a vectorized form. The lower order coefficients correspond to the part of the signal with slower variations, whereas the higher order coefficients correspond to faster variations and finer features. The spectrum of the wavelet coefficient also implies the sparsity of the target.

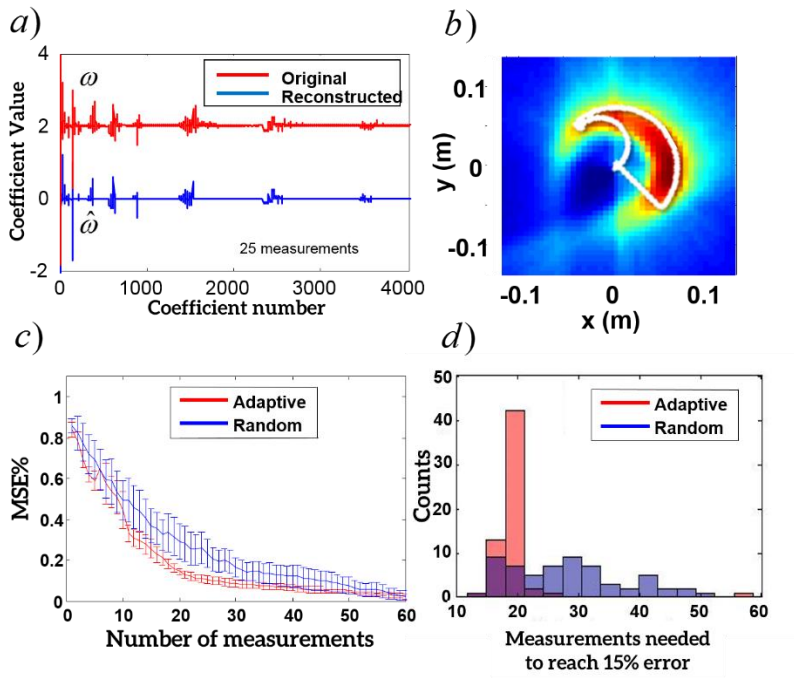

Figure 3.4 Experimental results and analysis for adaptive ISAR reconstruction on the dielectric rod target

(a) The reconstruction of the wavelet coefficient of the signal after 25 measurements. (b) The ISAR reconstruction via filtered back projection on the data with 25 measurements. (c) The average MSE comparison of adaptive spatial sampling and random spatial sampling for 60 simulated experiments. Error bars indicate the standard deviation of the MSE. (d) Histogram of how many measurements the adaptive and random sampling has taken to reach 15% MSE.

The reconstructed signal after 25 adaptive measurements is shown as an offset to the original signal in Figure 3.4(a). From the comparison between the wavelet coefficients of the full measurement and that of the compressed measurement, it can be seen in Figure 3.4 (a) that the reconstruction with the first 25 measurements selected by the adaptive algorithm can restore the original signal. The minor difference in higher order coefficients can be tolerated because they are likely to be the result of noise in the measurement and contribute only a small percentage in terms of energy. The first 25 measurements in the

range domain are reconstructed and back-projected to form the target image shown in Figure 3.4 (b). The white outline depicts the true contour of the target. To assess the reconstruction quality of the compressed adaptive measurement, we measured a 0.944 structural similarity index (SSIM) [122] when comparing to the full measurement reconstruction $\rho(\mathrm{x},\mathrm{y})$ in Figure 3.3 (d). It should be pointed out that the BCS algorithm allows the user to specify a stopping criteria when the change of uncertainty in the measurement is not increasing any more, yet we let the simulated experiment run without stopping to analyze convergence. The goal here is to provide information that can be used to define appropriate stopping criteria.

The idea of using CS techniques to reconstruct the target image from a small subset of all possible measurements has already been demonstrated [14, 15]. It was shown that randomly selecting measurement angles in an ISAR experiment might substantially reduce the number of measurements and thus reduce the amount of mechanical scanning. Using an adaptive algorithm for compressed spatial sampling further improves the efficiency by achieving an acceptable reconstruction faster.

To demonstrate this advantage, we have simulated the experiment 60 times, each starting at a different angle, and compared it to the results of 60 different experiments using random measurements. The result is shown in Fig. 4(c), using the normalized mean squared error (MSE) $\frac{1}{MN}\sum_{i=1}^{MN}\left(f_i-\hat{f}_i\right)^2$ normalized by $\left|\left|f\right|\right|^2$ as the reference criterion. We chose to use the range representation of the scene $f(\theta,r)$ as the benchmark, assuming that

the target and its associated $\rho(x, y)$ are unknown to the observer. It can be seen that the adaptive algorithm approaches low MSE faster than random sampling. Although the advantage tends to saturate when the number of measurements approaches the allowed maximum, the narrow error bars imply that the adaptive algorithm tends to be more stable when approaching convergence as the adaptive algorithm exploits the asymmetry of the target to select which measurements will most increase the information content. A histogram of the number of measurements required to reach 15% MSE further demonstrates the advantage of the adaptive algorithm over random sampling, as shown in Figure 3.4(d). Although it happens that random sampling may converge faster than the adaptive algorithm in some cases, the adaptive algorithm is overall much more reliable and converges more consistently. This is essential when the target has unknown complexity and the number of measurements to be made must be predetermined.

It can also be noticed in Figure 3.4(d), there was one outlier for the adaptive sampling that used all 60 measurements to reach the 15% MSE mark. The outlier is a consequence of the sampling constraints described earlier. Since ISAR has no multiplexing ability, each measurement is constrained to a single angle, and the algorithm must maximize the sum of $\mathbf{r}_{K+1}{}^{\mathrm{T}}\boldsymbol{\Sigma}\mathbf{r}_{K+1}$. Since the constraint may not allow the algorithm to choose the highest eigenvalue of $\boldsymbol{\Sigma}$ and associated eigenvector $\mathbf{r}_{K+1}$, the algorithm's more limited choices may be among lesser $\mathbf{r}_{K+1}$ values that may sometimes produce the same sum of

$\mathbf{r}_{K+1}{}^{\mathrm{T}}\boldsymbol{\Sigma}\mathbf{r}_{K+1}$, and their corresponding angles may differ significantly. Consequently, the algorithm may sometimes choose an angle that does not aid convergence.

Choosing the next measurement angle to maximize variance necessarily minimizes the new entropy, as shown in Eq (3.19). In other words, the algorithm chooses to maximize "new" information with each new measurement. To understand the selection process better, we show in Figure 3.5(a-d) four different stages of one simulated adaptive measurement, i.e. the 4th, 8th, 12th, and 16th adaptive measurement, respectively. The colored lines indicate the four measurement angles added in each sequence. Note that the early measurements are relatively evenly spaced in angle but that the later measurements have identified the thinner "eclipse" section for further scrutiny. These intuitive choices illustrate the algorithm's ability to recognize the part of the target with the most angle-dependent variation in signal.

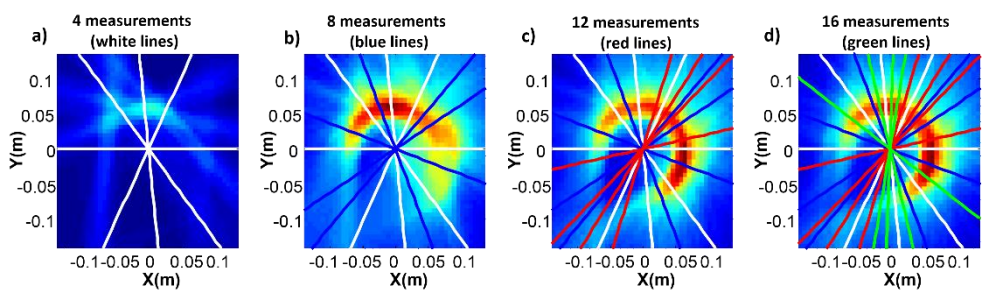

Figure 3.5 Diagram showing the progression of the adaptive algorithm

(a)-(d) Results from the adaptive algorithm after 4, 8, 12, 16 measurements respectively. Lines with different colors indicate the measurements made during each stage, i.e., white lines are the first 4 measurements; blue lines are the 5th-8th measurements. These figures demonstrate the process of adaptive selection.

Are there conditions where adaptive sampling does not have a significant advantage over random sampling? Consider a cylindrical target for which all measurement angles return the same signal. In this case, each measurement would introduce the same amount of uncertainty, and the adaptive algorithm would simply scan every angle. Thus, in scenes with cylindrical symmetry, the adaptive algorithm will not outperform the random sampling strategy.

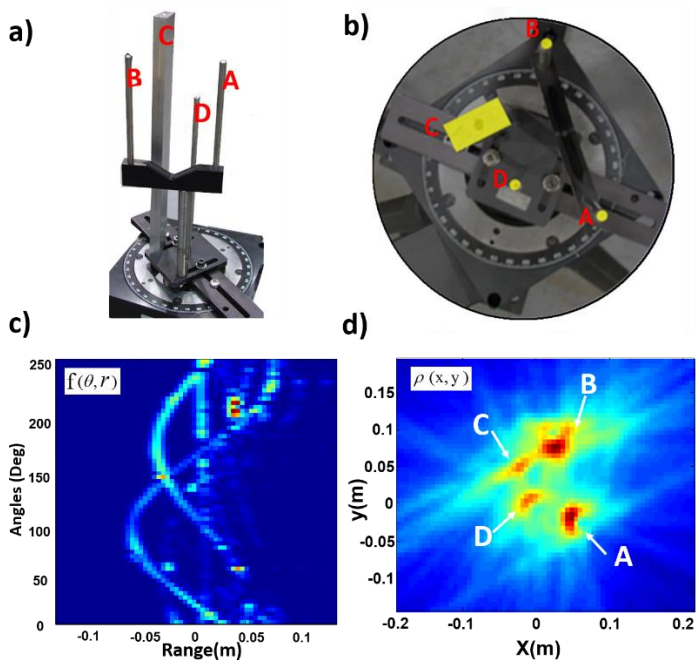

Figure 3.6 Experimental setup for the adaptive ISAR system with a set of metal rods as target

(a) Image of the target from the side and (b) from above. (c) The range signal measured at 300 angles separated at 0.1 degrees per measurement. (d) The ISAR reconstruction via back propagation.

This can be observed in a second experiment involving a simpler target with cylindrical symmetry, composed of four metal posts that appear as point scatterers in the

image. The configuration is shown in , Figure 3.6(a-b), and the range-angle data $f(\theta, r)$ is shown in Figure 3.6 (c) from which $\rho(x, y)$ is reconstructed in Figure 3.6 (d). Although the geometry of this target is simpler than the previous experiment, Figure 3.7(a) reveals that the wavelet coefficients of the measurements in this second experiment are less sparse than that of the first experiment, in part because of the cylindrical symmetry. Figure. 3.7(b) shows the reconstruction of the target with 35 measurements from the adaptive algorithm, which has an SSIM index of 0.917 compared to the benchmark in Figure 3.6(d).

As predicted, the symmetry and non-sparsity impose difficulties for the adaptive algorithm. To compare the adaptive algorithm with the random sampling method, we again simulated 60 different experiments, each starting at a different measurement angle. As expected, the MSE progression of both methods shows that the adaptive algorithm did not outperform the random sampling algorithm as in Figure 3.7(c). The two algorithms tend to approach a given MSE at the same rate. We believe this is due to the geometry of the target, for which most angles introduce a similar amount of uncertainty, so random selection is not an inferior methodology in this scenario. However, the adaptive algorithm still has the advantage of being more consistent, which is shown in Figure 3.7(c) as the uncertainties associated with adaptive sampling are smaller. In addition, the histogram in Figure 3.7(d) indicates how many measurements each algorithm took to achieve an MSE of 15%. The adaptive algorithm tends to achieve this goal in 45-50 measurements, whereas random sampling was less reliable by taking 35-55 measurements.

To characterize the advantage BCS provides, it is not enough to quantify how many fewer measurements were required to achieve a certain MSE. We must also consider the associated time and complexity introduced by the algorithm. According to the proposed method for selecting the next measurement, $\mathbf{r}_{K+1}{}^{\mathrm{T}}\boldsymbol{\Sigma}\mathbf{r}_{K+1}$ must be calculated for all remaining possible angles so that the best $\mathbf{r}_{K+1}$ may be selected, but the extra time for the matrix multiplication to take place is not always negligible. Two factors affect the calculation time: sampling in the range domain, and sampling in the angular domain. When the range domain is heavily sampled with a large spectral bandwidth, $\mathbf{r}_{K+1}$ can be very large and the extra multiplication become a computational burden. Similarly, if the sampling in angular domain is very fine, there are too many possible $\mathbf{r}_{K+1}$ candidates. For example 360° sampled at 0.1° intervals produces 3600 choices for $\mathbf{r}_{K+1}$ at the beginning, dramatically increasing the time required for calculating all $\mathbf{r}_{K+1}{}^{\mathrm{T}}\boldsymbol{\Sigma}\mathbf{r}_{K+1}$ values. However, note that even when these computations slow the time for convergence, the stability and confidence of convergence remains a significant advantage for applying the adaptive BCS algorithm to ISAR imaging. It can be seen from the work presented here that regardless of scene complexity, the adaptive is more reliable than random sampling toward reaching a desired MSE.

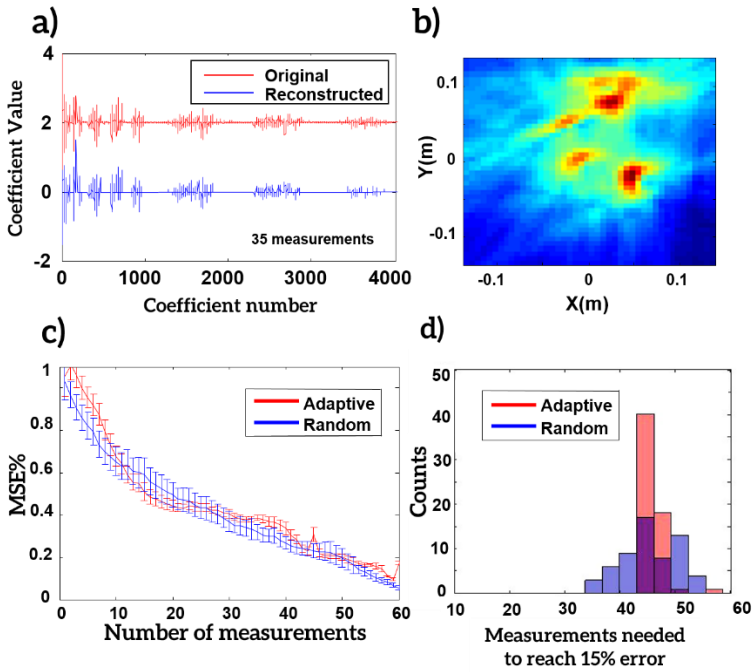

Figure 3.7 Results and analysis for the adaptive ISAR reconstruction of the metal rods target

a) The reconstruction of the wavelet coefficient of the signal after 35 measurements. b) The ISAR reconstruction via filtered back projection on the data with 35 measurements. c) The average MSE comparison of adaptive spatial sampling comparing to random spatial sampling for 60 simulated experiments. Error bars indicate the standard deviation of the MSE. d) Histogram of how many measurements the adaptive and random sampling has taken to reach 15% MSE.

3.5 Conclusion

We have presented an adaptive spatial sampling method for MMW inverse synthetic aperture radar (ISAR) imaging systems. The goal of adaptive imaging in ISAR for single pixel detector systems is to reduce the amount of mechanical scanning and the amount of data acquired in order to reduce acquisition time and minimize noise. We have implemented this adaptive algorithm based on the Bayesian compressive sensing algorithm developed by Carin et. al. [119], utilizing the full posterior estimation

methodology to obtain optimized measurements. As compared to existing random sampling strategies, the advantage of this adaptive algorithm is the experimentally demonstrated ability to reconstruct scenes reliably without prior knowledge of the complexity of the scene.

Our results indicate that the complexity of the scene determines the degree to which this adaptive ISAR sampling strategy is superior to random sampling methods. Specifically, the advantage of this adaptive algorithm is diminished as the complexity or symmetry of the scene increases and illumination from new directions provides little additional information. However, even in these scenarios the convergence is more consistently and reliably reached by adaptive methods.

4. Rapid prototyping of radio frequency passive components

4.1 Introduction

Improving radar imaging with conventional sensors, such as rectangular horns as antennas with computational imaging methods has been the focus of previous chapters. A computational method, such as the adaptive sensing algorithm helps to retrieve information beyond the amount of information acquired with these conventional antennas by reducing the amount of data needed for reconstruction; however, computational imaging alone does not fully employ the potential of radar imaging. Novel antenna design has been a growing interest in the millimeter-wave and radio frequency imaging society [24]. A custom designed antenna for research purposes is hard to manufacture because of the need for high precision mechanical tools and slow design-to-prototype time. A novel method for manufacturing and prototyping antenna and waveguide components that is fast and low-cost is desired. In addition, complicated RF assemblies that involve multiple elements are constructed by connecting various components with waveguides, which often results in numerous joints that increase the size and weight and degrades the performance.

A more efficient way to manufacture microwave devices is using additive manufacturing methods, such as three-dimensional (3D) printing. Waveguide assemblies

can be integrated into a single part without the need for additional interfaces, eliminating adapters [71].Furthermore, 3D printing is able to create complicated structures with high precision without adding difficulty to the manufacturing process; thus, reducing the cost for highly complicated components, such as electromagnetic crystal waveguide [30], corrugated horn antennas [48], and structural electronics [29, 73].

The most important requirement for 3D printing of microwave components is the surface conductivity, i.e., the surface of the part must be conductive in order to guide electromagnetic waves. Thus, the methods for 3D printing microwave components can be categorized as metal printing techniques and non-metal printing techniques. Metal printing techniques, such as electrical beam melting (EBM) [75] and binder jetting (BJ) [74] produce metal surfaces that are rough for high-frequencies, such as K-Band and W-Band frequencies [49, 74]. Not only the costs for metal 3D printers are on the order of millions of dollars, but the weight of metal printed parts is also much higher than plastic parts. On the other hand, as mentioned in the first chapter, the amount of copper needed to achieve good performance is a layer as thick as the skin depth, which is on the order of microns for millimeter wave components. With the development of metalizing techniques, such as plating-on-plastic [76-78], waveguides and antennas that are printed with plastic materials can be metalized to guide electromagnetic waves [26, 46].Thus, non-metal-printing methods combined with a plating-on-plastic technique offer a low-cost solution to making light-weight devices that are metallized only on the necessary surface. Though

the cost and weight have been reduced, the performance of 3D printed waveguides and antennas is comparable to that of those manufactured using traditional methods [48, 53, 79].

Previous efforts in metalizing 3D printed plastic waveguides and antennas include spraying metallic coating [48], printing with the conductive material [73, 80], and electroless copper plating [26, 53]. Spraying metallic paint produces low conductivity and poor surface smoothness. The result could be satisfying for low-frequency antenna applications; however for high-frequency applications, especially when a low loss is desired, a more conductive and smoother surface is required. 3D printing with a conductive material mixture produces a smooth surface; however, the material is made conductive by mixing it with conductive nanoparticles, which gives it a much lower conductivity than pure metal. On the other hand, 3D printers that enable conductive material are limited to fused deposition modeling (FDM) [81] machines whose resolutions are in the millimeter range, thus limiting this method to low-frequency applications. Electroless plating [82] results in a uniform layer of pure copper deposited onto the surface of the part, thus achieving high conductivity and keeping the surface smooth. The electroless plating method satisfies both low and high-frequency waveguide applications, as recently reported by [53]. However, electroless plating is a slow process even with a catalyst, and the plated layer is thin.

This chapter discusses a novel method for low-cost, rapid prototyping metalized 3D printed waveguides and antennas that address the above problems by combining electroless copper plating with traditional electroplating.

4.2 Method

An overview of the procedures for this method is shown in figure 4.1. As a first step, a computer-generated 3-D model of a waveguide or an antenna is designed. When designing the model, certain features, such as split-blocking, alignment pins, and anti-leakage feature, can be incorporated. The model is then printed using a high-resolution 3-D printer of choice, such as stereolithography [84] or polymer jetting [83] 3-D printers. The next step is preparing the 3-D printed part for metalizing by cleaning and oxidation. Oxidation enables the plastic surface to be treated further for a copper seed layer. The seed layer is uniformly deposited by electroless deposition. To thicken the plated layer, the part is then electroplated with copper. The finished parts are then treated with a protective layer to prevent the part from oxidation, rust, and scratches.

A WR42 rectangular waveguide for K-band (18GHz-26.5GHz) was manufactured using this procedure and was first introduced as a demonstration. Designing the waveguide should follow the principle of electromagnetics and waveguide design. A brief introduction to the waveguide theory is introduced for understanding the following

design considerations, such as implementing the split-block feature.

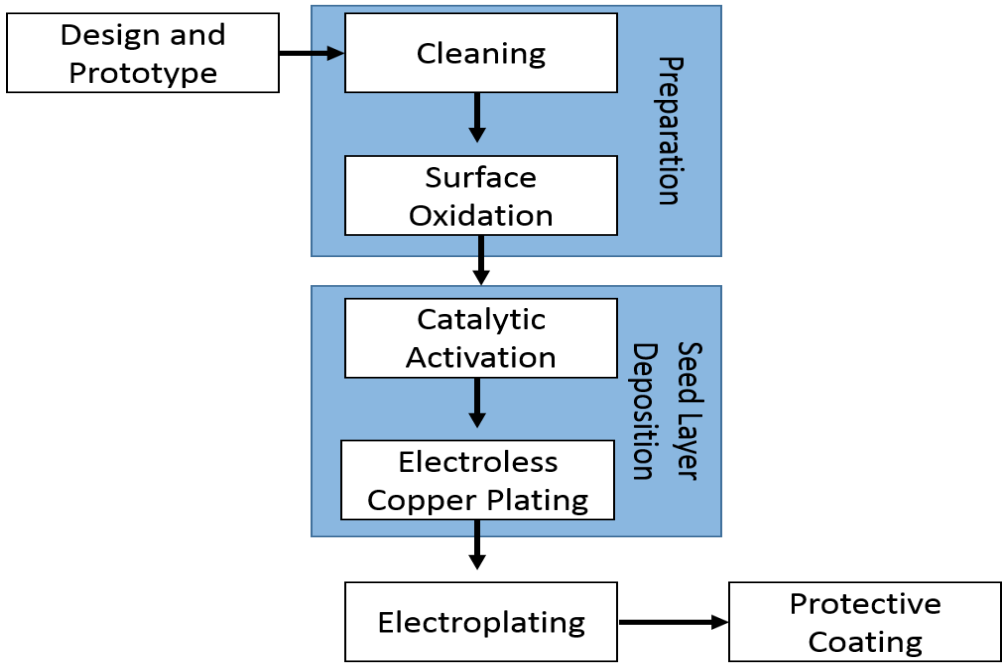

Figure 4.1 Overview of the proposed method

A rectangular waveguide is commonly used for transferring electromagnetic power from one port to another when the operating frequency is typically above 3GHz and where using coaxial cable could cause great loss. Rectangular waveguides must have conductive walls on each side, as shown in Figure 4.2 (a) where a denotes the dimension of the broad wall and b denotes the dimension of the short wall. Rectangular waveguides are typically air-filled to minimize dielectric loss; thus, the permittivity and permeability are essentially ϵ_0 *and* μ_0 , respectively. The electric and magnetic fields inside the waveguide is dictated by the source-free Maxwell's equation

$$\nabla \times \mathbf{E} = -j\omega\mu\mathbf{H}$$
$$\nabla \times \mathbf{H} = j\omega\epsilon\mathbf{E}$$
$$\nabla \cdot \mathbf{E} = 0$$
$$\nabla \cdot \mathbf{H} = 0 \tag{4.1}$$

where E and H are the electric field and magnetic field inside the waveguide, respectively. The solution to Maxwell's equation in a waveguide, i.e., the supported modes are categorized by the transverse and longitudinal components of the electric and magnetic fields. Transverse electric (TE) modes have no longitudinal electric field components, i.e., E_z=0. Transverse magnetic (TM) modes have no longitudinal magnetic field components, i.e., H_z=0. Similarly, transverse electric and magnetic (TEM) modes have no electric and magnetic field in the longitudinal direction, i.e., E_z=0 and H_z=0 . The dominant mode inside a rectangular waveguide is the TE_{10} mode. The solution of TE mode inside a rectangular waveguide takes the form

$$(\partial x^2 + \partial y^2)H_z + k_c^{\,2}H_z = 0$$
$$H_x = -\frac{j\beta}{k_c^{\,2}}\partial x H_z$$
$$H_y = -\frac{j\beta}{k_c^{\,2}}\partial y H_z$$
$$E_x = \eta_{TE}H_y$$
$$E_y = -\eta_{TE}H_x \tag{4.2}$$

where $\beta = \frac{2\pi}{\lambda_g}$ is the propagation wavenumber, $k_c^2 = \omega^2\epsilon\mu = \left(\frac{\omega}{c}\right)^2 - \beta^2$ is the cutoff wavenumber. The transverse impedance is denoted in Eq. 4.2 as $\eta_{TE} = \omega\mu/\beta$. Since we are

considering the TE_{10} mode, the solution should only be dependent on the x-direction along the broad wall, i.e. dy = 0 and satisfy the following equations

$$\begin{aligned} \P x^2 H_z(x) + k_c^{\,2} H_z(x) &= 0 \\ H_x &= -\frac{jb}{k_c^{\,2}} \P x H_z \\ H_y = 0,\ E_x &= 0 \\ E_y = -h_{TE} H_x &= -\frac{jb}{k_c^{\,2}} \end{aligned} \tag{4.3}$$

The general solution of the differential equation in Eq. 4.3 is thus a linear combination of $\cos k_c x$ *and* $\sin k_c x$. However, the solution must also satisfy the boundary condition at the x = 0 and x = a. Thus only the $\cos k_c x$ part of the solution is kept, i.e

$$H_z(x) = H_0 \cos k_c x \tag{4.4}$$

The electric field is thus

$$\begin{aligned} E_y(x) &= -h_{TE} \frac{jb}{k_c} H_0 \sin k_c x \\ &= E_0 \sin k_c x \end{aligned} \tag{4.5}$$

When applied the boundary condition at the walls, i.e. $x = 0$ *and* $x = a$, E_y must be 0, resulting in $k_c a = n\pi$, forcing the electric field at the wall is 0, as shown in Figure 4.2 (a).

A split-block design [4, 14-16] is used when waveguides have to be made by combining two pieces rather than a single tube; the question arises when deciding where to cut the waveguides. When combining two pieces of the waveguide into one piece, there is always unwanted discontinuity created on the conductive wall, which generates losses

and leakage. To minimize the loss and leakage due to the discontinuity, the cut should preferably avoid the walls where boundary conditions must be met. As it is shown in the previous calculations, E_y=0 must be enforced at the both ends of the broad wall for the TE_{10} to propagate; thus, it is preferable to split the two halves from the middle of the broad wall at x=a/2, i.e., the center E-Plane, as shown in Figure 4.2 (b).

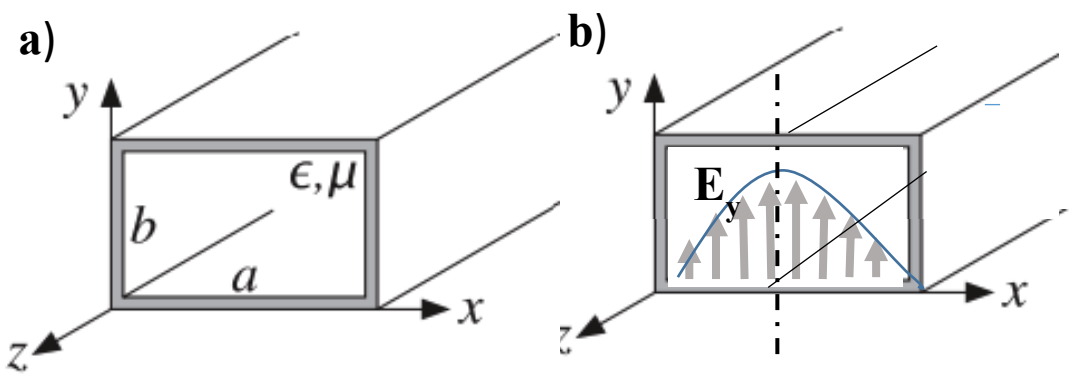

Figure 4.2 Electric field distribution inside a air-filled rectangular waveguide and its effect on selecting the plane for split-block design

(a) Diagram for an air-filled waveguide with notations specified for its broad and short wall (b) The electric field inside an air-filled waveguide.

The size of a waveguide determines its operating bandwidth because all waveguides are designed to ensure that only the lowest mode can propagate, i.e., the TE_{10} mode for rectangular waveguides, and not allow the next lowest mode to coexist in the waveguide. The next lowest mode inside a rectangular waveguide could be the TE_{01} or TE_{20} mode, depending on the size of the short wall b. Traditionally, b is

chosen to be smaller than a/2, i.e. $\boldsymbol{b} \leq \frac{\boldsymbol{a}}{\mathbf{2}}$, so that the next mode is TE_{20} instead of TE_{10} because the cutoff frequency of TE_{20} is higher than that of TE_{01}, given that the cutoff frequency for TE_{nm} mode is

$$f_{nm} = \sqrt{(\frac{np}{a})^2 + (\frac{mp}{b})^2} \quad . \tag{4.6}$$

The following table shows the parameters and dimensions chosen for conventional air-filled rectangular waveguides where a and b are in inches [85].

name	a	b	f_c	$f_{\min}$	$f_{\max}$	band
WR-90	0.90	0.40	6.56	8.20	12.50	X
WR-62	0.622	0.311	9.49	11.90	18.00	Ku
WR-42	0.42	0.17	14.05	17.60	26.70	K
WR-28	0.28	0.14	21.08	26.40	40.00	Ka
WR-15	0.148	0.074	39.87	49.80	75.80	V
WR-10	0.10	0.05	59.01	73.80	112.00	W

Figure 4.3 Conventional air-filled rectangular waveguide dimension and operating frequencies (GHz) [85]

It can be seen that as frequency increases and wavelength gets much shorter, the dimension for the waveguide become much smaller. For example, for a WR-10 waveguide that operates in the 75-110GHz range, the short wall has to be 0.05 inch (1.27 mm). The small dimension poses a big challenge for 3D printing technology and leads to the choice of using polymer jetting (PJ) 3D printing in this method. Although ABS wire-feed technology, such as fused deposition modeling (FDM), imposes a much lower cost, the resolution for FDM printers is incapable of high-frequency applications. Polymerization-

based printers, such as polymer jetting and stereolithography, become optimal choices because their resolution can reach 15-20 μm, depending on the model.

Following the abovementioned considerations, a 15 cm WR42 waveguide is designed and 3-D printed as shown in figure 4.4. The prototypes are 3-D printed using a Stratasys Object350 Connex PolyJet 3D printer with 16 μm layer resolution and 0.1 mm lateral resolution. The 3-D printer has an accuracy of 20-85 μm for features below 50 mm, and up to 0.2 mm for features larger than 50 mm, as illustrated in figure 4.4a). The waveguide is made of split-block designs cut from the center E-plane and combined together using bolts that are inserted into the holes along the substrates to minimize loss due to discontinuity and misalignment, as shown in Fig. 4.4b). Although the split-block waveguides have slightly inferior transmission performance than machined waveguide without the crack, the method described here is valuable for manufacturing complicated components and systems, since accessing the interior of a convoluted waveguide becomes progressively more difficult as the number of bends in the waveguide increases.

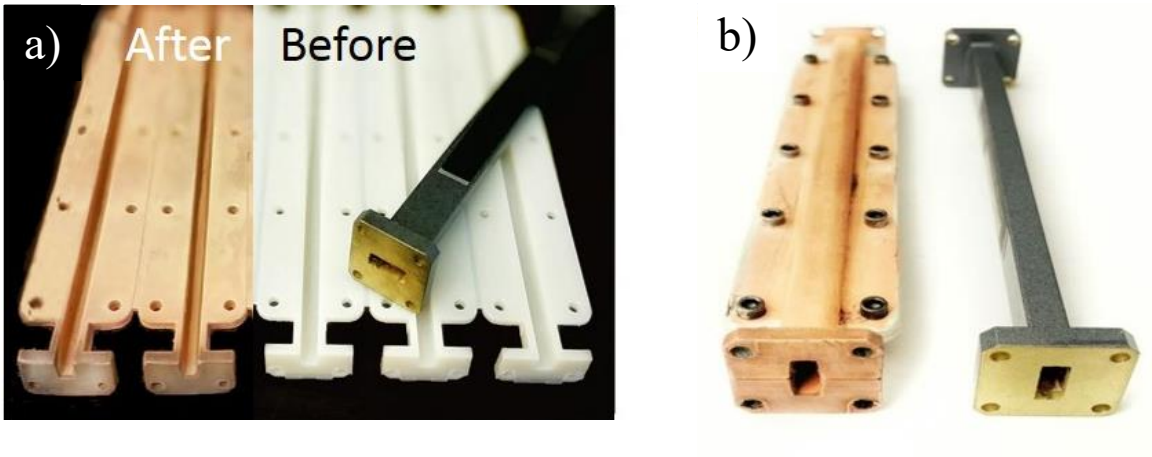

Figure 4.4 Copper desposition on the surface of dielectric 3-D printed waveguide sections

(a) 3-D printed WR42 waveguide split-blocks with standard rectangular flange, before and after metallization; (b) 3-D printed WR42 rectangular waveguide assembly after metallization, with its commercial counterpart

The metallization method proposed in this chapter is based on traditional electroless copper and electroplating procedures, with modifications to adapt to manufacturing microwave devices in an academic lab environment. To prepare the part for metallization, the support material must be removed and the parts must be cleaned thoroughly with a strong degreaser, such as trisodium phosphate. Any amount of residual grease on the surface will prevent the part from successful metal plating. After the part is cleaned, the next step in metallization is etching the surface with a strong oxidizer [82]. This step is necessary because the 3D printed plastic material needs to be made hydrophilic, so that the coating adheres to the plastic surface. A strong oxidizer, such as hydrogen peroxide will oxidize the part's surface and produce microscopic pores

that function as binding sites for the catalytic material. The part must be rinsed with deionized water following each step in the procedure.

The next step, electroless plating, is a popular technique for plating-on-plastic (PoP) that utilizes an oxidation-reduction chemical reaction rather than electrodeposition. The PoP technology was first developed in the 1960's to make automobile parts [82]; it was then applied to manufacturing shielding devices made of ABS plastics [86]. Asao et. al. demonstrated using PoP to manufacture millimeter waveguides and filters with injection-molded plastic [46, 47]. Plating on plastic relies on electroless plating, which is essentially a redox reaction where metallic ions are deposited onto the catalytic surface [87]. Copper is one of the popular materials used for electroless deposition and widely used in fabricating epoxy-based substrates for microelectronic devices, such as printed circuit boards (PCBs) [88].

The plastic surface needs to be catalytically activated before electroless deposition. However, traditional electroless copper plating requires palladium as catalyst [87], which imposes a high cost on manufacturing waveguides and antennas in a lab environment. Instead, the procedures choose to use silver (Ag), a cheaper and more accessible alternative [88]. Colloidal silver is deposited on the part through the repeated submersion of the part in tin(II) chloride and silver nitrate solutions. The reaction is described by the following equation:

$$Sn^{2+} + 2Cl^{-} + 2Ag^{+} + 2NO_3^{-} \rightarrow Sn^{4+} + 2Ag^{0} + 2Cl^{-} + 2NO_3^{-} \tag{4.7}$$

The colloidal silver deposited on the part surface appears to be black, as shown in Figure 4.5 (b). This is because colloidal silver contains submicroscopic nanoparticles of silver that are much smaller than optical wavelengths, thus absorbing light instead of reflecting it. For the same reason, the conductivity of a colloidal silver deposited surface is much less than that which underwent continuous silver deposition.

Electroless copper deposition requires no power supply to drive the deposition reaction, which is described by the following equation:

$$Cu^{2+} + 2HCHO + 4OH^{-} \xrightarrow{CATALYST} Cu + 2HCOO^{-} + 2H_2O + H_2 \tag{4.8}$$

Formaldehyde (HCHO) is used in this reaction as the reducing agent. The reaction relies on the surface to be catalytically activated. The detailed principle behind electroless deposition theory is provided in [87]. According to the mixed potential theory [87], the overall reaction can be decomposed into a separate reduction partial reaction,

$$Cu^{2+} + 2e^{-} \xrightarrow{catalyst} Cu \tag{4.9}$$

and a partial oxidation reaction,

$$HCHO + 2OH^{-} \xrightarrow{catalyst} HCOO^{-} + H_2O + \frac{1}{2}H_2O + e \tag{4.10}$$

The two reactions happen at the same electrode; namely, the metal-solution interface, the interface between a metal and an electrolyte solution. These reactions together create a steady state with a potential called the steady-state mixed potential. Figure 4.5 shows the measured I-V graph of the two separated reactions, and the

equilibrium condition [87]. As shown in the figure, the current density for equilibrium and the potential vs. standard electrode are at E=-0.65V. Thus, the rate of deposition can be calculated using Faraday's law using equation

$$w = i' \ 1.18 mgh^{-1}cm^{-2} = 2.2 mgh^{-1}cm^{-2} \tag{4.11}$$

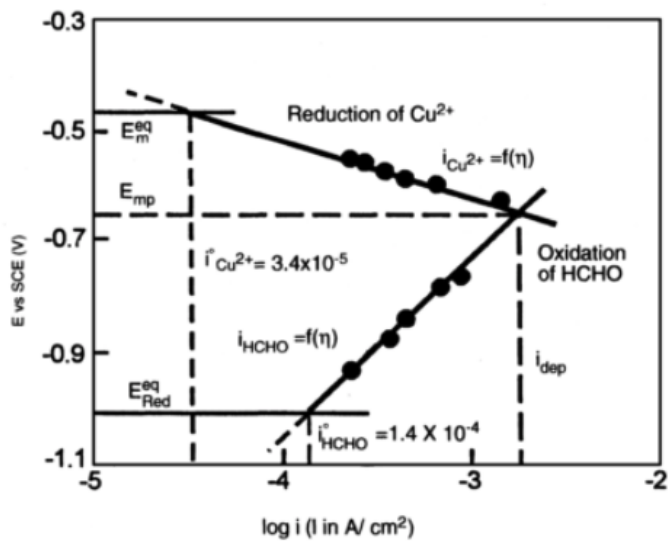

Figure 4.5 Evans diagram for reduction of Cu2+ ions and for oxidation of reducing agent formaldehyde [87]

The concentrations of reactants and the temperature are two important factors that control the reaction rate and must be carefully controlled. Formaldehyde can only act as a reducing agent when in an alkaline environment, i.e., pH 12 or above. However, copper ions form copper hydroxide and tend to precipitate out of the solution. A chelator, such as EDTA or triethanolamine(TEA) is to be used to prevent copper hydroxide precipitation. The concentrations of reactants and temperature are two important factors that control the rate of reaction. The electroless plating reaction heats up the solution and is also an

auto-catalytic reaction; i.e., deposited copper catalyzes the oxidation of formaldehyde and the reduction of copper. The reaction condition and reactant concentration thus have to be carefully controlled. The electroless copper plating solution contains 5g/L copper sulfate, 10g/L EDTA, 5g/L sodium hydroxide, and 20mL/L 4% formaldehyde as the reactant, and 100mL/L triethanolamine as the chelator and pH buffer. The temperature should be maintained at 50-60 C, and pH is maintained between 12 and 12.5. The detailed method and procedure for electroless copper deposition are described in [87, 88]. Successful electroless plating is able to deposit copper of a few microns, depending on the surface area, which is enough to act as a seed layer for electroplating.

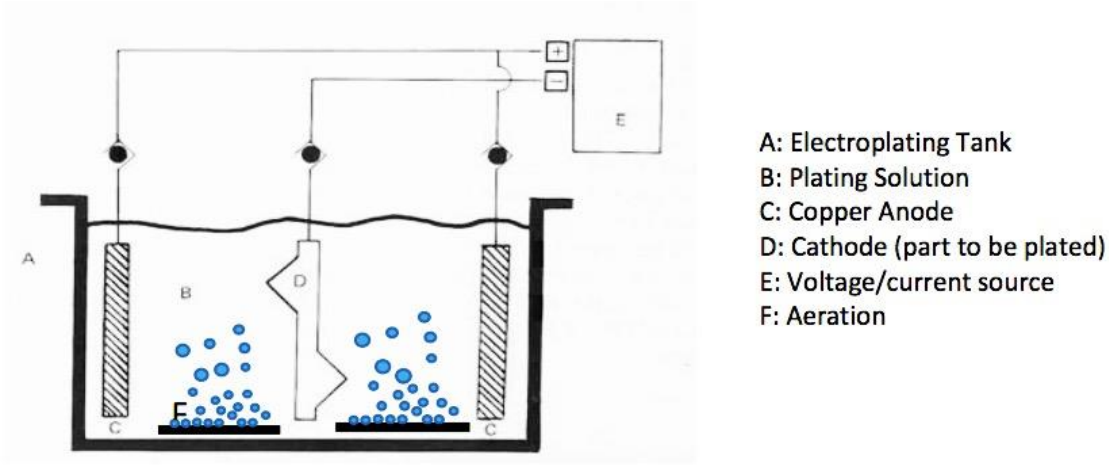

Figure 4.6 Electroplating mechanism used for copper deposition

Following the electroless deposition, the part is plated using electrolytic deposition to enhance surface copper deposition. Common techniques employ acidic electroplating using sulfuric acid or fluoboric acid [89], but a weaker acid that dissolves copper, such as acetic acid, can be used when less hazardous chemicals are preferred. If a

weaker acid is used, however, the plating solution's throwing power is sacrificed, and a longer deposition time is required to sufficiently plate deep features. Electroplating microwave devices such as waveguides require the inner surface of the channel to have a bright finish, indicating a smooth surface with low loss. One key factor in achieving smooth and bright copper deposition is introducing additives into the plating solution. To achieve this goal, we adopted the additive recipe introduced by IBM in the damascene process, which has been widely used in on-chip metallization [90]. In the common damascene process, the copper sulfate-based electroplating bath utilizes small amounts of chloride ions and polyethers such as polyethylene glycol (PEG) as a suppressor, a sulfur-based organic compound such as 3-mercapto-1-propanesulfonic acid as a brightener, and an aromatic nitrogen based polymer such as Janus Green B as leveling agent to produce mirror-flat surfaces [91]. Additives include 0.132g/L sodium chloride, 0.5g PEG (polyethylene glycol), 0.06g sodium MPSA (3-mercapto 1-propanesulfonate), 0.06g Janus Green B [92]. Another key factor is the agitation of the plating bath. Good agitation ensures uniform copper deposition and reduces the current density needed for electroplating.

The finished part is then immediately rinsed and transferred to a benzotriazole bath to prevent future oxidation. Oxidation on the surface lowers the conductivity and even rusting, which can be inhibited with a thin layer of benzotriazole coating.

Using the procedure described above, a K-band pyramidal horn with a standard

WR42 flange is also designed, with a 105 mm x 79 mm aperture and 19 cm in length. The pyramidal horn is also split from the E-plane, as shown in Figure 4.8. The designed prototypes are replicas of commercially available products for directly comparing the results.

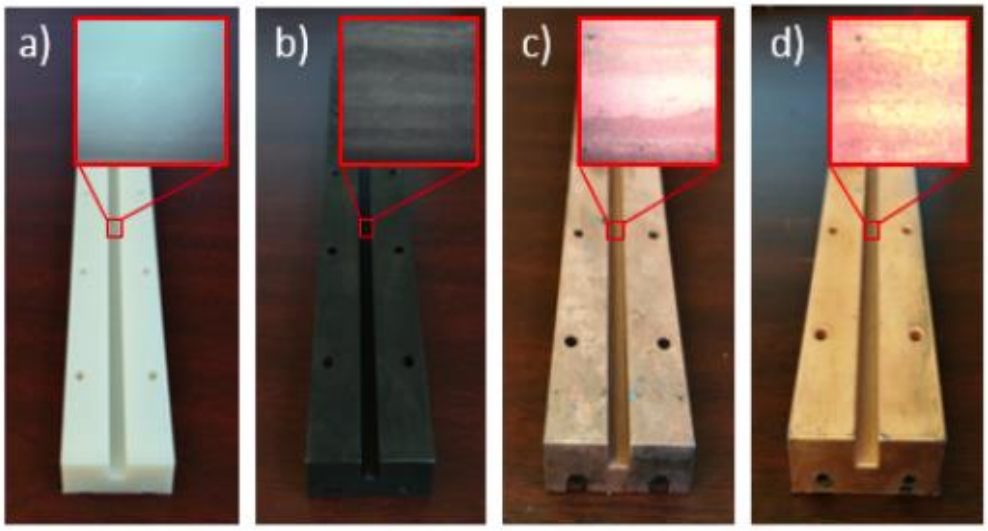

Figure 4.7 The half WR42 waveguide block during the plating process with the insets show the microscopic image of the part surface.

(a) after cleaning support material and grease. (b) with silver deposited as a catalytic agent for electroless copper plating. (c) after

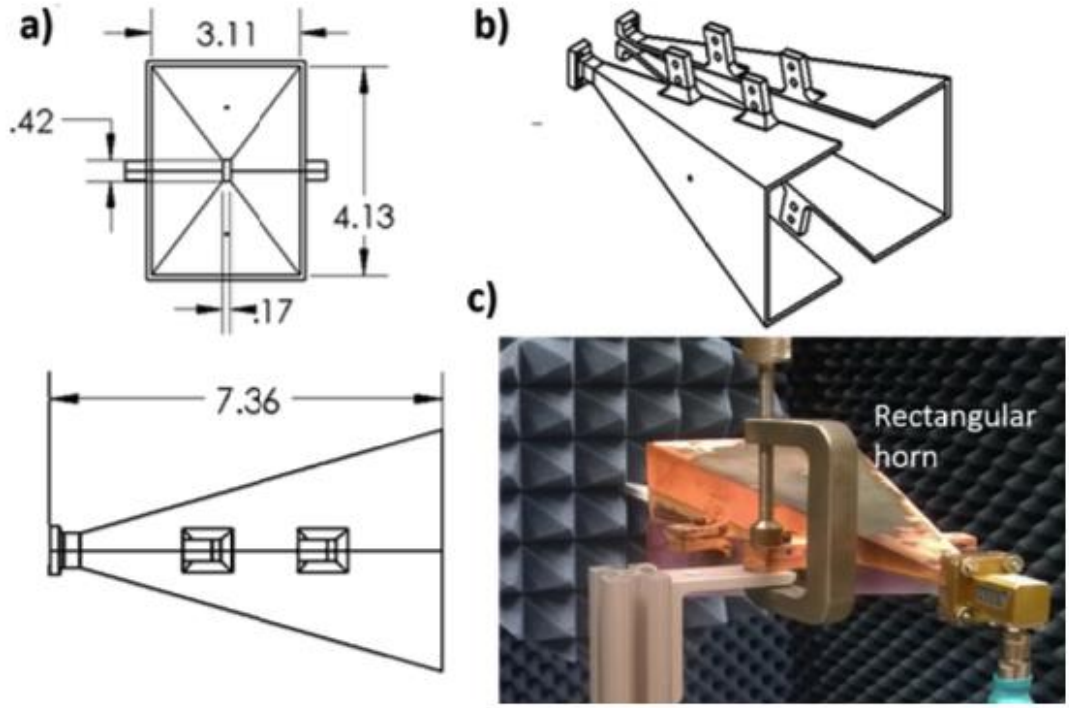

Figure 4.8 K-band rectangular horn drawings

(a)-(b) Schematic drawing of a K-band rectangular horn c) the manufactured horn antenna under test

4.3 Results and performance

The metallization results and performance of the pyramidal horn and the K-band waveguide is demonstrated by comparing the performance to their commercial counterparts. Figure 4.9 (a)-(c) shows the surface scan of a WR42 waveguide under a Zygo optical profilometer. A 250 μm by 400 μm area inside the waveguide channel has been scanned and shown in the figure. The noticeable particles on the surface may have

attached to the surface during the electroplating process, which introduces a 10 μm artifact on the surface as the worst case scenario. The surface roughness is 2μm along the z-direction and 1μm along the x-direction. The average smoothness, Ra, defined as the arithmetic mean deviation, i.e., the average deviation of all points from the measurement is calculated $R_a = \frac{1}{A}\iint |y(x,z)|dxdz$, where A is the area. The measured smoothness is 0.479 μm. Comparing to a 0.93 μm roughness of the rectangular waveguide made with SLA 3D printers metalized by commercial electroless plating and reported by [53], the surface roughness with our method is almost twice as good.

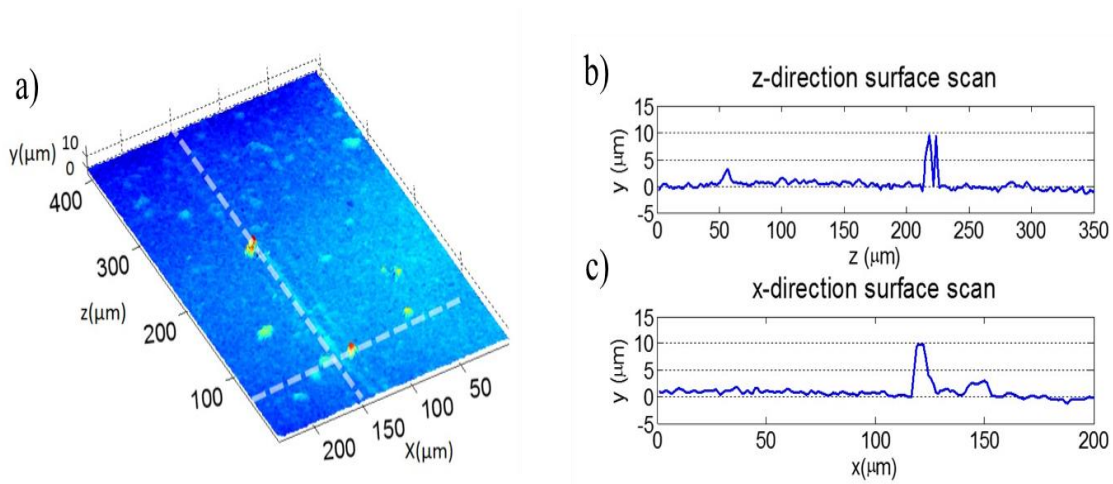

Figure 4.9 Measurement of surface smoothness after copper deposition

(a) 3D scan of surface area inside the waveguide channel. (b) worst case z-direction surface profile, and (c) worst case x-direction surface profile

To evaluate the performance and the feasibility of replacing traditional waveguide manufacturing with 3D printing, the return loss $|S11|^2$, and the transmission loss $|S21|^2$ of the 3D printed waveguide is measured with a network analyzer and compared with an identical commercial waveguide. The results shown in Fig. 4.10 (a)-(b) indicate almost

identical performance for the 3D printed and commercial waveguides across all frequencies in the K-band. The 3D printed waveguide has an average of 0.4 dB loss in transmitted power. To further characterize the loss performance, we calculated the dissipative loss per wavelength of the two waveguides, which can be calculated as $\frac{\lambda}{L}|S_{11}|^2/(1-|S_{11}|^2)$ where λ is the L wavelength, and L is the waveguide length [93].The result of the dissipative loss calculation is shown in Fig. 4.10 (c); it is almost identical between the 3D printed waveguide and the commercial waveguide.

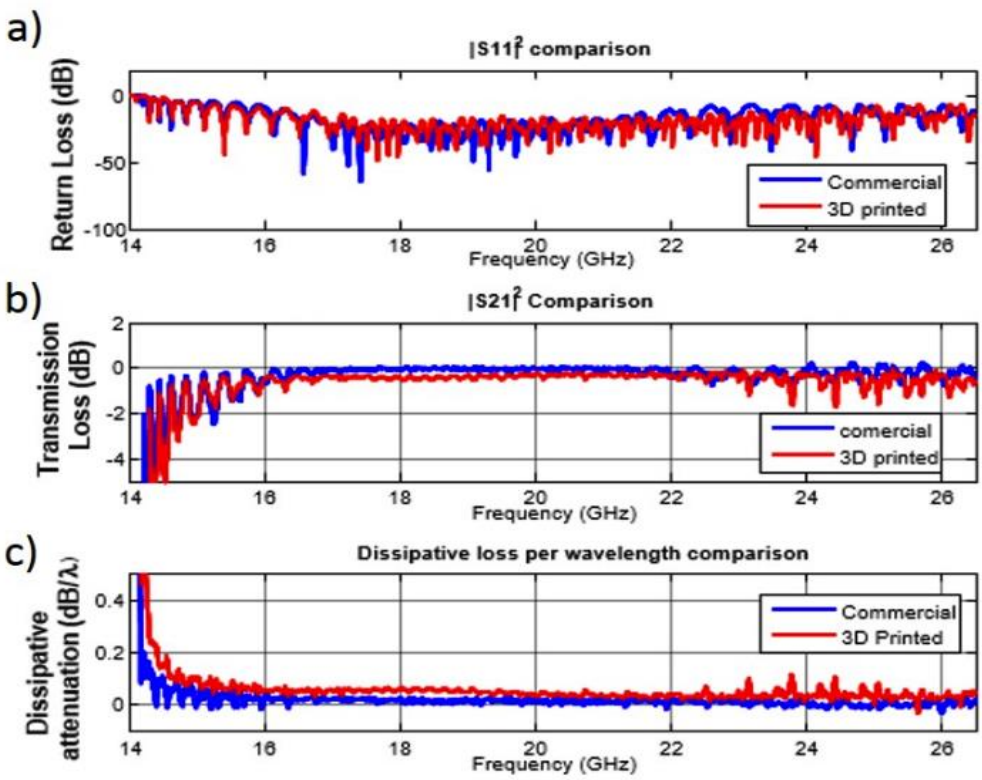

Figure 4.10 Performance of the 3D printed WR42 rectangular waveguide comparing with an identical commercial waveguide.

(a) S11 parameter comparison. (b) S21 parameter comparison. （c) calculated dissipative attenuation per wavelength comparison.

To test the performance of the metalized rectangular horn antenna, the radiation pattern of the antenna is measured with an NSI near-field scanner and compared with an identical commercial counterpart with 21Db gain. The comparison of the radiation pattern is made at different frequencies across the K-band and is shown in Figure 4.11. It can be seen that the 3D-printed pyramidal horn made with the proposed rapid prototyping method has an almost identical radiation pattern and gain performance to its commercial antenna across the K band.

The performance of the 3D-printed components can be affected by the heating during chemical procedures, resulting in warped parts and some misalignment along the crack. These defects can be minimized or avoided by careful handling during the chemical treatment and precise assembling with the alignment holes.

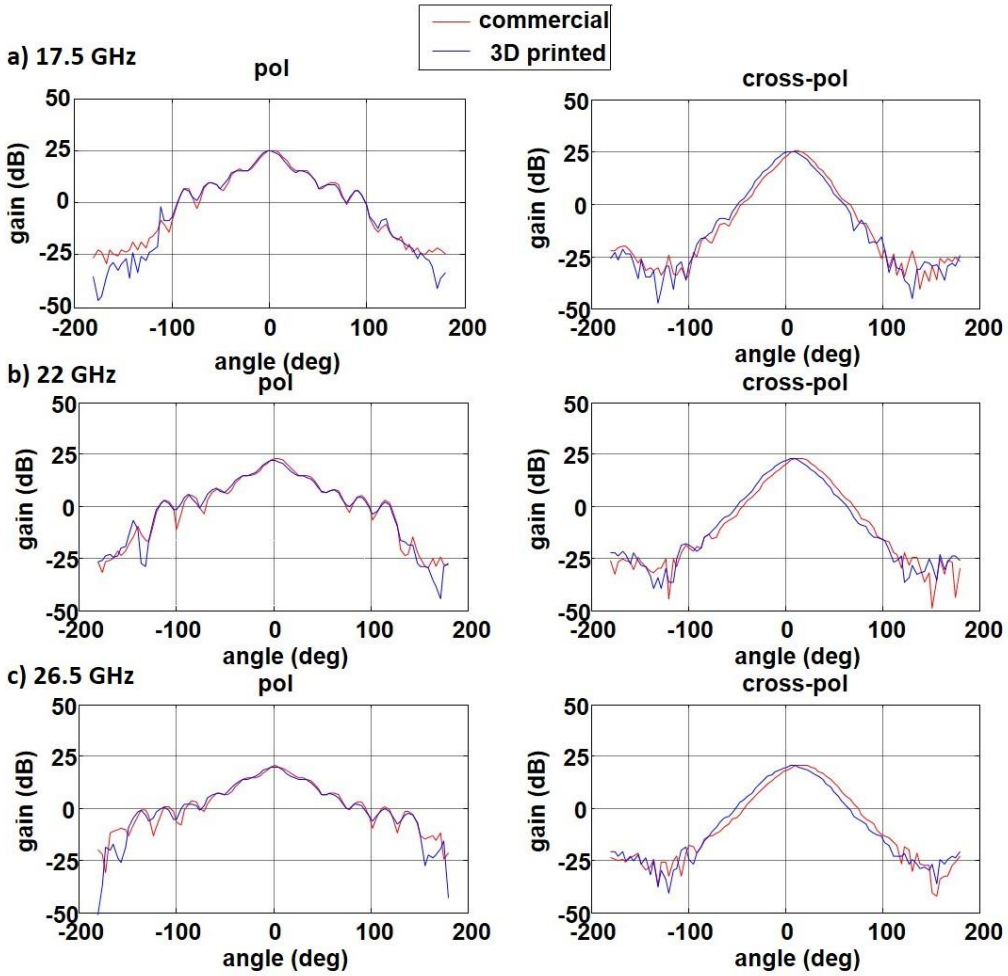

Figure 4.11 The radiation pattern of the 3D-printed WR42 pyramidal horn compared with a commercial horn under different polarizations at different frequencies

4.4 Towards integrated millimeter wave and terahertz system

The ultimate goal of developing a rapid prototyping method for microwave components is to acquire the ability to manufacture microwave systems in unity. This ability is especially beneficial for millimeter wave and terahertz frequency systems because these high-frequency systems are traditionally complicated in manufacture.

The 3-D printing of millimeter wave and terahertz systems offers a fast, cheap, lightweight, compact and yet high-quality solution to prototyping and manufacturing THz systems. The components can be made with a high-resolution 3-D printer with plastic and metallized with copper only on the surface that matters to terahertz waves. Thus, the cost and weight of such components can be largely reduced while maintaining high quality. Moreover, 3-D printing enables the optimization of the size and components, so the system can be made compact without increasing the complexity of the manufacturing process.

Several efforts have been made to integrate millimeter wave and terahertz systems with 3-D printing technologies. 3-D printing has already been used for manufacturing structured electronics [73]. Xin et al. have demonstrated a multilayer RF microstrip made by 3-D printing and metalized with ultrasonic wire embedding [94], which opens up the possibilities of 3-D printing integrated structured electronics in the RF domain. A 3D printed plastic lens at 60GHz [71] has also been demonstrated to integrate with a millimeter-wave, high density interconnects (HDI) antenna package.

The advantage of 3D printing applied to THz and MMW imaging systems comes twofold; system integration and low loss at high frequency. The ability to integrate MMW and a THz source have already been shown in [94]. Circuitry can be printed and metalized with mounting structures to hold silicon radar chips. Based on the successful demonstration of 3D printed MMW components, such as waveguide, antenna, with the

advancement of 3D printing materials in physical sturdiness and cost efficiency, it is foreseeable that an integrated radar system can be made.

5. 3-D printed spiral leaky-wave frequency diverse antenna for computational millimeter wave imaging

High-resolution radar imaging requires a wide bandwidth and a large aperture, which motivates imaging using higher frequencies, such as millimeter wave frequencies and synthetic aperture methods. A large aperture is often synthesized by using a large array of single apertures or by raster scanning a single aperture. The former method is much more expensive, especially for higher frequencies whereas the latter is slow and often noisy. In the previous chapters, methods of improving radar imaging using computational methods are proposed. A method of using a sparse array instead of a full focal plane array is used to estimate the surface profile and reflectivity is discussed in Chapter 2. An adaptive sensing algorithm based on the Bayesian compressive sensing that reduces the amount of mechanical scanning is introduced in Chapter 3. These methods utilize different computational methods to improve the efficiency of imaging using simple antenna transceivers. As it is mentioned in Chapter 1, more complicated antennas, such as various beam-steering antennas and frequency-diverse antennas are able to improve the efficiency of radar imaging even further when combined with computational imaging algorithms. Facilitated by the method proposed in Chapter 4 for rapid prototyping custom designed antennas, a method that combines novel antenna design with computational

imaging methods is discussed in this chapter as a further improvement for millimeter-wave radar imaging.

5.1 Introduction

Imaging systems capture information from the object dimension and transform it into data that fits into the information domain. For example, a conventional camera captures a scene of the objects in front of the viewer, a 3D scene of the real world, and transforms the inherent information of the objects, i.e., how light scatters off the surface of these objects, which reveals the properties of these objects into signals that are perceivable by the 2D camera sensor. During this process, the information in the object dimension, i.e., x, y, z intensity and wavelengths, is confined in the information dimension, i.e., only x and y, and intensity is recorded. Computational imaging is a generalized terminology for methods that utilizes computational algorithms, such as compressive sensing and light-field imaging to aid the design of imaging systems in a way that the imaging systems are no longer confined by the information dimension. Compressive sensing is one of the most popular techniques used for acquiring information beyond the number of pixels since the goal of compressive sensing is to reconstruct a signal using much fewer samples, as compared to the Nyquist sampling theorem. Compressive sensing under visible light imaging has been able to extend traditional 2D imaging into time-domain super-resolution imaging [40], 2D hyperspectral imaging [39], polarization

imaging [41], etc. The key is to code the extra dimension signal using a coded aperture to multiplex the signal [21].

In radar imaging, the information dimension is limited to one dimension, i.e., the range domain or the frequency domain whereas the object dimension is at least three-dimensional; thus, compressive sensing becomes a good solution to overcome the limit posed by signal acquisition. Various techniques have been explored to apply compressive sensing in the radar imaging scheme [95-98]. Similar to the coded aperture imaging techniques, imaging in microwave frequencies in a compressive way also require ways to multiplex the signal. To multiplex a 2D scene, the radiating aperture has to be frequency-diverse, i.e., radiating a different 2D pattern (the measurement mode) at different frequencies. Several demonstrations have been made to image with various types of frequency-diverse antennas. One way to achieve frequency diversity is to incorporate resonant structures in the aperture, such as metamaterial elements [7]. (Hunt et. al) [6] has demonstrated imaging with a planar panel populated with metamaterial apertures with distinct resonant frequencies. Another approach, by (Xin et. al) [22] uses a reconfigurable array to modulate the array pattern.

The evaluation of a frequency-diverse antenna is usually done by assessing how many measurement modes, i.e., how many distinct radiation patterns an antenna is able to generate.One important factor to increase the number of measurement modes is to increase the quality factor, i.e., the Q-factor. The Q-factor is an indication how many

distinct radiation patterns can be packed into the full bandwidth. The number of modes within the bandwidth is decided by how much the frequency has to be changed to produce a unique radiation pattern [99]. For a resonating element, the Q-factor determines how wide are the peaks at the center frequency f_0 with the 3dB bandwidth calculated as f_0/Q. For a high Q antenna, the peaks are narrow thus the frequency does not have to change much to produce another radiation pattern, and vice versa. Given a bandwidth B, the number of unique measurement mode can be estimated by QB/f_0. Since the operating frequency bandwidth is fixed, a high Q-factor is needed to have a large number of distinct measurement modes.

The Q-factor for any RF resonator is defined in the same way of any RLC network, i.e.,

$$Q = 2p f_0 \frac{energy\ stored}{energy\ dissipated} \tag{5.1}$$

According to [99], the Q-factor can be increased by either increasing the stored energy or by decreasing the energy dissipated. The energy stored can be increased by simply increasing the volume of the antenna. However, as mentioned in the earlier chapter, the energy lost in the form of Ohmic losses are associated with conductive walls from the cavity walls and dielectric filling, if any. The Ohmic loss due to resistivity on the wall can be mitigated by decreasing the surface area or increasing the conductivity of the wall material. The former method is used in the higher terahertz frequency applications where electromagnetic bandgap structures [30] made of dielectric materials can be used

to guide waves inside waveguides. For lower frequencies, (such as the millimeter-wave frequency) antennas, the scaling of frequency favors conductive over dielectric materials [99]. As discussed in Chapter 4, energy losses due to dielectric filling can be mitigated by introducing air-filled antennas; thus, air-filled cavities are favorable, as compared to dielectric cavities, even though dielectric cavities can be made with low-cost using various circuit fabrication techniques. Another source of energy loss is the coupling of the antenna from the rest of its circuit. Impedance mismatching and imperfect contacts between the two may cause reflection and leakage before the waves are coupled into the structure. It is thus, necessary to maximize the volume of an air-filled structure. In the meanwhile, minimize the total surface area and increase wall conductivity and impedance-matching to have a high-Q antenna. It has been shown in [99, 100] such air-filled resonant cavity with radiating apertures with increased Q-factor can effectively increase the imaging ability.

In this chapter, a novel type of frequency diverse antenna based on a slotted leaky waveguide is presented. Leaky waveguides have been widely used for their beam steering ability [101], as introduced in Chapter 1. A leaky waveguide with diversified radiation patterns in a spiral shape has been designed as shown in Figure 5.1 (a). The spiral leaky waveguide can be seen as an ensemble of horizontally and vertically oriented leaky waveguide sections. The radiation pattern can thus be seen as a linear combination of the radiation patterns of all leaky waveguide sections. The overall radiation pattern thus has

variations in the two-dimensional space when changing its operating frequency, enabling it to encode the measurement of the scene.

Figure 5.1 Images of the 3D-printed spiral leaky wave antenna panel

(a)-(b) the front and back half of the frequency diverse antenna (c) the leaky wave frequency diverse antenna assembly with cone-shaped elliptical holes as radiating apertures

5.2 Design and prototyping

The leaky-wave frequency diverse antenna is based on a cavity backed slot waveguide. Traditional slotted antennas are widely used as steering beam radar for navigation applications [101]. They are made from shorted waveguides with open slots on the side walls. A voltage applied across a slot induces an E-field within the slot and a circulating current around the slot. This results in the slot radiating like a dipole antenna, according to Babinet's principle [85]. This configuration can be treated as a waveguide acting as the transmission line and powering all the dipoles along the line. The shape, position, and orientation all determine how the slots radiate because of the distribution of

wall current, E-field, and H-field inside the waveguide. As discussed in the earlier chapter, inside a rectangular waveguide, the dominant TE_{10} mode has a propagating E-field and and H-field, as described in

$$H_x = \frac{-E_0}{2pfm}\sqrt{k^2 - (\frac{p}{a})^2}\sin(\frac{px}{a})e^{-j\sqrt{k^2-(p/2)^2}z}$$
$$E_y = E_0\sin(\frac{px}{a})e^{-j\sqrt{k^2-(p/2)^2}z}$$
$$H_z = \frac{jE_0}{2pfm}\cos(\frac{px}{a})e^{-j\sqrt{k^2-(p/2)^2}z} \tag{5.2}$$

where a is the broad wall of the waveguide and k is the wavenumber. The tangential magnetic field on the top wall of the waveguide generates a current on the surface, which can be determined by $\boldsymbol{J} = \hat{\boldsymbol{n}} \times \boldsymbol{H}$, which can be calculated as

$$J_x = -\frac{jE_0}{2pfm}\cos(\frac{px}{a})e^{-j\sqrt{k^2-(p/2)^2}z}$$
$$J_z = -\frac{E_0}{2pfm}\sqrt{k^2 - (\frac{p}{a})^2}\sin(\frac{px}{a})e^{-j\sqrt{k^2-(p/2)^2}z} \tag{5.3}$$

The slots on traditional leaky-wave antennas are thin rectangular slots with a size of 0.1λ by 0.5λ, as shown in figure 5.2. According to Maxwell's equations, the slots on the wall can only radiate when the excited current is disturbed and has to detour around the slots. Consider slot #1 centered on the broad wall of the waveguide shown in figure 5.2, where the slot is a narrow rectangle oriented along the z-direction. The z-component of the excited wall current will not be disturbed as the opening perpendicular to z-direction is small enough, i.e. 0.1λ. The narrow slit design forces the radiation to be mostly in one polarization, thus resulting in minimum cross-polarization (x-pol). The x-component of

the wall current reaches 0 at x=a/2; thus, when the slot is located in the center of the wall, the current is not disturbed. As a result, slot #1 is not a good choice for placing the leaky holes on a rectangular waveguide. By introducing an offset from the center, slot #2 is a popular configuration for steering leaky waves.

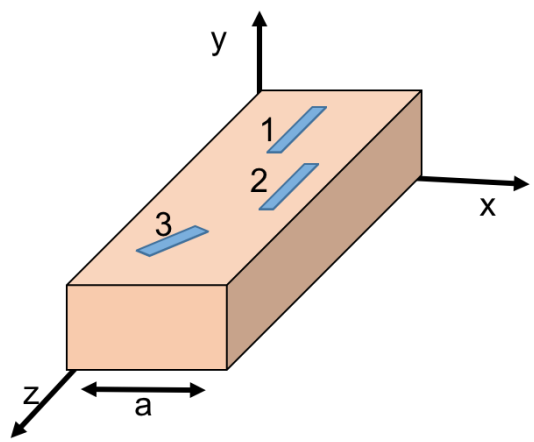

Figure 5.2 Different orientations of slots on an air-filled rectangular waveguide

In this work, the frequency diversity antenna is not designed to work only for single polarization where the cross-polarization is unwanted. As long as the radiation pattern for the frequency diverse antenna is accurately characterized at each frequency sample and measured at both polarizations, it is sufficient to reconstruct images with a frequency diverse antenna system. Thus the slot #3 is also a probable candidate where the radiation power is proportional to the rotational angle, and both x and z components of the wall current will contribute to the radiation. In addition, the shape of the radiating holes thus does not have to be "narrow slots" and much are more flexible when designing the panel.

The radiating power of a circular hole on a leaky waveguide can be modeled as

$$P_{rad} = 2\pi\nu(4\alpha^3 c^3 / 3\nu^3)(2\mu_0 |H| + \epsilon |E|^2) \tag{5.4}$$

where c is the speed of light, f is the frequency, and α is the diameter of the circular hole [11]. Thus the radiating power grows in a cubic fashion with respect to the diameter-to-frequency ratio, i.e., a fixed size hole radiates more at lower frequencies but less at higher frequencies. To make the antenna radiate more equally at each frequency, the holes are made with random sizes to make lower frequencies radiate more. Although the holes implemented here are not necessarily circular holes, the above equation provides a qualitative insight on how the parameters of the opening on the side wall affect the radiation power.

The radiating holes are designed to be ellipses of random sizes placed along the center of the broad walls. Thus, a balance has to be struck by randomizing the sizes of the holes. The elliptical holes are also oriented in random directions to equalize the radiation efficiency at different frequencies. Figure 5.3 shows a set of computer simulations of four K-band leaky waveguide sections with identical circular holes, random sized holes, identical ellipses, and ellipses with random sizes and orientations. The |S21| parameters are calculated to estimate the amount of radiation through the series of holes. The comparisons in figure 5.3 demonstrate the effect of randomizing the size and orientation of radiation holes. By comparing figures 5.3 (a) and 5.3(b), it can be seen that by randomizing the size of radiating holes, the radiation at lower frequencies can be

increased to the same level as higher frequencies. By comparing figures 5.3(c) and 5.3(d), it can be seen that by randomizing the radiating ellipses, the leaky waveguide changes from radiating selectively at some frequencies to radiating equally at all frequencies in K-band. Another factor to consider is the spacing between the holes, which decides where the main beam of a steering beam leaky waveguide points towards at the center frequency. The beam direction follows the equation

$$\sin f = \left(\sqrt{(k_0^2 - \left(\frac{p}{2}\right)^2)} - \frac{2p}{p} \right) / k_0 \tag{5.5}$$

where ϕ is the main beam direction at center frequency, β is the wave number of the center frequency, and p is the period of the spacing between holes, assuming the spacing is identical. Although the radiation pattern we desired is a random one, it is still desirable to align the "main beam" at center frequency to the boresight direction in order to direct the radiation power toward the imaging scene because the spiral waveguide is essentially an ensemble of short, straight, leaky waveguide sections. Therefore, the spacing is calculated according to equation (5.5) as 1.7cm. Figure 5.4 shows the result of optimizing the periodic spacing between leaky holes on a K-band, air-filled waveguide. The radiation pattern is shown at different frequencies across the K-band, i.e., 18GHz (a), 22.25 GHz center frequency (b), and 26.5 GHz (c). The results in radial plots are shown in the bottom halves of Figure 5.5. It can be seen that the main beam at the center frequency is directed at 90 degrees, i.e., the boresight.

Following all the above-mentioned design considerations, the leaky waveguide-based frequency diverse antenna panel is designed for the K-band featuring a standard WR-42 channel wound up in an 18cm. x 18cm. square panel with 59 radiating holes along the broad wall of the waveguide. The antenna panel is 3D printed with a high-resolution Connex 360 PolyJet 3D printer, and with an axial resolution up to 16 microns. The 3D printed panels are then electroplated with pure copper using the method described in Chapter 4. This enables the plastic parts to have a conductive surface over the skin depth to guide the wave inside the channel. The 3-D-printed leaky waveguide is made in a split-block fashion in order to have the inside of the waveguide electroplated, as seen in figure 5.1 (a)-(b).

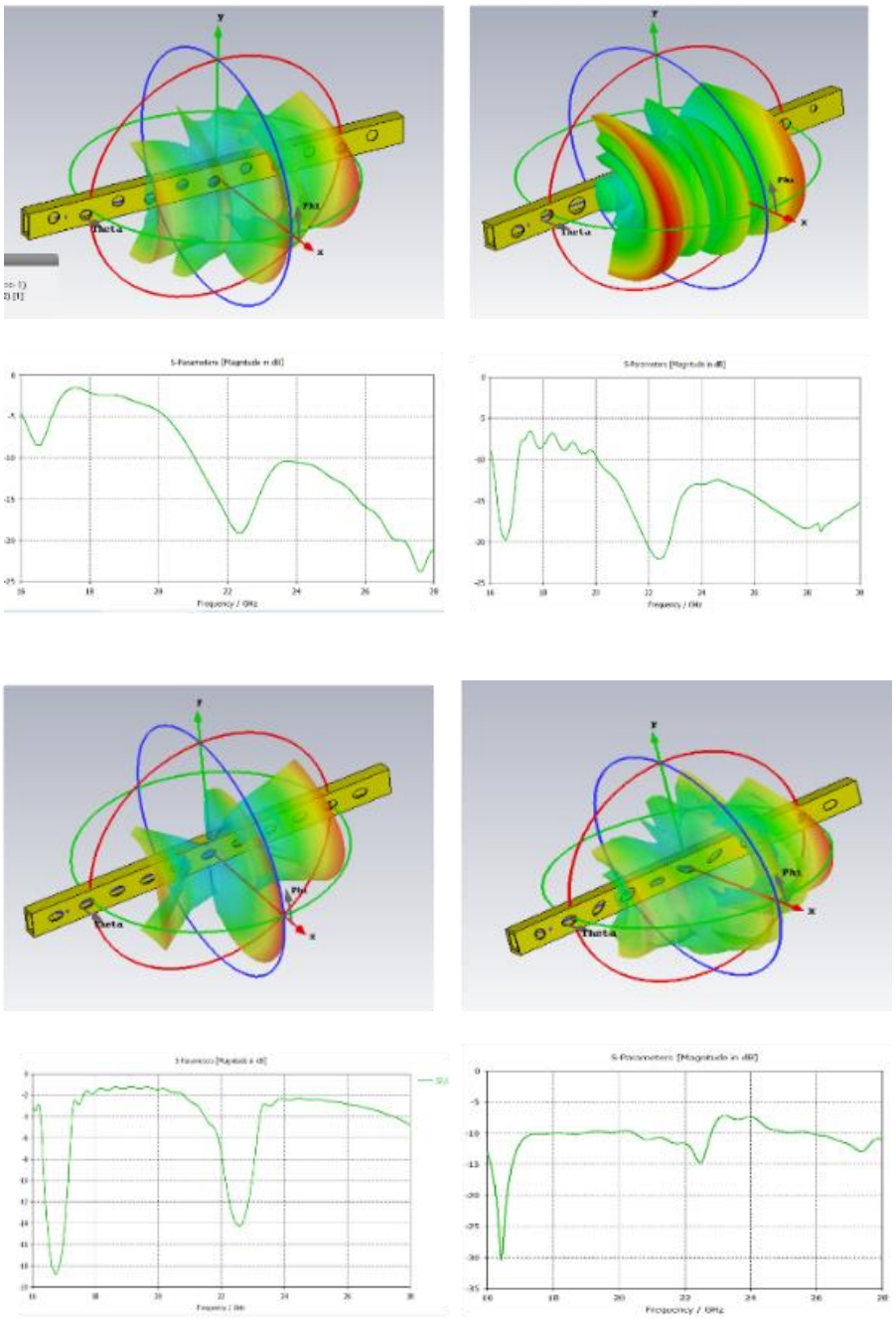

Figure 5.3 Simulation showing different frequency response corresponding to different slot designs

（a）Simulation of an air-filled rectangular waveguide with identical off-centered circular holes （b）off-centered holes with different sizes （c） identical centered elliptical holes (d) randomly oriented centered elliptical holes

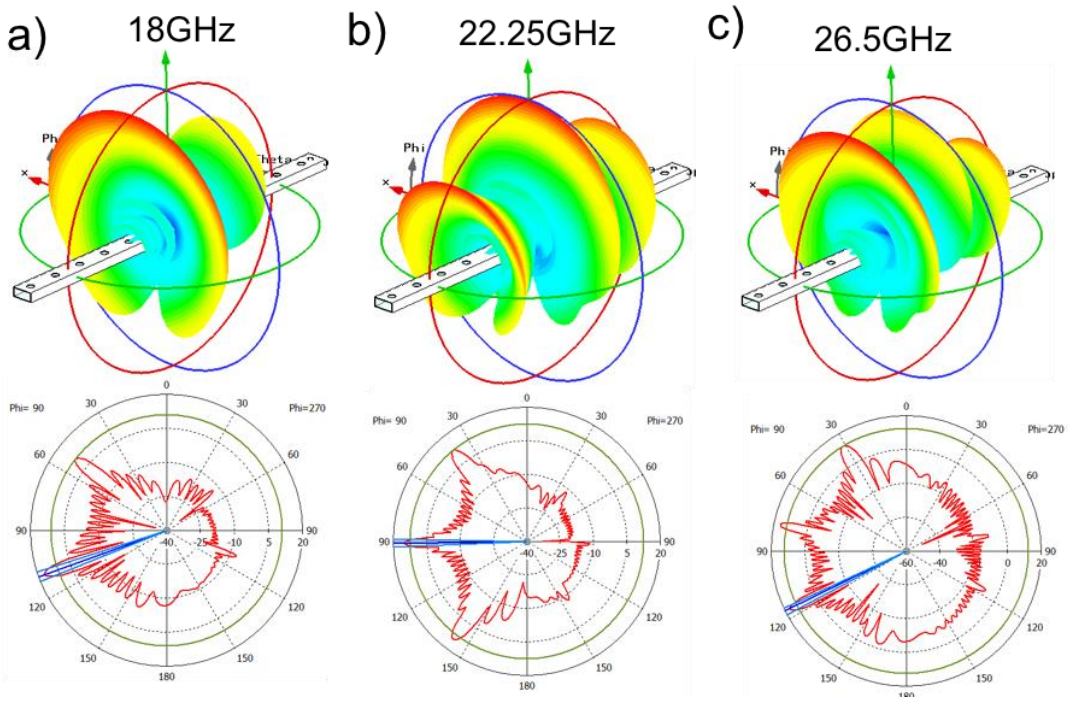

Figure 5.4 Periodicity of leaky holes on an air-filled K-band waveguide optimized for centering the main beam at center frequency.

The split-block fashion is widely used in radio frequency components when the inside of a waveguide filter contains complicated features such as corrugated waveguides, filters, couplers, etc. [79]. However, the split-block construction unavoidably introduces losses from discontinuity at the joining interface. It is thus difficult for split-block components to have perfect sealing and alignment. One of the most used methods for good alignment is to use alignment pins [102] or to have alignment features integrated into the components. Figure 5.1a-b) shows the alignment pins and holes integrated into

the half blocks of the antenna panel. As discussed in Chapter 4, the best way to mitigate energy leaking out of the split-block is to split from the center of the E-plane for an air-filled rectangular waveguide. However, in the design presented here, the only possible location for splitting the spiral waveguide is through the center of the H-plane. This is because the radiating holes are placed on the broad wall and have to face towards the object. Alternatively, these holes can be placed on the short walls, which enables cutting through the center E-plane, but limits the amount of radiation energy. In addition, the equivalent dipoles of such holes are also smaller, if they are on the short wall [85]. Thus, sealing the split-blocks in this design becomes a major contribution to energy loss, which eventually derogates the Q-factor. Plastic tends to warp, due to external pressure, causing gaps to form between the screws that are used for tightening. However, if designed correctly, the deformability can actually help to seal the gap, thereby decreasing the loss of energy. Figure 5.5 shows the design of a sealing feature that was used in this design. A curved recess is featured at the place where the screws align, and this tightens the two split-blocks together. When the screws are fastened, the two halves of the curved recess, together, act as a spring that directs the pressure to the edge of the split, as shown in Figure

5.5 (b). With the design shown in Figure 5.5 (b), energy lost due to leakage can be further reduced and, as a result, prevent the Q-factor from decreasing.

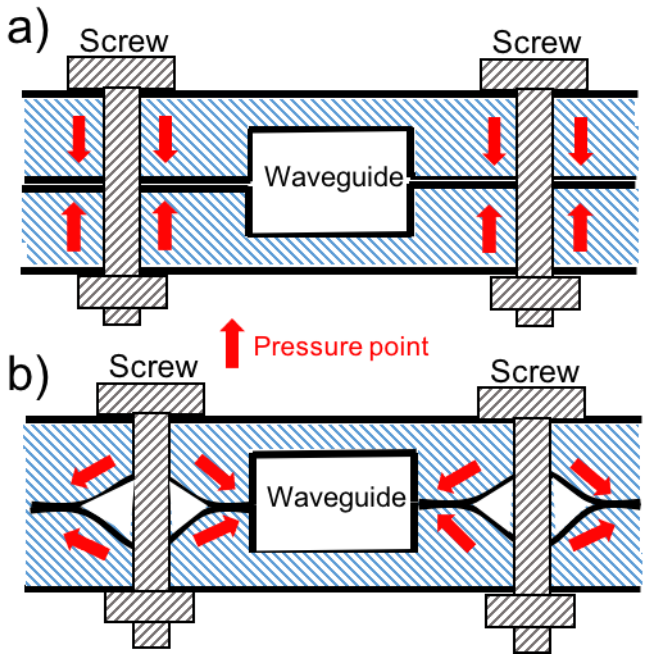

Figure 5.5 Diagram of the split-block design with curved recess

(a) Schematic drawing of split-block waveguide sections without curved recess feature. (b) Curved recess features are applied to the split-blocks preventing energy from leaking through the gap between blocks.

5.3 Frequency diverse antenna measurement

To evaluate the design of this frequency diverse antenna based on a spiral leaky waveguide, the Q-factor and the radiation efficiency are estimated to assess its ability to conduct computational imaging experiments. The Q-factor can be estimated by measuring the |S11| parameter in the time domain [103], i.e., the voltage impulse response, with a

vector network analyzer (VNA), as shown in Figure 5.7. Note that the decay of the impulse response in the time domain is an exponential decay due to power loss in the antenna, with the relationship described as

$$Q = 2\pi f_0 \frac{1}{2\alpha} \tag{5.6}$$

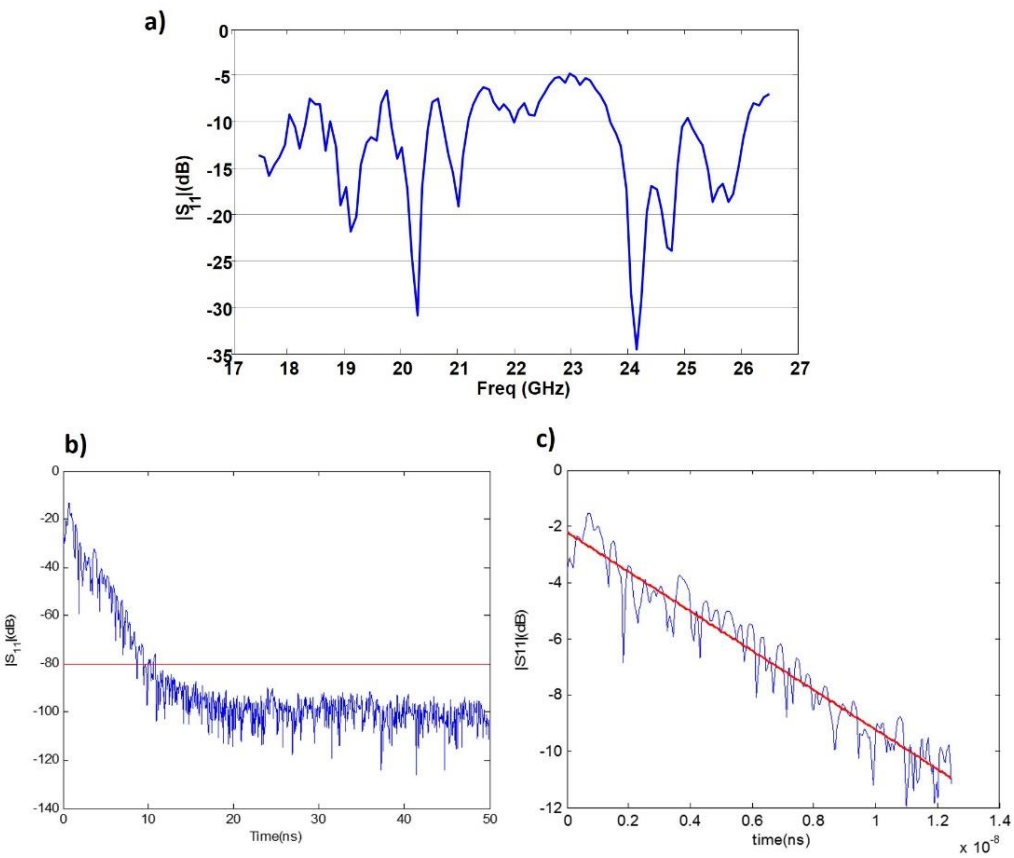

Figure 5.6 |S11| measurement of the antenna and the Q-factor estimation

(a) frequency domain measurement for coupling loss analysis, (b) time domain measurement (c) Q-factor estimation by measuring the time domain voltage impulse response.

The measured impulse response is displayed in a log-linear plot in order to estimate the decay factor in the form of e^{α}. The red line indicates the -80dB noise level, 20dB above the -100dB floor of the VNA used; using only the data above the noise floor results in a more accurate estimation. The value of α is estimated by linear fitting on the log-linear plot, as shown in figure 5.6 (b). As a result of Eq. 5.6, the estimated Q-factor is Q≈110. The number of distinct measurement modes is thus $\frac{QB}{f_0}$ ~ 45.

The |S11| parameter in the frequency domain as shown in figure 5.5 (a) is measured to assess the reflected energy due to imperfect coupling. The signal is coupled with the waveguide by an SMA-WR42 adapter, which is flushed against the waveguide opening on the panel. The reflection is, on average, below -5dB and is a possible result of discontinuity at the joint of two blocks that are close to the input port.

The radiation efficiency is measured by using an NSI near-field scanner [104] to measure the E-field, i.e. the |S21| parameter, in the x-y plane in both horizontal and vertical polarization. The scan covers a 60° field of view from the antenna, which is sampled at the Nyquist rate for the center frequency of the K-band [13]. The radiation efficiency is estimated to be the summation of power received at each sampling point across the frequency bandwidth i.e.

$$h(f) = \sum_{x}^{M} \sum_{y}^{N} |S_{21}(x,y,f)|^2 \tag{5.7}$$

The estimated radiation efficiency for both polarizations is shown in Figure 5.7. The average efficiency over the K-band frequencies is around 40%.

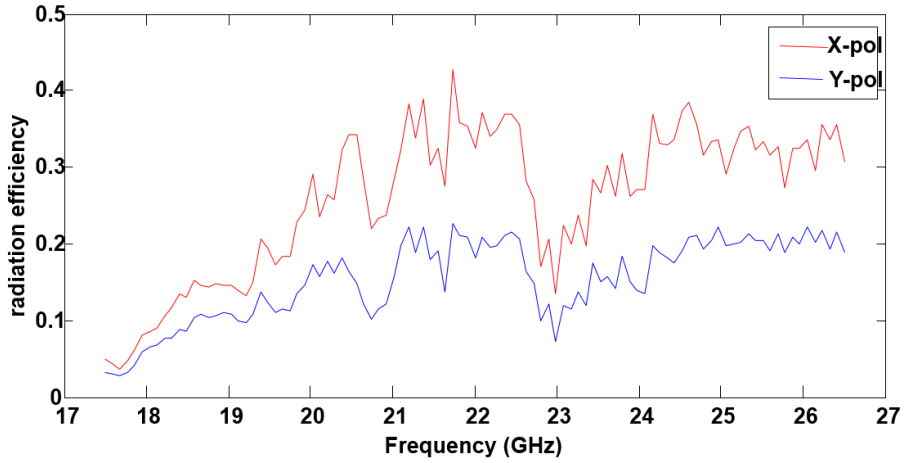

Figure 5.7 Radiation efficiency estimation of the frequency diverse antenna, at both x- and y- polarization

To demonstrate the frequency diversity, the radiation pattern in the near-field, at different frequencies across the K-band, are shown in Figures 5.9 (a-c). It was assumed up to this point that every hole along the spiral waveguide is excited with the same level of power. However, as the waveguide feed resides in the center of the spiral, it can be seen that the power decreases as the guided wave encounters more radiating holes along the waveguide. Thus, the holes nearest the center are excited with higher power than the ones near the edges. The design of the leaky spiral waveguide thus include holes that increase in size, from the center to the edges. Figure 5.9 (d) shows the superimposed back propagated radiation pattern, measured at 101 frequencies across the K-band.

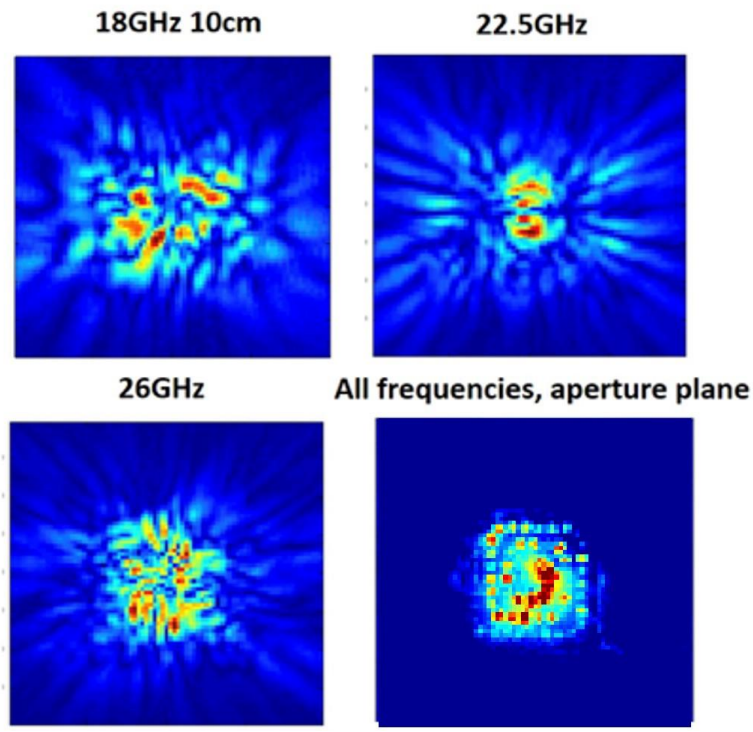

Figure 5.8 Radiation pattern of the leaky wave frequency diverse antenna

a) 18GHz, b)22.5 GHz, and c) 26 GHz, and d) back-propagated pattern at the aperture plane over all 101 frequency points.

5.4 Imaging experiment

The imaging system consists of a transmitting antenna (Tx) and four receiving probe antennas (Rx). The configuration is shown in Figure 5.9. The frequency diverse antenna described above is used as the transmitting antenna, whereas the receiving antennas are simple traditional open-ended waveguide probes for the K-band. Although using a frequency diverse antenna as both transmitting and receiving antenna, i.e. a panel-to-panel configuration [105], results in a much high mode diversity, the radiation efficiency of a single frequency diverse antenna presented here is limited to 40% on

average across the K-band. Unfortunately, the limited radiation efficiency is squared when multiplying the efficiency of the transmitting antenna and receiving antenna, thus resulting in as low as 16% on average across the K-band. Low radiation efficiency results in low signal to noise (SNR) ratio and thus subject to noise that shows up as artifacts in the reconstructed image. The open-ended probes, although they do not contribute the mode diversity, have a gain of +6 dB and thus can effectively improve the SNR. The frequency diverse antenna performs imaging by measuring the S21 parameter between the antenna and the probes, i.e. the signal radiated from the antenna, reflected off the target, and received by the probes. The complex signals received by the probes are recorded by a VNA over 101 points across the K-band.

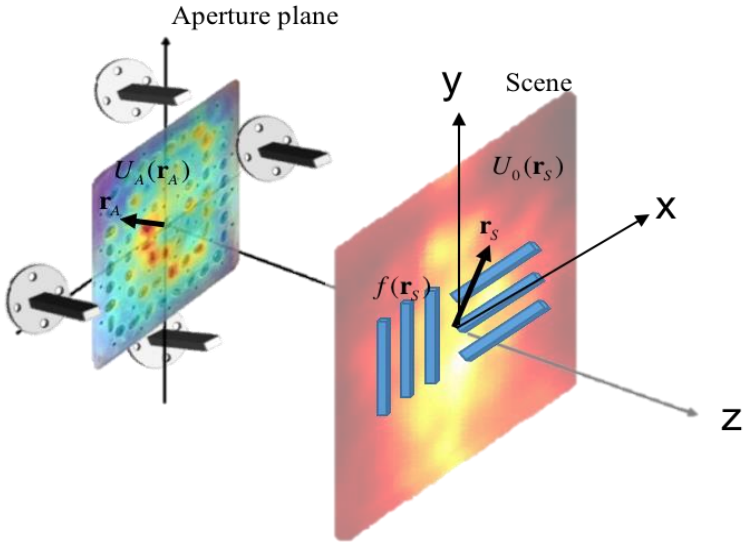

Figure 5.9 Configuration for the panel-to-probe imaging system using the frequency diverse antenna based on a spiral leaky waveguide.

The back propagated field pattern indicating radiation strength at the aperture plane is shown as an overlay over the panel

To apply the computational imaging method, the forward model of the image acquisition process has to be modelled. The detail of the modeling method can be found in [7] and a brief review is included, to introduce the necessary knowledge. Consider the imaging configuration shown in Figure 5.9, where the field at the aperture plane is denoted as $U_A(\boldsymbol{r_A})$. The field propagated to the imaging scene at z0 can be described as:

$$U_0(\mathbf{r}_S) = \iint_S U_A(\mathbf{r}_A)\frac{\partial}{\partial z}G(\mathbf{r}_S,\mathbf{r}_A)d^2\mathbf{r}_A$$

$$G(\mathbf{r}_S,\mathbf{r}_A) = \frac{e^{-jb_0|\mathbf{r}_S-\mathbf{r}_A|}}{|\mathbf{r}_S-\mathbf{r}_A|}$$

$$\frac{\partial}{\partial z}G(\mathbf{r}_S,\mathbf{r}_A) = z\left(\frac{jb_0}{|\mathbf{r}_S-\mathbf{r}_A|} - \frac{1}{|\mathbf{r}_S-\mathbf{r}_A|^2}\right)G(\mathbf{r}_S,\mathbf{r}_A) \tag{5.8}$$

where $G(\mathbf{r_S},\mathbf{r_A})$ is the scalar propagator for the field from the aperture plane to the scene. In the case when the field $U_0(\boldsymbol{r_A})$. is in a free-space region, $U_0(\boldsymbol{r_A})$ becomes a solution to the source-free Helmholtz equation, i.e.,

$$\nabla^2 U_0 + b_0^2 U_0 = 0 \tag{5.9}$$

However, when an object with a different refractive index is present, the incident and the scattered waves must be solutions of

$$\nabla^2 U_T + (b_0^2 + \Delta b(\mathbf{r}_S))^2 U_T = 0. \tag{5.10}$$

Under the first Born approximation, the second order term involving $\Delta\beta(r)^2$ in the above equation can be neglected, thus resulting in

$$\nabla^2 U_T + \beta_0^2 U_T = -2\beta_0 \Delta\beta(\mathbf{r}_S) U_T$$
$$= -f(\mathbf{r}_S) U_0(\mathbf{r}_S) \tag{5.11}$$

where the right-hand-side of the equation becomes the source of the total field, assuming the incident field $U_0(\boldsymbol{r_S})$ is not strongly perturbed by the object and $f(\boldsymbol{r_S})$ denotes the refractive index variation, i.e., the object.

The next step is to find the field backscattered from the object to the aperture plane where the receivers reside. The backscattered field can be calculated in a similar way to Eq (5.8) except treating the field at the scene as the source for propagation, i.e.,

$$U_S(\mathbf{r}_A) = -\int_V G(\mathbf{r}_A, \mathbf{r}_S) f(\mathbf{r}_S) U_0(\mathbf{r}_S) d^3\mathbf{r}_S \tag{5.12}$$

Let $T_{Rx}(\boldsymbol{r_A})$ denote the spatial distribution of receiver probes, which is a sum of delta functions in 2D space on the aperture plane. Knowing the backscattered field distribution at the aperture plane and where the probes are, the measurement can be described as

$$g = \int_S U_S(\mathbf{r}_A) T_{Rx}(\mathbf{r}_A) d^2\mathbf{r}_A \quad . \tag{5.13}$$

Substituting Eq (5.12) and Eq (5.8),

$$g = -T_{RX}(\mathbf{r}_A) \int_V f(\mathbf{r}_S) U_0(\mathbf{r}_S) \int_z U_0(\mathbf{r}_S) D^{-1}(\mathbf{r}_A, \mathbf{r}_S) dz\, d^3\mathbf{r}_S \tag{5.14}$$

where

$$D(\mathbf{r}_S, \mathbf{r}_A) = z\left(\frac{j\beta_0}{|\mathbf{r}_S - \mathbf{r}_A|} - \frac{1}{|\mathbf{r}_S - \mathbf{r}_A|^2}\right)$$
$$\frac{\partial}{\partial z} G(\mathbf{r}_S, \mathbf{r}_A) = D(\mathbf{r}_S, \mathbf{r}_A) G(\mathbf{r}_S, \mathbf{r}_A) \tag{5.15}$$

Eq(5.13) further simplifies by applying paraxial approximation at far-field, i.e. $z \cong |\mathbf{r}_A - \mathbf{r}_S|$ and ignoring the $\frac{1}{R^2}$ term in D (r_A, r_S), yielding

$$g = \frac{j}{b_0} T_{RX}(\mathbf{r}_A) \int_V f(\mathbf{r}_S) U_0^{\,2}(\mathbf{r}_S)\, d^3\mathbf{r}_S \tag{5.16}$$

To construct the forward model, the imaging space containing the target is discretized into three-dimensional voxels and is represented by vector f with dimension M×1. The discretization is done by sampling the spatial domain using voxel size equaling to half of the shortest wavelength in the K-band. The measurement vector is denoted by g, with dimension N×1. In this experiment N=440 because the measurements are sampled using 101 frequency points with a total of 4 probes. For a single probe, the measurement at one frequency is

$$g_n = \frac{j}{b_0} \sum_M U_0^{\,2}(\mathbf{r}_S)\, f(\mathbf{r}_S) \qquad \text{Eq(5.17)}$$

which can be modeled as a linear equation $g = Hf$, similar to the method described in Chapter 3, such that

$$\begin{bmatrix} g_1 \\ g_2 \\ \vdots \\ g_N \end{bmatrix} = \begin{bmatrix} h_{11} & h_{12} & \dots & h_{1M} \\ h_{21} & h_{22} & & \\ \vdots & & \ddots & \\ h_{N1} & & & h_{NM} \end{bmatrix} \begin{bmatrix} f_1 \\ f_2 \\ \vdots \\ f_M \end{bmatrix} \qquad \text{Eq (5.18)}$$

Note that the number of measurement N has to be treated differently than the number of distinct measurement modes. It is possible to acquire enough samples by using

a large amount of receiver so that N=M. However, g can still be under-sampled in such a case because of the orthogonality of the measurements; i.e., all N measurements may not be independent. Thus, the problem becomes a traditional compressive sensing problem and can be solved by various techniques such as L-1 minimization [64], matched filtering [104], or an iterative method such as general minimal residual (GMRes) [106].

The range resolution and diffraction limit cross-range resolution can be derived using standard SAR equations, i.e.

$$d_r = \frac{c}{2B}$$
$$d_{cr} = \frac{l_0 Z}{D} \qquad \text{Eq (5.19)}$$

where B is the frequency bandwidth, c is the speed of light, Z is the distance between the aperture and the scene in the axial direction, and D is the effective aperture size for the frequency diverse antenna, including the receiver probes. In this experiment, the K-band bandwidth is 9GHz, yielding a range resolution of 1.67 cm. The effective aperture size is 38 cm, thus at Z = 60cm and the center wavelength of 1.3 cm, the cross range resolution is about 2.05 cm.

To test imaging with this frequency diverse antenna, based on a spiral leaky waveguide, a target T-shaped target is shown, that has been placed 60 cm away from the antenna. The T-shape target is made of two 2 cm x 10 cm copper tape patches. A simulation is done by a virtualizer program [104] to test the capability of the imaging system and to use it as the benchmark for the actual experimental result. The transmitting

antenna in the simulation is characterized by the electric field that is superimposed over all frequency points at the aperture plane. The simulated target, as shown in Figure 5.11a, is placed 60 cm away from the aperture plane. The virtualizer simulates the radiated field and backscattered field, treating the target as a perfect reflector, and simulated measurements with 20dB SNR are collected at the receiver locations. The reconstruction is done, using different methods, for example, TwIST to enforce L-1 minimization, a matched filter, and GMRes. The respective results are shown in Figure 5.10 (c). The dashed outline in the results indicates the actual dimension and location of the simulated targets. Figure 5.10 (b) shows the actual target made of copper tape. The result of reconstructing the measurements are shown in Figure 5.10(d) with different methods. As shown in Figure 5.10 (c-d), the reconstructions from the measurement show agreement to the simulated reconstructions and are able to localize the T-shape in the scene. The artifacts and differences between actual reconstruction and the simulated reconstructions resulted from noise and an imperfect surface of the copper tape.

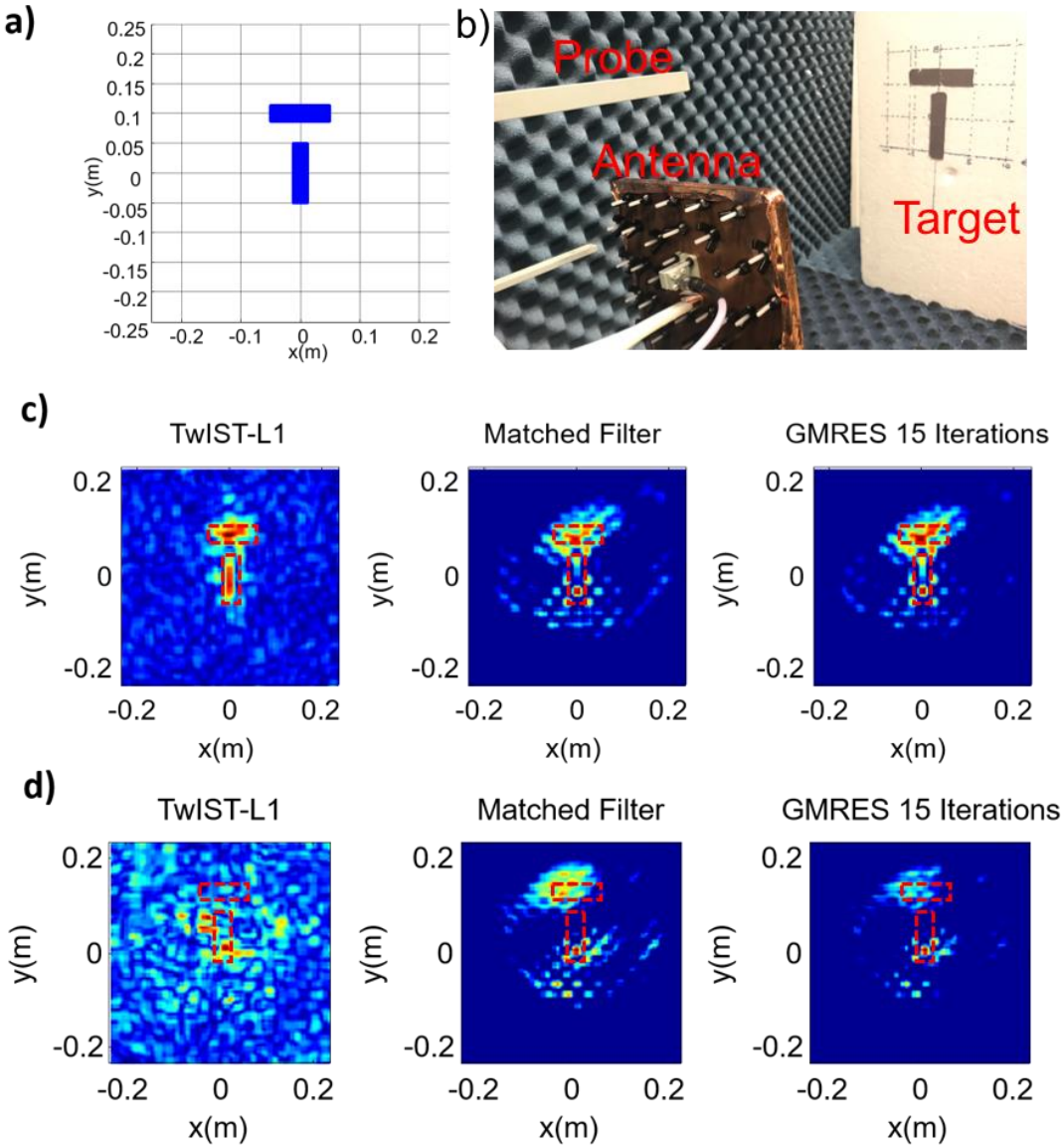

Figure 5.10 Simulation and experimental results of the computational imaging system based on a leaky spiral waveguide

(a) The simulated T-shaped target in the virtualizer program (b) the actual T-shaped target made of copper tape (c) reconstruction of simulation measurements using TwIST-L1, matched filter and GMRes with 15 iterations, respectively (d) reconstruc

5.5 Discussion

In this chapter, a novel frequency-diverse antenna is proposed as a solution to improve radar imaging by combining computational imaging methods and novel antenna design. The proposed antenna design based on a spiral leaky waveguide shows high Q-factor and good mode diversity across the K-band frequencies and has achieved diffraction-limit imaging with probes as receivers. The proposed system has been able to eliminate the need for synthesizing a large aperture with antenna array or the need for scanning a probe across the imaging scene while imaging a 2D scene.

Computational imaging method introduces a trade-off between computational complexity and the physical process. While the reduction of mechanical scanning puts a heavy requirement on computational power, the accuracy of modeling the forward model becomes sensitive to the accuracy of the reconstruction. While using the first Born approximation makes the modeling easy, in fact, the targets are highly scattering and sometimes specular [6].

Another factor that needs optimizing is SNR of the imaging system, which requires a higher radiation efficiency for frequency diverse antenna. The trade-off introduced when deciding the number of radiating holes in the leaky waveguide is between a high Q-factor and a high SNR. Future work can be done to optimize the number of leaky hole element while maximizing the achievable Q-factor and maintaining a high radiation efficiency.

6. Conclusion

We have explored the different ways to improve the efficiency for radar imaging using computational imaging methods and combining computational imaging with novel antenna design. Traditional high frequency radar imaging has been implemented using either focal plane array or synthetic aperture technologies. The former method is a straightforward imitation to optical cameras yet expensive to implement in high frequency as the cost for its intricate circuitry increases as the frequency and bandwidth increase. The latter method mechanically scans a transceiver to form a large effective aperture, thus increasing the diffraction limited resolution of the imaging system. The tradeoff has been between the acquisition time and the system cost. Computational imaging methods are capable of acquiring information beyond the recorded pixels, thus is an intuitive approach to incorporate into radar imaging to reduce the amount of sensors needed and reduce the system cost effectively. For computational imaging to be effectively reducing the amount of data needed, the data acquisition process has to be multiplexed, which inspired the research on designing frequency diverse antenna design. Frequency diversity antennas make it possible to encode a 3D scene using radiation pattern with spatial variation at different frequencies. With the help of frequency diverse antenna, high-resolution radar imaging with a single antenna using a fast frequency sweep can be eventually achieved, which is a significant improvement over traditional focal plane imaging or the SAR imaging.

To reduce the number of sensors in radar imaging systems, a time-of-flight (ToF) imaging algorithm for millimeter wave frequencies is proposed in chapter 2. The system utilizes a sparse array of horn antennas in a multi-static setup to collectively reconstruct the surface profile and reflectivity. The demonstration in this thesis is done in 2D by reconstructing a slice of the 3D target. However, with more powerful computers in the future, 3D reconstruction can be done using the same algorithm. Unlike SAR imaging which treats the target as diffusive objects, this algorithm works under the assumption that the target being a specular reflecting object that bounces millimeter waves off the surface. Although this assumption enables modeling the time-of-flight information as a single peak, it is hard to reconstruct diffusive targets and targets with more complicated structures that cause multiple reflections.

A similar method [123] in the optical frequencies implemented using an array of streak camera was proposed to image around a corner. The significance of this proposed algorithm is the ability to image occluded targets, either the target is concealed or is not in the line of sight. It is not only a method for reducing the number of sensors for radar imaging systems but also can be used for localizing occluded or buried reflective targets. An example application is for ballistic studies for army and military research.

For single transceiver imaging system relying on mechanical scanning such as SAR and ISAR imaging, an adaptive sampling method based on Bayesian compressive sensing framework has been proposed in chapter 3. For the ISAR experiment discussed in Chapter

3, a single transceiver revolves around the scene and collect range data at different angles. The adaptive algorithm provides a posterior estimation based on all previous measurements. The method proposed here significantly reduces the need for mechanical scanning for ISAR imaging systems operating in the millimeter wave frequencies. Also, it is a reliable method that does not need prior information of the complexity of the scene and can stop after the reconstruction converges. The simulated experiments are reconstructed in 2D for simplicity. Future effort can be made towards implementing this algorithm for the 3D experiments, thus enabling real-world applications. The challenge for extending this algorithm to 3D applications remains in size of the model, and the calculation needed for choosing the next optimum measurement location. Although the proposed method is developed in the context of millimeter wave imaging and is designed for a specific ISAR system, the method can be well applied to any other single aperture imaging modalities in any frequency range that rely on mechanical scanning.

The ultimate goal for applying computational methods to improve radar imaging is to break the tradeoff between physical sensors and mechanical scanning. This goal can be achieved with an antenna design that can perform multiplexed measurement. Thus a 3D scene can be reconstructed with a single antenna using measurements at different frequencies. A frequency scan is rather fast compared to mechanical scan. Thus it can be treated as a “snapshot” solution.

To facilitate the antenna design and prototyping process in a laboratory environment, we have presented in chapter 4 a method for rapid prototyping antennas and other components using a high-resolution 3D printer. The printed antenna is then metallized with pure copper on the surface to guide electromagnetic waves. Although antennas and RF circuits can be made using low-cost methods on dielectric substrates, for high-frequency applications that require low loss transmission, air-filled waveguides are considered as the main option. Also, as pointed out in chapter 5, air-filled antennas has much higher Q-factors over dielectric based antennas which translate to better imaging ability. These considerations have motivated the low-cost, rapid prototyping method presented here. The prototyping time for a customized design antenna drops from 1-2 months with a conventional machine shop to 2-3 days with a 3D printer. To demonstrate the feasibility of replacing traditionally manufactured passive components with 3D printed ones, we have tested the performance of the 3D printed waveguides and antennas and compared to identical parts from vendors. The almost identical performance in a laboratory environment shows promising future for 3D printed passive components. Future work should be directed towards manufacturing integrated passive circuits and improving the efficiency of the electroless copper plating process. For example, the current technique relies on the waveguides to be designed in split-block fashion, which introduces discontinuity at the walls and thus energy loss. A method to effectively stream chemicals inside the waveguide could be a potential solution.

With the ability to rapid prototype custom designed antenna, a novel air-filled frequency diverse antenna based on a leaky waveguide. The goal is to let the antenna generate distinct radiation patterns at different frequencies thus to multiplex the 3D scene. The key to the antenna design is to achieve a high Q-factor that results in larger number of distinct measurement modes. With frequency diverse antennas and computational imaging method, radar imaging can eventually be done using a single antenna with a fast frequency sweep. Frequency diverse antennas can be seen as an ensemble of radiating dipoles regardless of whether the design is based on metamaterials, resonant cavities, or leaky waveguides, yet these radiating elements do not need to be excited individually like phased array antennas. The challenge this method faces is the design tradeoff between radiation efficiency and the Q-factor, and also the processing speed. With ongoing efforts to build a real-time high-resolution millimeter wave imager using a large array of cavity based frequency diverse antennas, it is foreseeable in the near future that frequency diverse antennas will be widely used in high-frequency radar imaging.

7. Bibliography

[1] M. I. Skolnik, *Radar Handbook*. 2008.

[2] K. Mori, T. Takahashi, I. Ide, H. Murase, T. Miyahara, and Y. Tamatsu, "Recognition of foggy conditions by in-vehicle camera and millimeter wave radar," *2007 IEEE Intell. Veh. Symp.*, pp. 87–92, 2007.

[3] L. P. Song, C. Yu, and Q. H. Liu, "Through-wall imaging (TWI) by radar: 2-D tomographic results and analyses," *IEEE Trans. Geosci. Remote Sens.*, vol. 43, no. 12, pp. 2793–2798, 2005.

[4] D. M. Sheen, D. L. McMakin, and T. E. Hall, "Three-dimensional millimeter-wave imaging for concealed weapon detection," *IEEE Trans. Microw. Theory Tech.*, vol. 49, no. 9, pp. 1581–1592, 2001.

[5] D. L. Marks, O. Furxhi, and D. J. Brady, "W-band imager without mechanical scanning based on an echelle spectrometer," in *International Conference on Infrared, Millimeter, and Terahertz Waves, IRMMW-THz*, 2014.

[6] J. Hunt, J. Gollub, T. Driscoll, G. Lipworth, A. Mrozack, M. S. Reynolds, D. J. Brady, and D. R. Smith, "Metamaterial microwave holographic imaging system.," *J. Opt. Soc. Am. A. Opt. Image Sci. Vis.*, vol. 31, no. 10, pp. 2109–19, 2014.

[7] G. Lipworth, A. Mrozack, J. Hunt, D. L. Marks, T. Driscoll, D. Brady, and D. R. Smith, "Metamaterial apertures for coherent computational imaging on the physical layer," *J. Opt. Soc. Am. A*, vol. 30, no. 8, pp. 1603–1612, 2013.

[8] L. J. Cutrona, W. E. Vivian, E. N. Leith, G. O. Hall, L. J. Cutronat, S. Member, W. E. Viviant, E. N. Leitht, and G. Hallt, "A High-Resolution Radar Combat-Surveillance System," *IRE Trans. Mil. Electron.*, vol. MIL–5, pp. 127–131, 1961.

[9] L. Yujiri, M. Shoucri, and P. Moffa, "Passive millimeter wave imaging," *Microw. Mag. IEEE*, vol. 4, no. 3, pp. 39–50, 2003.

[10] D. R. Wehner, *High-resolution radar*, 2nd ed. Artech House Publishers, 1931.

[11] D. L. Marks, "Theory of Spatially Resolving Antenna Arrays using Frequency Diversity," pp. 1–21, 2015.

[12] R. Zhu, T. Zvolensky, and D. Marks, "Millimeter wave computational imaging with 3D printed leaky wave frequency diverse antenna," in *2016 41st International Conference on Infrared, Millimeter, and Terahertz waves (IRMMW-THz)*, 2016, p. 1.

[13] O. Yurduseven, J. N. Gollub, D. L. Marks, and D. R. Smith, “Frequency-diverse microwave imaging using planar Mills-Cross cavity apertures,” *Opt. Express*, vol. 24, no. 8, p. 8907, 2016.

[14] E. J. Candes and M. B. Wakin, “An Introduction To Compressive Sampling,” *IEEE Signal Process. Mag.*, vol. 25, no. 2, pp. 21–30, 2008.

[15] D. L. Donoho, “Compressed sensing,” *IEEE Trans. Inf. Theory*, vol. 52, no. 4, pp. 1289–1306, 2006.

[16] C. Shannon, “A mathematical theory of communication,” *ACM SIGMOBILE Mob. ComThe Bell Syst. Tech. Journalputing …*, vol. 27, no. July 1948, pp. 379–423, 1948.

[17] A. Mrozack, M. Heimbeck, D. L. Marks, J. Richard, H. O. Everitt, and D. J. Brady, “Compressive and Adaptive Millimeter-wave SAR,” *arXiv Prepr. arXiv1402.1466*, pp. 1–14, 2014.

[18] J. Hunt, T. Driscoll, A. Mrozack, G. Lipworth, M. Reynolds, D. Brady, and D. R. Smith, “Metamaterial Apertures for Computational Imaging,” *Science (80)*., vol. 339, no. 6117, pp. 310–313, 2013.

[19] D. J. Brady, A. Dogariu, M. a Fiddy, and A. Mahalanobis, “Computational optical sensing and imaging: introduction to the feature issue.,” *Appl. Opt.*, vol. 47, no. 10, pp. COSI1–I2, 2008.

[20] G. R. Arce, D. J. Brady, L. Carin, H. Arguello, and D. S. Kittle, “Compressive coded aperture spectral imaging: An introduction,” *IEEE Signal Processing Magazine*, vol. 31, no. 1. pp. 105–115, 2014.

[21] D. J. Brady, *Optical imaging and spectroscopy*. 2009.

[22] M. Liang, Y. Li, H. Meng, M. Neifeld, and H. Xin, “Reconfigurable Array Design to Realize Principal Component Analysis (PCA) Based Microwave Compressive Sensing Imaging System,” *IEEE Antennas Wirel. Propag. Lett.*, vol. PP, no. 99, pp. 1–1, 2015.

[23] G. H. Huff and J. T. Bernhard, “Reconfigurable Antennas,” in *Modern Antenna Handbook*, 2007, pp. 369–398.

[24] P. Antonik, M. C. Wicks, H. D. Griffiths, and C. J. Baker, “Frequency diverse array radars,” in *IEEE National Radar Conference - Proceedings*, 2006, pp. 215–217.

[25] J. J. Adams, E. B. Duoss, T. F. Malkowski, M. J. Motala, B. Y. Ahn, R. G. Nuzzo, J. T. Bernhard, and J. A. Lewis, “Conformal printing of electrically small antennas on three-dimensional surfaces,” *Adv. Mater.*, vol. 23, no. 11, pp. 1335–1340, 2011.

[26] E. G. Geterud, P. Bergmark, and J. Yang, “Lightweight Waveguide and Antenna Components Using Plating on Plastics,” in *7th European Conference on Antennas and Propogation (EuCAP)*, 2013, pp. 1812–1815.

[27] G. Du, M. Liang, R. A. Sabory-Garcia, C. Liu, and H. Xin, “3-D Printing Implementation of an X-band Eaton Lens for Beam Deflection,” *IEEE Antennas Wirel. Propag. Lett.*, vol. 15, pp. 1487–1490, 2016.

[28] W. J. Otter and S. Lucyszyn, “3-D printing of microwave components for 21st century applications,” *2016 IEEE MTT-S Int. Microw. Work. Ser. Adv. Mater. Process. RF THz Appl.*, no. October, pp. 1–3, 2016.

[29] S.-Y. Wu, C. Yang, W. Hsu, and L. Lin, “3D-printed microelectronics for integrated circuitry and passive wireless sensors,” *Microsystems Nanoeng.*, vol. 1, no. April, p. 15013, 2015.

[30] Z. Wu, W.-R. Ng, M. E. Gehm, and H. Xin, “Terahertz electromagnetic crystal waveguide fabricated by polymer jetting rapid prototyping.,” *Opt. Express*, vol. 19, no. 5, pp. 3962–3972, 2011.

[31] P. Goldsmith, C. Hsieh, and G. Huguenin, “Focal Plane Imaging Systems for Millimeter Wavelengths,” *Microw. Theory …*, vol. 41, no. 10, 1993.

[32] H. J. Visser, *Array and Phased Array Antenna Basics*. 2006.

[33] A. J. Fenn, D. H. Temme, W. P. Delaney, and W. E. Courtney, “The Development of Phased-Array Radar Technology,” *Lincoln Lab. J.*, vol. 12, no. 2, pp. 321–340, 2000.

[34] D. Pozar, *Microwave Engineering Fourth Edition*. 2005.

[35] Naval air systems command, and Naval air warfare center. Electronic warfare and radar systems engineering handbook. Naval air warfare center, 1997.

[36] C. Wolff, Radar Tutorial, http://www.radartutorial.eu/

[39] E. Hecht, “Optics 4th edition,” *Optics 4th edition by Eugene Hecht Reading MA AddisonWesley Publishing Company 2001*, vol. 1. p. 122, 2001.

[38] W. M. Brown, “Synthetic Aperture Radar,” *Aerosp. Electron. Syst. IEEE Trans.*, vol. AES-3, no. 2, pp. 217–229, 1967.

[39] M. E. Gehm, R. John, D. J. Brady, R. M. Willett, and T. J. Schulz, “Single-shot compressive spectral imaging with a dual-disperser architecture,” *Opt. Express*, vol. 15, no. 21, pp. 14013–14027, 2007.

[40] P. Llull, X. Liao, X. Yuan, J. Yang, D. Kittle, L. Carin, G. Sapiro, and D. J. Brady, "Coded aperture compressive temporal imaging," *Opt. Express*, vol. 21, no. 9, p. 10526, 2013.

[41] T.-H. Tsai, X. Yuan, and D. J. Brady, "Spatial light modulator based color polarization imaging," *Opt. Express*, vol. 23, no. 9, pp. 11912–11926, 2015.

[42] E. Yigit, "Compressed sensing for millimeter-wave ground based SAR/ISAR imaging," *J. Infrared, Millimeter, Terahertz Waves*, vol. 35, no. 11, pp. 932–948, 2014.

[43] T. M. Cover and J. a. Thomas, *Elements of Information Theory*. 2005.

[44] D. R. Jackson, C. Caloz, and T. Itoh, "Leaky-wave antennas," *Proc. IEEE*, vol. 100, no. 7, pp. 2194–2206, 2012.

[45] J. Bewersdorf, A. Egner, and S. W. Hell, "4Pi Microscopy," in *Handbook of Biological Confocal Microscopy*, 2006, pp. 561–570.

[46] H. Asao, K. Henmi, M. Mukuda, and N. Yoneda, "Ku-band power combiner composed of metal-plated plastic waveguide hybrid," in *2004 IEEE MTT-S International Microwave Symposium Digest (IEEE Cat. No.04CH37535)*, 2004, vol. 2, pp. 8–11.

[47] H. Asao, N. Yoneda, M. Mukuda, K. Yamasaki, O. Kamohara, Y. Yoshino, and K. Henmi, "Metal-plated plastic waveguide filter using injection molding process," in *IEEE MTT-S International Microwave Symposium Digest*, 2003, vol. 2.

[48] J. S. Chieh, B. Dick, S. Loui, and J. D. Rockway, "Development of a Ku -Band Corrugated Conical Horn Using 3-D Print Technology," *IEEE Antennas Wirel. Propag. Lett.*, vol. 13, pp. 201–204, 2014.

[49] H. H. Tsang, J. H. Barton, R. C. Rumpf, and C. R. Garcia, "Effects of extreme surface roughness on 3D printed horn antenna," *Electron. Lett.*, vol. 49, no. 12, pp. 734–736, 2013.

[50] P. Isaac, "3D Printed Electromagnetic Transmission and Electronic Structures Fabricated on a Single Platform Using Advanced Process Integration Techniques," *Proc. Natl. Acad. Sci. U. S. A.*, vol. 104, no. 25, pp. 10335–9, 2014.

[51] M. Ahmadloo and P. Mousavi, "Application of novel integrated dielectric and conductive ink 3D printing technique for fabrication of conical spiral antennas," *IEEE Antennas Propag. Soc. AP-S Int. Symp.*, pp. 780–781, 2013.

[52] P. Nayeri, M. Liang, S. Member, R. A. Sabory-garc, M. Tuo, F. Yang, S. Member, M. Gehm, H. Xin, and A. Z. Elsherbeni, "3D Printed Dielectric Re fl ectarrays : Low-Cost High-Gain Antennas at Sub-Millimeter Waves," *IEEE Trans. Antennas Propag.*, vol. 62, no. 4, pp. 2000–2008, 2014.

[53] M. D. Auria, S. Member, W. J. Otter, J. Hazell, B. T. W. Gillatt, C. Long-collins, and N. M. Ridler, “3-D Printed Metal-Pipe Rectangular Waveguides,” *IEEE Trans. Components, Packag. Manuf. Technol.*, vol. 5, no. 9, pp. 1339–1349, 2015.

[54] N.H. Farhat and W. R. Guard, "Millimeter wave holographic imaging of concealed weapons," Proc. IEEE, vol. 59, pp. 1383-1384, Sept 1971.

[55] H.D. Collins, D. L. McMakin, and T. E. Hall, et. al., "Real-time holographic surveillance system," U.S. Patent Patent 5455590, 1995.

[56] A. L. Boyer, "Reconstruction of ultrasonic images by backward propagation," in Acoustic Holography, New York :Plenum, 1970, pp. 333-384.

[58] D. M. Sheen, D.L. McMakin, and T. E. Hall, "Near Field Imaging at Microwave and Millimeter Wave Frequencies," IEEE, 2007.

[59] M. Soumekh, "Bistatic synthetic aperture radar inversion with application in dynamic object imaging," IEEE Trans. Signal Processing, vol. 39, pp. 2044-2055, 1991.

[60] M. Soumekh, "A system model and inversion for synthetic aperture radar imaging," IEEE Trans. Signal Processing, vol. 1, pp. 64-76, A1992.

[61] M. A. Lefsky, W. B. Cohen, G. G. Parker, and D. J. Harding, “Lidar remote sensing for ecosystem studies,” *Bioscience*, vol. 52, no. 1, pp. 19–30, 2002.

[62] J. Means and S. Acker, “Predicting forest stand characteristics with airborne scanning lidar,” *Photogramm. Eng. Remote Sens.*, vol. 66, no. 11, pp. 1367–1371, 2000.

[63] P. R. Gill, A. Wang, and A. Molnar, "The In-Crowd Algorithm for Fast Basis Pursuit Denois- inig," IEEE Trans. Signal Processing, vol. 59, pp. 4595-4605, July 2011 2011.

[64] E. J. Candès, M. B. Wakin, and S. P. Boyd, “Enhancing sparsity by reweighted L1 minimization,” *J. Fourier Anal. Appl.*, vol. 14, no. 5–6, pp. 877–905, 2008.

[65] S. Vitebskiy and L. Carin, "Moment-method modeling of short-pulse scattering from and the resonances of a wire buried insed a lossy, dispersive half-space," IEEE Trans. Antennas and Propagation, vol. 43, pp. 1303-1312, 1995.

[66] E. L. Jacobs, "Scattering from a rough resistive sheet E Polarization " PhD thesis, The George Washington University, 2001.

[67] T. D. DeRose and B. a. Barsky, “Geometric continuity, shape parameters, and geometric constructions for Catmull-Rom splines,” *ACM Trans. Graph.*, vol. 7, no. 1, pp. 1–41, 1988.

[68] S. Boyd and L. Vandenberghe, *Convex Optimization*, vol. 25, no. 3. 2004.

[69] M. Costa, A. P. Braga, and B. R. De Menezes, “Improved generalization learning with sliding mode control and the Levenberg-Marquadt algorithm,” in *Proceedings - Brazilian Symposium on Neural Networks, SBRN*, 2002, vol. 2002-January, pp. 44–48.

[70] O. Oshiga, S. Severi, and G. T. F. De Abreu, “Superresolution Multipoint Ranging with Optimized Sampling via Orthogonally Designed Golomb Rulers,” in *IEEE Transactions on Wireless Communications*, 2016, vol. 15, no. 1, pp. 267–282.

[71] A. Bisognin, D. Titz, and F. Ferrero, “3D printed plastic 60 GHz lens: Enabling innovative millimeter wave antenna solution and system,” in 2014 IEEE MTT-S International Microwave Symposium (IMS), 2014, pp. 1–4.

[72] R. Zhu, G. Lipworth, T. Zvolensky, D. Marks, and D. Smith, “Versatile manufacturing of split block microwave devices using rapid prototyping and electroplating,” IEEE Antennas Wirel. Propag. Lett., vol. 1225, no. c, pp. 1–1, 2016.

[73] E. Macdonald, R. Salas, D. Espalin, M. Perez, E. Aguilera, D. Muse, and R. B. Wicker, “3D Printing for the Rapid Prototyping of Structural Electronics,” IEEE Access, vol. 2, pp. 234–242, 2014.

[74] Y. Bai and C. B. Williams, “An Exploration of Binder Jetting of Copper,” *Rapid Prototyp. J.*, vol. 21, no. 2, pp. 177–185, 2015.

[75] X. Gong, T. Anderson, and K. Chou, “Review on Powder-Based Electron Beam Additive Manufacturing Technology,” in *ASME/ISCIE 2012 International Symposium on Flexible Automation*, 2012, pp. 507–515.

[76] P. Yen, “Improved ABS plastic activating treatment for electroless copper plating,” *Polymer*, vol. 36, no. 17. pp. 3399–3400, 1995.

[77] W. Gui-xiang, L. Ning, H. Hui-li, and Y. Yuan-chun, “Process of direct copper plating on ABS plastics,” *Appl. Surf. Sci.*, vol. 253, no. 2, pp. 480–484, 2006.

[78] N. V Mandich, “EMI shielding by electroless plating of ABS plastics.,” *Plat. Surf. Finish.*, vol. 81, no. 10, pp. 60–63, 1994.

[79] C. H. Smith, A. Sklavonuos, and N. Scott Barker, “SU-8 micromachin- ing of millimeter and submillimeter waveguide circuits,” in IEEE MTT-S International Microwave Symposium Digest, 2009, pp. 961–964.

[80] M. Liang, X. Yu, C. Shemelya, E. Macdonald, H. Xin, and E. Paso, “3D Printed Multilayer Microstrip Line Structure with Vertical Transition toward Integrated Systems,” no. 1, pp. 5–8, 2015

[81] O. S. Carneiro, A. F. Silva, and R. Gomes, “Fused deposition modeling with polypropylene,” *Mater. Des.*, vol. 83, pp. 768–776, 2015.

[82] J. J. Kuzmik, “Chapter 14 Plating on Plastics,” in Electroless Plating - Fundmentals and Applications, 1990, pp. 377–399.

[83] J. S. Kim, D. S. Kim, and M. C. Lee, “3D printing method of multi piezo head using a photopolymer resin,” in *ICCAS 2007 - International Conference on Control, Automation and Systems*, 2007, pp. 2587–2590.

[84] R. Bogue, “3D printing: the dawn of a new era in manufacturing?,” *Assem. Autom.*, vol. 33, no. 4, pp. 307–311, 2013.

[85] C. E. Balanis, “Antenna Theory: Analysis and Design, 3rd Edition - Constantine A. Balanis,” *Book*. p. 1136, 2005.

[86] N. V Mandich, “EMI shielding by electroless plating of ABS plastics.,” *Plat. Surf. Finish.*, vol. 81, no. 10, pp. 60–63, 1994.

[87] M. Paunovic, “Electroless deposition of copper,” in *Modern Electroplating*, vol. 1, 2010, pp. 433–446.

[88] E. Uzunlar, Z. Wilson, and P. a. Kohl, “Electroless Copper Deposition Using Sn/Ag Catalyst on Epoxy Laminates,” *J. Electrochem. Soc.*, vol. 160, no. 12, pp. D3237–D3246, 2013.

[89] J. W. Dini and D. D. Snyder, “Electrodeposition of Copper,” in *Modern Electroplating: Fifth Edition*, 2011, pp. 33–78.

[90] P. C. Andricacos, C. Uzoh, J. O. Dukovic, J. Horkans, and H. Deligianni, “Damascene copper electroplating for chip interconnections,” *IBM J. Res. Dev.*, vol. 42, no. 5, pp. 567–574, 1998.

[91] P. C. Andricacos, C. Uzoh, J. O. Dukovic, J. Horkans, and H. Deligianni, “Damascene copper electroplating for chip interconnections,” pp. 567– 574, 1998.

[92] P. M. Vereecken, R. a. Binstead, H. Deligianni, and P. C. Andricacos, “The chemistry of additives in damascene copper plating,” *IBM J. Res. Dev.*, vol. 49, no. 1, pp. 3–18, 2005.

[93] F. L. Warner, A. E. Bailey, "Attenuation measurement" in Microwave Measurements, London, U.K.:IET Press, pp. 132-134, 1989.

[94] M. Liang, X. Yu, C. Shemelya, E. Macdonald, H. Xin, and E. Paso, “3D Printed Multilayer Microstrip Line Structure with Vertical Transition toward Integrated Systems,” in *2015 IEEE MTT-S International Microwave Symposium, IMS 2015 (2015)*, 2015, no. 1, pp. 5–8.

[95] R. Baraniuk and P. Steeghs, “Compressive radar imaging,” in *IEEE National Radar Conference - Proceedings*, 2007, pp. 128–133.

[96] J. H. G. Ender, “On compressive sensing applied to radar,” *Signal Processing*, vol. 90, no. 5, pp. 1402–1414, 2010.

[97] M. Rossi, A. M. Haimovich, and Y. C. Eldar, “Spatial compressive sensing for MIMO radar,” *IEEE Trans. Signal Process.*, vol. 62, no. 2, pp. 419–430, 2014.

[98] J. Ender, “A Brief Review of Compressive Sensing Applied to Radar,” in *14th International Radar Symposium (IRS)*, 2013, pp. 3–16.

[99] D. Marks, O. Yurduseven, and D. Smith, "Cavity-backed metasurface antennas and their application to frequency diversity imaging," J. Opt. Soc. Am. A 34, 472-480 (2017).

[100] T. Fromenteze, O. Yurduseven, M. F. Imani, J. Gollub, C. Decroze, D. Carsenat, and D. R. Smith, “Computational imaging using a mode-mixing cavity at microwave frequencies,” *Appl. Phys. Lett.*, vol. 106, no. 19, pp. 15–20, 2015.

[101] L. Goldstone and a. Oliner, “Leaky-wave antennas I: Rectangular waveguides,” *IRE Trans. Antennas Propag.*, vol. 7, no. 4, pp. 307–319, 1959.

[102] R. Safavieh, M. Pla Roca, M. A. Qasaimeh, M. Mirzaei, and D. Juncker, “Straight SU-8 pins,” *J. Micromechanics Microengineering*, vol. 20, no. 5, p. 055001, 2010.

[103] W. M. Siebert, Circuits, Signals, and Systems (Massachusetts Institute of Technology, 1985)

[104] G. Lipworth, A. Rose, O. Yurduseven, V. R. Gowda, M. F. Imani, H. Odabasi, P. Trofatter, J. Gollub, and D. R. Smith, “Comprehensive simulation platform for a metamaterial imaging system,” *Appl. Opt.*, vol. 54, no. 31, p. 9343, 2015.

[105] V. R. Gowda, J. N. Gollub, O. Yurduseven, and D. R. Smith, “Multistatic microwave imaging with arrays of planar cavities,” *IET Microwaves, Antennas Propag.*, vol. 10, no. 11, pp. 1174–1181, 2016.

[106] H. F. Walker, “Implementations of the GMRES method,” *Comput. Phys. Commun.*, vol. 53, no. 1–3, pp. 311–320, 1989.

[107] X. Yuan, T. Tsai, R. Zhu, P. Llull, D. Brady, and L. Carin, “Compressive Hyperspectral Imaging with Side Information,” *IEEE J. Sel. Top. Signal Process.*, vol. 9, no. 6, pp. 964–976, 2015.

[108] T. S. Ralston, D. L. Marks, P. Scott Carney, and S. a. Boppart, “Interferometric synthetic aperture microscopy,” Nat. Phys., vol. 3, no. 2, pp. 129–134, 2007.

[109] D. Takhar, J. N. Laska, M. B. Wakin, M. F. Duarte, D. Baron, S. Sarvotham, K. F. Kelly, and R. G. Baraniuk, “A new compressive imaging camera architecture using optical-

domain compression," Proced. Comput. Imaging, vol. 6065, pp. 606509–606509–10, 2006.

[110] W. L. Chan, K. Charan, D. Takhar, K. F. Kelly, R. G. Baraniuk, and D. M. Mittleman, "A single-pixel terahertz imaging system based on compressed sensing," Appl. Phys. Lett., vol. 93, no. 12, 2008.

[111] L. Xiao, K. Liu, D. Han, and J. Liu, "A compressed sensing approach for enhancing infrared imaging resolution," Opt. Laser Technol., vol. 44, no. 8, pp. 2354–2360, 2012.

[112] J. Greenberg, K. Krishnamurthy, and D. Brady, "Compressive single-pixel snapshot x-ray diffraction imaging.," Opt. Lett., vol. 39, no. 1, pp. 111–4, 2014.

[113] D. J. Brady, D. L. Marks, K. P. MacCabe, and J. A. O'Sullivan, "Coded apertures for x-ray scatter imaging.," Appl. Opt., vol. 52, no. 32, pp. 7745–54, 2013.

[114] O. Furxhi, D. L. Marks, and D. J. Brady, "Echelle crossed grating millimeter wave beam scanner," Opt. Express, vol. 22, no. 13, pp. 16393–16407, 2014.

[115] I. Daubechies, "The wavelet transform, time-frequency localization and signal analysis," Inf. Theory, IEEE Trans., vol. 36, no. 5, pp. 961–1005, 1990.

[116] L. Yu and Y. Zhang, "Random step frequency CSAR imaging based on compressive sensing," Prog. Electromagn. Res. C, vol. 32, no. June, pp. 81–94, 2012.

[117] J. H. G. Ender, "On compressive sensing applied to radar," Signal Processing, vol. 90, no. 5, pp. 1402–1414, 2010.

[118] K. B. Cooper, R. J. Dengler, N. Llombart, T. Bryllert, G. Chattopadhyay, E. Schlecht, J. Gill, C. Lee, A. Skalare, I. Mehdi, and P. H. Siegel, "Penetrating 3-D imaging at 4- and 25-m range using a submillimeter-wave radar," IEEE Trans. Microw. Theory Tech., vol. 56, no. 12, pp. 2771–2778, 2008

[119] S. Ji, Y. Xue, and L. Carin, "Bayesian Compressive Sensing," IEEE Trans. Signal Process., vol. 56, no. 6, pp. 2346–2356, Jun. 2008.

[120] M. Tipping, "Sparse Bayesian Learning and the Relevance Vector Machine," J. Mach. Learn. Res., 2001.

[121] G. Lauritsch and W. H. Haerer, "Theoretical framework for filtered back projection in tomosynthesis," Proc. SPIE 3338, 1127–1137 (1998).

[122] Z. Wang, A. C. Bovik, H. R. Sheikh, and E. P. Simoncelli, "Image quality assessment: From error visibility to structural similarity," IEEE Trans. Image Process., vol. 13, no. 4, pp. 600–612, 2004.

[123] A. Velten, T. Willwacher, O. Gupta, A. Veeraraghavan, M. G. Bawendi, and R. Raskar, "Recovering three-dimensional shape around a corner using ultrafast time-of-flight imaging," *Nat. Commun.*, vol. 3, p. 745, 2012.

8. Biography

Ruoyu Zhu was born on March 30, 1990, in Daqing, Heilongjiang, China. His family moved to Beijing in 2005. Ruoyu attended high school at the Beijing Concord College of Sino-Canada in 2005. He was the president of the student union and ranked top 1% at his high school. In 2008, Ruoyu started his undergraduate studies in Electrical Engineering at the University of Illinois at Urbana-Champaign where he was actively involved in imaging related research. In 2011 he was awarded the Frank D. and Irene M. Low Scholarship, and in 2012 the E. C. Jordan Award for excellence in academics and his efforts in research. In 2012, Ruoyu received the B.S. degree in Electrical Engineering with honors. In the same year, he attended Duke University for his Ph.D. degree in Electrical Engineering. Ruoyu joined the Duke Imaging and Spectroscopy Group and focused on researching in computational imaging. Hi will receive the Ph. D. degree in Electrical Engineering in 2017.